Applications of plasmonics in silicon based photonic devices

Roney Thomas

Submitted in accordance with the requirements for the degree of Doctor of Philosophy

The University of Leeds
School of Electronic and Electrical Engineering

November 2012

The candidate confirms that the work submitted is his own and that appropriate credit has been given where reference has been made to the work of others.

This copy has been supplied on the understanding that it is copyright material and that no quotation from the thesis may be published without proper acknowledgement

© *2012 The University of Leeds and Roney Thomas*

Acknowledgements

I acknowledge the help and guidance to the staff, students, and fellow researchers for smoothly carrying out my PhD studies at the University of Leeds. In particular, I would like to convey my special thanks to the supervisors Prof. Robert W. Kelsall, and Dr. Zoran Ikonic for guiding me to become an effective researcher in this new field of physics.

I would like to give special thanks to my co-workers, in particular to Leon Lever for introducing me to the Comsol simulation programming software, Neil Pilgrim for guiding me in carrying charge transport simulations, and Alex Valavanis in helping me to carry out programming relevant to my research.

Finally, I want to deeply acknowledge my family and friends for their kind support through out the period of my research, and special thanks to my wife Tina Thomas for helping me for proofreading of my thesis.

Roney Thomas

Abstract

Surface plasmon polaritons are highly confined electromagnetic waves which can be employed in developing miniaturised optical devices for bridging the size-mismatch between the nanoscale electronics and large diffraction-limited photonic devices. For this purpose, it is desired to develop silicon compatible plasmonic devices in order to achieve seamless integration with electronics on the silicon-on-insulator platform. Plasmonic devices such as modulators, detectors, couplers, (de)multiplexers, etc, would possess the advantages of having a small device footprint, low cost, low power consumption and faster response time.

In this thesis, different silicon-based plasmonic devices were investigated using finite element simulations, including optical modulators, couplers and splitters. A metallised stub filled with SiGe/Ge multiple quantum wells or quantum dots in a silicon matrix, coupled to a dielectric waveguide was investigated. The modulation principles include 'spoiling' of the Q factor and conversion of the electromagnetic mode parity, due to variation of the absorption coefficient of the stub filling.

A CMOS compatible interference-based Mach-Zehnder modulator with each arm comprising a metal-insulator-semiconductor-insulator-metal structure, and a simpler single arm variant, were considered for electro-optic and electroabsorption modulation respectively. The electron density profiles in bias-induced accumulation layers were calculated with the inclusion of size-quantisation effects at the oxide-silicon interfaces. These were then used to find the complex refractive index profiles across the structure, in its biased and unbiased states, and eventually the modulator insertion loss and extinction

ratio, and their dependence on various structural parameters.

Finally, a silicon-based plasmonic nanofocusing coupler was investigated, which comprised symmetric rectangular grooves converging towards a central metal-silicon-metal nano-slit at the apex of the structure. The structure was optimised to achieve maximum coupling of light incident from a wide input opening, and coherent excitation and focusing of surface plasmons as they propagate towards the nano-slit waveguide. Application of the nanofocusing structure to achieve simultaneous coupling and splitting was also investigated, whereby incident light was focused into two nano-slits separated by a metal gap region at the apex. Such a plasmonic coupler or splitter can be used for coupling light directly from a wide fibre grating opening into nanoplasmonic waveguides in future on-chip plasmonic-electronic integrated circuits, or into the two arms of a plasmonic Mach-Zehnder modulator.

List of publications

The following journal papers were published by the author during the course of the present work.

Journal papers

- R. Thomas, Z. Ikonic, and R.W. Kelsall, "Plasmonic enhanced electro-optic stub modulator", Photo. and Nanostr.– Fund. and Appl., 9 (2011), 101–107.
- R. Thomas, Z. Ikonic, and R.W. Kelsall, "Electro-optic metal–insulator–semiconductor–insulator–metal Mach-Zehnder plasmonic modulator", Photo. and Nanostruc.– Fund. and Appl., 10 (2012), 183–189.
- R. Thomas, Z. Ikonic, and R.W. Kelsall, "SiGe metallized stub and plasmonic gap mode electro-absorption modulators", Proc. of SPIE, 7943 (2011), 79431A.
- R. Thomas, Z. Ikonic, and R.W. Kelsall, "Silicon based plasmonic coupler", Opt. Exp., Vol 20 (19), 21520–21531 (2012).
  - Photon 12 Durham (IOP)- Best runner up poster prize for the paper (3-6 Sept. 2012).

Submitted paper

- R. Thomas, Z. Ikonic, and R.W. Kelsall, "Plasmonic modulators for near-infrared photonics on a silicon-on-insulator platform", IEEE J. of Sel. Top. in Quant. Elec.

on Nanoplas., Submitted (2012).

Conference presentations

- R. Thomas, Z. Ikonic, and R.W. Kelsall, "Silicon-based plasmonic coupler", Photon12: Inst. of Phys., Durham, 3-6 Sept. 2012.
- R. Thomas, Z. Ikonic, and R.W. Kelsall, "A CMOS compatible metallised nanofocusing coupler", 9th International Conf. on Group IV Phot., San Diego, California (USA), 29-31 Aug 2012.
- R. Thomas, Z. Ikonic, and R.W. Kelsall, "Silicon-on-insulator plasmonic waveguide coupler", EMRS, Strasbourg (France), 27-31 May 2012.
- R. Thomas, Z. Ikonic, and R.W. Kelsall, "Three dimensional finite element modelling of a plasmonic electro-absorption modulator, TMCS III, University of Leeds, Jan 2012.
- R. Thomas, Z. Ikonic, and R.W. Kelsall, "Electro-optic Mach-Zehnder plasmonic modulator", EMRS, Nice (France), 9-13 May 2011.
- R. Thomas, Z. Ikonic, and R.W. Kelsall, "Plasmonic enhanced SiGe stub modulator on a SOI platform in communication wavelength range", Photon10, Southampton, 23-26 Aug, 2010.
- R. Thomas, Z. Ikonic, and R.W. Kelsall, "Metallised SiGe stubs on planar Si waveguides for electro-absorption plasmonic modulators in communication wavelength range", UK Semiconductors, Sheffield, 7-8 Jul, 2010.
- R. Thomas, Z. Ikonic, and R.W. Kelsall, "Applications of plasmonics in SiGe stub modulators using electro-absorption effect in the communications wavelength range", Plasmonics meeting (UK), 10 May 2010.

List of abbreviations

SPPs	Surface plasmon polaritons
FEEM	Finite element electromagnetic model
QM	Quantum mechanical
CMOS	Complementary-metal–oxide–semiconductor
SOI	Silicon-on-insulator
IMI	Insulator-metal-insulator
MIM	Metal-insulator-metal
EO	Electro-optic
EA	Electroabsorption
CGD	Conductor–gap–dielectric
TMM	Transfer matrix model
TE/TM	Transverse electric/ Transverse magnetic
MQW	Multiple quantum wells
QD	Quantum dots
MISIM	Metal-insulator-semiconductor-insulator-metal
MOS	Metal-oxide-semiconductor

List of symbols

Fundamental constants

$c = 3.00\times10^{8}\,\mathrm{m/s}$	Speed of light in vacuum
$e = 1.60\times10^{-19}\,\mathrm{C}$	Elementary charge
$\varepsilon_0 = 8.85\times10^{-12}\,\mathrm{F/m}$	Vacuum permittivity
$m_e = 9.11\times10^{-31}\,\mathrm{kg}$	Rest mass of free electron

Symbols

ω_p	Bulk plasma frequency
ω_{sp}	Surface plasmon frequency
k	Wavevector
k_{SPP}	SPPs wavevector
ϵ	Dielectric constant
$\epsilon(\omega)$	Complex dielectric function
κ	Imaginary part of the complex refractive index
n	Real part of the refractive index
α	Absorption coefficient
λ_0	Free space wavelength
λ_{SPP}	SPP wavelength
γ	Collision frequency
τ	Relaxation time
v_g	Group velocity
γ	Complex propagation constant
γ_{SPP}	SPP propagation constant
g	Reciprocal vector
Γ	Complex reflection coefficient amplitude of the SPPs
Q_S	Quality factor of the stub
$\triangle n_{Si}$	Change in Si refractive index
$\triangle n_{eff}$	Change in effective mode index
ϕ	Phase shift

Electronic properties

D	Electric displacement field
P	Polarisation
μ_0	Magnetic permeability in free space
σ	Conductivity
I	Electric field intensity
E_f	Quasi-Fermi energy
E_C	Conduction band energy level
E_V	Valence band energy level
N_e	Electron concentration
N_h	Hole concentration
n	Total electron density
Q	Total charge density

Contents

Acknowledgements **i**

List of publications **v**

List of abbreviations **vii**

List of symbols **ix**

Contents **xii**

1 Introduction **1**

1.1 Brief history of plasmonics 1

1.2 Applications 3

1.3 Structure of the thesis 11

2 Theory of surface plasmon polaritons **13**

2.1 The optical properties of metals 13

2.2 Surface plasmon polaritons at metal-dielectric interfaces 17

2.3 Dispersion relation of SPPs at a metal-dielectric interface 22

2.4 Multilayer plasmonic systems 24

2.4.1 EM field confinement and slow light effects in a periodic metal grating system 29

2.5 Choice of metals 40

3 A silicon based plasmonic enhanced stub modulator 41

3.1 Introduction 41

3.2 The finite element and transmission line models of the metallised stub structure 43

3.3 Two dimensional finite element modelling of the metallised stub structure 46

3.4 Comparison of the finite element and transmission line results 48

3.5 Lateral stub resonance modes 50

3.5.1 Optimisation 53

3.6 Biasing schemes for the electrical control of the plasmonic stub modulator 54

4 Three dimensional modelling of a plasmonic-enhanced stub modulator 61

4.1 Introduction 61

4.2 Three dimensional modelling of the original metallised stub structure . . . 65

4.3 Optimisation 69

4.4 Discussion 73

5 Conductor-gap-dielectric systems and MOS-type optical modulators 75

5.1 Introduction 75

5.2 Conductor-gap-dielectric systems 76

5.3 Electro-optic MOS plasmonic modulators 85

5.3.1 Inversion and accumulation mode devices including quantum mechanical effects 87

5.3.2 2D optimisation and electro-optic modulation 90

5.3.3 Asymmetric biasing scheme 97

5.4 MISIM electroabsorption device 98

6 Silicon-based plasmonic coupling to nano-slot and SOI waveguides 107

6.1 Introduction: optical transmission in different plasmonic structures 107

6.2 Silicon-based metallised grooved plasmonic nano-focusing coupler 110

6.3 Two dimensional finite element and transfer matrix models 112

6.4 Optimisation of the coupling efficiency for varying physical parameters . . 122

6.5 Applications to SOI waveguide coupling and plasmon mode splitting . . . 127

7 Conclusion and future outlook **133**

7.1 Summary 133

7.2 Future of silicon-based plasmonic integrated circuits 138

Chapter 1

Introduction

1.1 Brief history of plasmonics

Even before researchers began their investigation on the optical properties of metals, they were used by artists to generate different colours in glass artifacts and artwork where gold and silver nanoparticles of different sizes and shapes were painted onto glass to create beautiful colours, such as the famous Lycurgus cup of 4th century AD (Figure 1.1). The cup appears green when exposed to light from outside (Figure 1.1a) and shines in red when illuminated from inside the cup (Figure 1.1b). The oscillating electromagnetic (EM) field of the incident light causes free electrons of the metal to oscillate, which prohibits or screens light from penetrating more than only a fraction of its wavelength into the metal. The frequency at which these electrons oscillate on the surface of metal nanoparticles causes light to be mostly scattered. Therefore, a significantly reduced transmission and enhanced reflection occurs, which results in the unusual optical properties exhibited by the Lycurgus cup.

Surface plasmon polaritons (SPPs) were first described by Ritchie in 1957 who theoretically investigated the loss spectra of a low energy plasma of electrons moving through thin metal foil in an externally applied field [1]. SPPs are electromagnetic waves that are confined to the interface of two media with opposite signs of permittivity. They can occur due to a resonant interaction of an incident EM field with collective electron

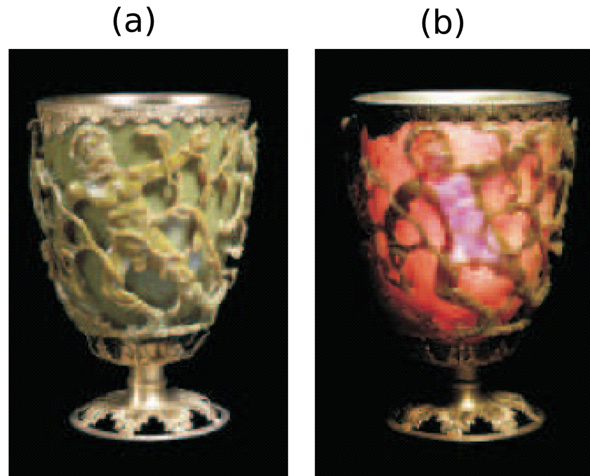

Figure 1.1: Lycurgus cup showing the enhanced scattering of light by embedded metal nanoparticles when (a) shined under ambient light from outside and (b) when illuminated from inside the cup.

density wave oscillations on the surface of metal nanoparticles. The word polariton in the term SPP indicates a coupled oscillation of bound electrons and light on the metallic surface, and was first described by Cunnigham et.al in 1974 [2].

Earlier studies carried out by Pines and Bohm showed that, due to the long range nature of the Coulomb force, an electron gas of high density produces organised oscillations, also called *plasma* oscillations [3–6]. A range of electron energy loss experiments on magnesium and aluminium were carried out by Powell and Swan, that demonstrated the existence of electromagnetic excitation of SPPs at the metal-air interface [7]. These excitations occurred at lower energies ($\omega_p/\sqrt{2}$ where ω_p is the bulk plasma frequency), which was previously predicted by Ritchie [8]. Subsequently, the influence of dielectric coatings over the metal on the resonance frequency and angular dependence of the intensity in the context of energy loss experiments was also investigated [9]. In the late 1960's, excitation of propagating SPPs along a thin metal-air interface via attenuated total reflection (ATR) was demonstrated using Kretschmann and Otto prism configurations as shown in Figure 1.2.

Light (with wavevector k) incident at an angle θ to the surface normal of a planar

metal-dielectric interface has a momentum $k_x = k \sin\theta$ along the interface (i.e the propagation direction). The wavevector k_x is smaller than that of the SPPs, which means that a phase matching condition between the incident light and SPPs must be satisfied that provides extra momentum in order to excite SPPs. This can be achieved using Kretschmann and Otto prism configurations (using the three layer system shown in Figure 1.2), in which light is incident from the glass side at an angle greater than the critical angle, such that a total internal reflection occurs within the glass. In such a situation, the wavevector of the beam reflected at the interface between the glass prism (with dielectric constant ϵ) and metal will have an in-plane momentum of $k_x = k\sqrt{\epsilon} sin\theta$, which is sufficient to excite SPPs at the metal-air interface. It should be noted that SPPs at the metal-prism interface cannot be excited because the dispersion curve lies outside the light line of the prism cone as indicated in Figure 1.3 [10, 11]. The mismatch of the momentum between the incident light and that of the SPPs can also be compensated via ATR through diffraction at the surface of a diffraction grating[12].

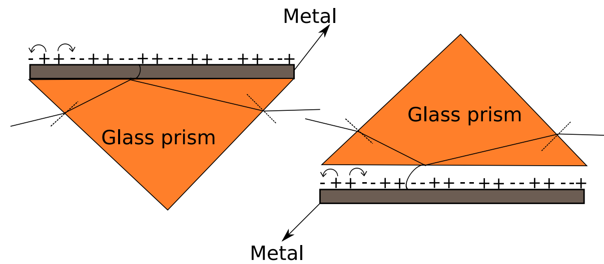

Figure 1.2: Schematic diagram of prism coupling to SPPs using attenuated total internal reflection with Kretschemann (left) and Otto (right) configurations [10, 11].

1.2 Applications

Since the discovery of SPPs and advances in nanoscale fabrication techniques, there have been significant developments in both theoretical and experimental research, which have lead to the use of SPPs in various applications ranging from electrochemistry [13] and biosensing [14–16] to scanning tunnelling microscopy, surface plasmon microscopy [17, 18],

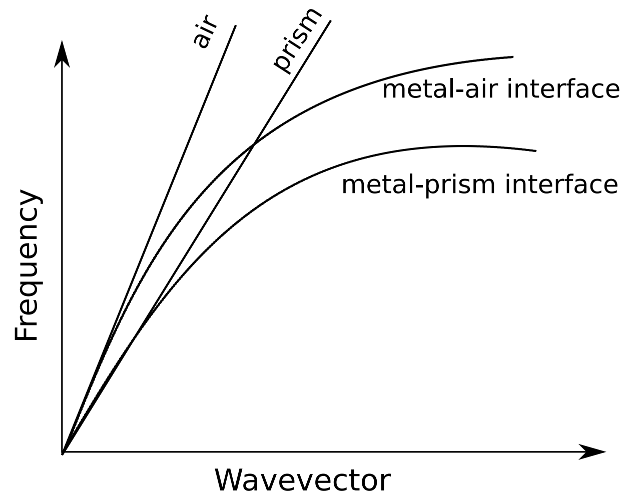

Figure 1.3: Shows the light lines (dispersion) in air and prism, and SPP light lines at the metal-air and metal-prism interface. The excitation of SPPs at the metal-air interface is possible since its dispersion lies within the prism light cone.

and surface plasmon resonance technology for biological interactions and gas detection [19–24]. Using the Kretschmann technique (Figure 1.4), excitation of SPPs at a metal-dielectric interface can be achieved, and subsequently surface plasmon resonance (SPR) can be obtained when the momentum of the excited SPPs is matched to those of the incident photons. SPR is very sensitive to even a slight change in the conditions of the media near the interface. Thus, if the exciting light is kept at a fixed wavelength then SPR provides precise measurement of changes in the refractive index or thickness of the medium placed in close proximity to the interface, and also changes in its absorption characteristics [15, 25]. Figure 1.4 shows the conventional approach for detecting the induced change in refractive index or thickness of a biomolecular layer due to some molecular interactions, which influence the SPR characteristics.

In recent years, there has been growing research interest in the use of SPPs for tuning the electromagnetic properties of metallic nanostructures, which in turn can be achieved by tailoring their geometrical features [26, 27]. SPPs can also serve as a basis for the design, fabrication and characterisation of subwavelength waveguide components [28–38]. They can be made to focus and concentrate light in subwavelength structures,

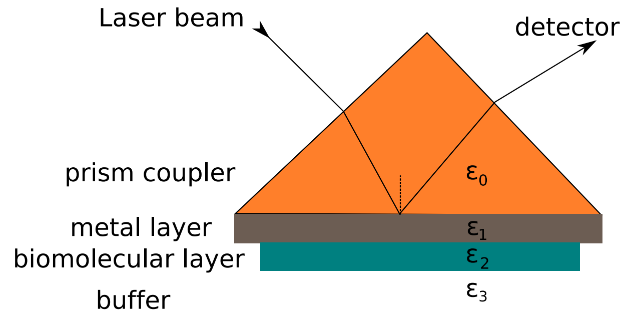

Figure 1.4: Schematic diagram of a conventional SPR biosensor used to detect the variation in the biomolecular interaction, which in turn induces changes in the refractive index and thickness of the biomolecular layer adjacent to the metal-dielectric prism structure.

or to achieve enhanced optical transmission through periodic arrays of subwavelength holes deposited on optically thick metallic films [39, 40]. Furthermore, there has been a tremendous development in SPP based circuits, in order to integrate photonics and electronics [41]. This new technology would possess the advantages of both photonics and electronics, which include faster response time, smaller device footprint and therefore lower costs and amount of materials used, and possible complementary-metal-oxide-semiconductor processing feasibility.

Control over the propagation of SPPs at a metal-dielectric interface can be achieved by introducing surface modulation, for example by creating local defects in the form of nanoscale particle-like structures or milling holes into the film. These defects aid scattering of the SPPs, and thereby modify their dispersion in the dielectric medium. Periodic height-modulated silica nanostructures, such as particles and wires of 70nm height deposited on top of a silica substrate, for control over SPP propagation via scattering from height modulation, were demonstrated by Ditlbacher et. al. [42] (Figure 1.5). Silica nanostructures were subsequently coated with a thick metal film. By focusing a laser beam towards a nanoparticle/nanowire defect, scattering of the incident beam by the defect was used to excite SPPs. The periodicity of the surface undulations (height) was tuned for a given angle of incidence to satisfy Bragg's condition, which resulted in a

very large reflection (90%) of the SPP wave. The experimental evidence from the above investigations suggested that passive optical elements can be easily fabricated for applications such as SPP mirrors and beam-splitters. The fulfilment of Bragg's condition using a metallised grating structure is discussed in more detail in the next chapter.

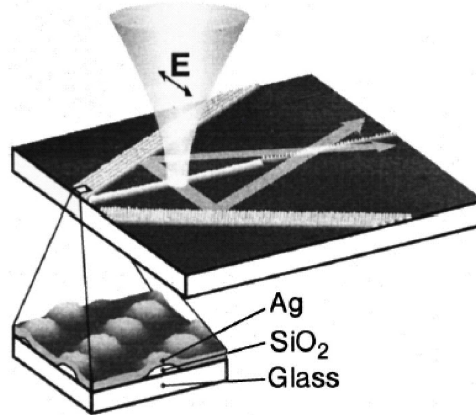

Figure 1.5: Shows the propagation route of SPPs over a planar silver film comprising surface modulation. The micrograph shows an enlarged view of a sample of a Bragg reflector comprising lines of regularly spaced height modulations [42].

An optical far-to-near field conversion for coupling nanophotonic to conventional photonic devices was demonstrated by Nomura et. al [43], in which a grating coupler was used to couple the incoming light in order to excite SPPs (see Figure 1.6). An SPP condenser (several hemispherical submicron metallic particles) was used, which scatters and focuses SPPs towards a nanodot coupler comprising a linear array of nanoparticles. Here, the SPP condenser aids conversion of the far-field propagating SPPs into the optical near-field by efficiently exciting localised surface plasmons (SPs) in the nanodot coupler. Due to efficient coupling between the localised SPs in the neighbouring nanoparticles of the nanodot coupler, the propagation length of the focused SPPs along the nanodot coupler was found to be three times larger than that in a planar metal-dielectric waveguide.

Experimental realisation of the excitation and propagation of SPPs along a thin

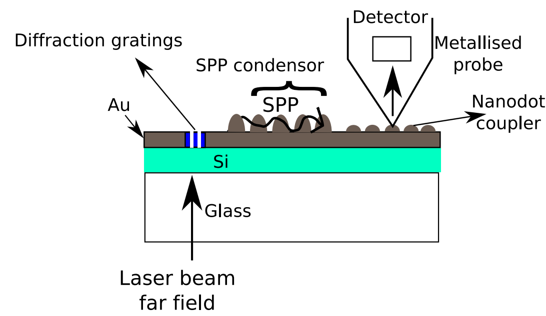

Figure 1.6: Experimental setup of the nanodot coupler with SPP condenser for optical far/near field conversion [43].

metal stripe waveguide has also been demonstrated by Lamprecht et al. as illustrated in Figure 1.7 [30]. Here, an aluminium screen was used to provide separation between the excitation and measurement regions, so that the light incident upon the excitation region does not affect the SPP propagation in the measurement region. SPPs were excited along the metal stripe waveguide using the Kretschmann prism technique, and then propagated towards the measurement region, where they were locally scattered by the surface corrugations of the stripe originating from the metal evaporation process. The propagation length of the SPPs was measured using a conventional optical microscope by detecting the stray light generated due to the scattering of the SPPs.

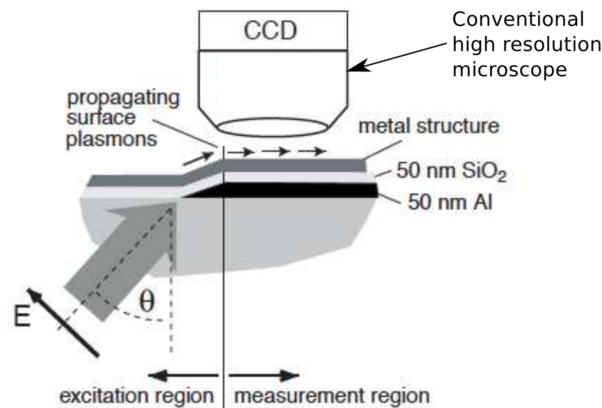

Figure 1.7: Schematic illustration of the experimental setup for the excitation and measurement of SPPs propagating along the thin metal stripe waveguide [30].

Using a similar configuration, the application of metal nanowires as optical waveguides for transporting SPPs, was demonstrated by Krenn et al. as shown in Figure 1.8 [32]. In this case, SPPs were excited in a wide metal stripe waveguide using the Kretschmann technique, which were then tapered into a metal nanowire waveguide (200nm wide, 50nm high) in order to excite the nanowire locally. Direct imaging of the SPP's near-field along the metal nanowire was carried out using subwavelength resolution photon scanning tunnelling microscopy (PSTM), in which part of the near field sample (of SPPs) was picked up by the fibre tip in order to guide it towards the detector. The PSTM measurements revealed that the light was transported along the metal nanowire over a distance of a few microns ($\approx 2.5\mu$m). Although the SPP propagation length was limited due to damping by the metal, this distance is sufficient for integrating nanophotonics and electronics for short signal paths.

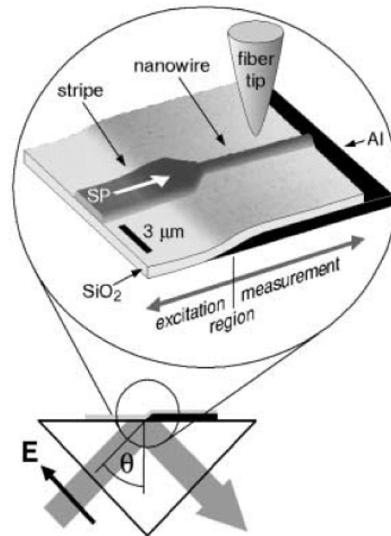

Figure 1.8: Schematic of the experimental setup used by Krenn et. al. [32] for the local excitation of surface plasmons and subsequently coupling them via the tapered structure into the metal nanowire, where the strip SPP excites plasmons locally along the nanowire.

In order to integrate photonic and electronic-based circuits, a common silicon-based

platform is necessary, and therefore it becomes desirable to develop nanophotonic devices which are compatible with standard complementary-metal-oxide-semiconductor (CMOS) processing technology. Another motivation for developing Si-based plasmonic devices is that photonic components are restricted in size to about half the incident light wavelength, which then poses serious challenge for researchers to integrate them with CMOS nanoscale electronics. On the other hand, silicon-compatible plasmonic devices would provide micron-scale footprints due to the highly confined nature of SPPs at the metal-dielectric interface [44, 45]. Hence, numerous silicon-based plasmonic devices for optoelectronic applications have been theoretically and experimentally investigated, including but not limited to, waveguides, multiplexers/demultiplexers, switches, modulators, and detectors [46–52].

A silicon-based plasmonic waveguide was theoretically investigated, in which the structure comprises periodically arranged metal nanoparticles on a thin silicon-on-insulator substrate [35]. The periodicity of the metal nanoparticles was optimised so that the excited surface plasmons efficiently overlap with the fundamental mode of the fibre taper waveguide situated at a particular height above the metal nanoplasmonic waveguide. In this way, maximum coupling between the excited SPPs and the fundamental mode of the taper waveguide occurs, and therefore maximum power transfer (up to 90%) between the two can be achieved for an optimised taper length. Such a plasmonic structure can be used for applications such as energy guiding, optical sensing, and switching.

In other applications, optical power splitters/couplers based on the multimode interference (MMI) effect and self-imaging have been theoretically and experimentally demonstrated [53–55]. For example, a metal-insulator-metal (MIM) structure was proposed, in which the real part of the effective mode index was tailored in a index-guided multimode plasmonic waveguide to achieve a subwavelength MMI effect, and the effect was subsequently used to investigate 1x2 splitting functionality. A plasmonic waveguide structure comprising a cylindrical silicon waveguide embedded in a low permittivity dielectric layer near the metal surface was recently proposed [47]. The diameter of the

semiconductor nanowire and spacing between the cylindrical waveguide and metal surface was optimised to achieve a controlled propagation length. It was found that a hybrid plasmonic mode exists between the cylinder and the adjacent metal-dielectric interface, whose propagation length far exceeded that of SPPs along an equivalent metal-dielectric interface. The low permittivity gap layer enabled the confinement of the electromagnetic energy of the hybrid mode, leading to subwavelength optical guiding with low loss. Moreover, a hybrid dielectric-loaded plasmonic waveguide was also investigated as a wavelength-selective ring resonator and multiplexer [56]. The structure comprised an SiO_2 film sandwiched between a silicon nanowire and a metal film with air cladding, as shown in Figure 1.9. The energy of the fundamental mode supported by the structure was mostly confined in the thin oxide layer. The structure was used as a bus waveguide in order to achieve optical coupling with a very small ring resonator waveguide (1 to 2 μm diameter) placed in close proximity (200 nm) to it.

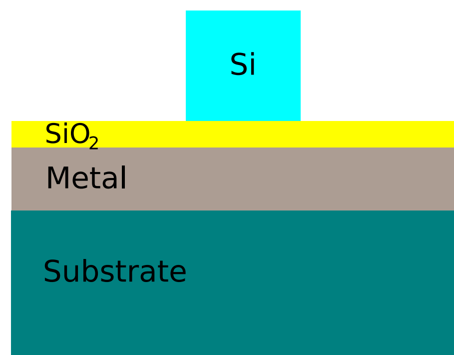

Figure 1.9: Schematic cross sectional view of a hybrid dielectric-loaded plasmonic waveguide, in which most of the energy density of the hybrid mode exists in the low index oxide layer.

Apart from the above applications, researchers have demonstrated that the dissipation loss due to the absorption of light by the metals can be mitigated by using gain materials, which are located in close proximity to the metal surface for applications such as nanoplasmonic lasers [57]. The enhanced electric field intensities associated with the localised surface plasmon excitation on the surface of plasmonic nanostructures strongly

modifies the radiative and nonradiative properties of the emitter, and therefore such nanostructures behave as nanoantennas [58]. These nanostructures, when assembled in a particular fashion, may exhibit unusual optical properties, such as negative refractive index at near-infrared and visible light frequencies, which leads to negative refraction that can be utilise to possibly stop or localise light pulses [59, 60].

1.3 Structure of the thesis

In the following chapter, the electromagnetic response and optical properties of metals in different frequency regimes are discussed. The theory behind the condition to achieve confined SPPs in a planar metal-dielectric structure is discussed. The confinement nature of the SPPs in insulator-metal-insulator and metal-insulator-metal structures are also discussed. In the next subsection of the chapter, a simple grating structure is considered to investigate the optical confinement of SPPs within the structure in comparison within the structure without any metal gratings. Additionally, the structure is investigated to achieve SPP dispersion along with the light lines of air and silica, and the condition to achieve slow light effect is also discussed.

Chapter three explores the application of plasmonics in a metallised cavity structure for an optical modulation purpose using two-dimensional electromagnetic modelling. Assuming that the structure is filled with an optically active material, the resonance within the cavity can be controlled by altering the imaginary part of the refractive index of the material, which modifies the system transmission between the biased and unbiased states. Chapter four extends the investigation of the above plasmonic structure using a complete three dimensional modelling.

In chapter five, performance analysis of a conductor-gap-dielectric system supporting a gap plasmon mode within a low index dielectric layer sandwiched between a conductor and a high index dielectric layer was studied for optical modulation purpose. Additionally, the subwavelength confinement nature of SPP modes in a metal-oxide-semiconductor plasmonic structure is theoretically investigated for optical modulation

purposes. When a bias is applied, the formation of accumulation charge layers near the metal-insulator-semiconductor junction creates large variation of the effective index of the plasmon mode, which eventually enables one to achieve very short device length.

In chapter six, the performance of periodically arranged metallised nanostructures for effective coupling of light via coherent focusing of SPPs, into a nano-sized aperture is theoretically investigated. The structure could be used for coupling directly from a wide fibre grating opening into a nano-plasmonic or a silicon-on-insulator (SOI) dielectric waveguide. Finally, in chapter seven, a brief summary of the work carried out is described, and suggestions for future work is stated.

Chapter 2

Theory of surface plasmon polaritons

2.1 The optical properties of metals

Metals behave differently with respect to different parts of the electromagnetic spectrum of the incident light. They are highly reflective for frequencies up to the visible part of the spectrum, preventing light from penetrating them, which is why, for lower frequencies, they are generally considered as good conductors [61, 62]. On the other hand, for near-infrared and higher frequencies, the amount of field penetration of the incident light into metals increases significantly, resulting in increased absorption of the light. At ultra-violet frequencies, metals behave as dielectric media, allowing electromagnetic waves to propagate through them with different degrees of attenuation. For noble metals, such as gold or silver, strong absorption between electronic bands due to inter-band transition occur, which is why they tend to be very lossy in this regime.

The dispersive properties of metals can be described by a complex dielectric function $\epsilon(\omega)$, which is related to the conductivity σ as:

$$\epsilon(\omega) = 1 + \frac{i\sigma(K,\omega)}{\epsilon_0\omega} \tag{2.1}$$

where ω is the angular frequency of an incident plane wave, $\mathbf{K}$ is the wavevector and ϵ_0 is permittivity of the vacuum. $\epsilon(\omega)$ can be separated into real and imaginary parts, ϵ_{re} and ϵ_{im}, which are related to the complex refractive index $n(\omega)$= n(ω) + i$\kappa(\omega)$ via:

$$\epsilon_{re} = n^2 - \kappa^2, \tag{2.2}$$

$$\epsilon_{im} = 2n\kappa \tag{2.3}$$

$$n^2 = \frac{\epsilon_{re}}{2} + \frac{1}{2}\sqrt{\epsilon_{re}^2 + \epsilon_{im}^2} \tag{2.4}$$

$$\kappa = \frac{\epsilon_{im}}{2n} \tag{2.5}$$

where κ is the extinction coefficient which determines the amount of optical absorption of the EM waves propagating through the medium. This is also related to the absorption coefficient (α) as: $\alpha(\omega)= \frac{4\pi}{\lambda_0}\kappa(\omega)$, where λ_0 is the free space wavelength. The basic physics involving the optical response of metals lies in the change in the phase of the induced currents with respect to the driving field at a particular frequency. This is explained by the plasma model, which is also known as the Drude model. The Drude model is a classical approximation, in which a 'gas' of free electrons in a material oscillates in response to the applied EM field, and their motion is damped due to collisions occurring at a characteristic collision frequency $\gamma=\frac{1}{\tau}$. The relaxation time τ of free electrons is typically on the order of 10^{-14}s at room temperature, which corresponds to γ=100THz. The motion of these free electrons subjected to an external electric field $\mathbf{E}$ (Figure 2.1) can be described via the basic force expression as:

$$m\ddot{\mathbf{x}} + m\gamma\dot{\mathbf{x}} = -e\mathbf{E} \tag{2.6}$$

where the second term in the expression results from the collision of the displaced electrons (of mass m) with positive ions within the metal.

Assuming a harmonic time dependence of the applied electric field, $E(t) = E_0e^{-i\omega t}$, the solution of the Eq. 2.6 can be obtained, which describes the electron oscillations as:

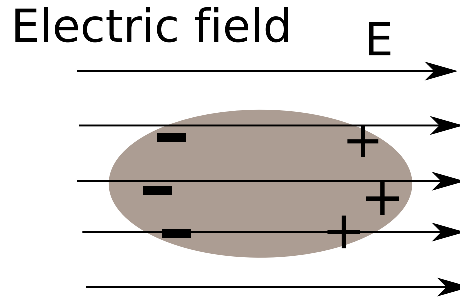

Figure 2.1: Schematic diagram of the sea of electrons subjected to an external electric field **E**, resulting in a macroscopic polarisation **P**.

$$x(t) = x_0 e^{-i\omega t}. \tag{2.7}$$

Here x_0 denotes the complex amplitude which includes any phase shift incurred between the driving field and response. Using Eq. 2.7, Eq.2.1 can be solved, which gives x_0 as:

$$x(t) = \frac{e}{m(\omega^2 + i\gamma\omega)} E(t) \tag{2.8}$$

The macroscopic polarisation $P = -ne\mathbf{x}$ due to the displaced electrons is then given by :

$$\mathbf{P} = -\frac{ne^2}{m(\omega^2 + i\gamma\omega)} \mathbf{E} \tag{2.9}$$

The dielectric displacement **D** due to an applied electric field **E** is related to polarisation **P** by:

$$\mathbf{D} = \epsilon_0 \mathbf{E} + \mathbf{P} \tag{2.10}$$

$$\mathbf{D} = \epsilon_0 (1 - \frac{\omega_p^2}{\omega^2 + i\gamma\omega}) \mathbf{E} \tag{2.11}$$

where $\omega_p^2 = \frac{ne^2}{\epsilon_0 m}$ is the plasma frequency of the free electron gas. Since $\mathbf{D} = \epsilon_0 \epsilon \mathbf{P}$, the dielectric function of the electron gas can therefore be written as [61–63]:

$$\epsilon(\omega) = 1 - \frac{\omega_p^2}{\omega^2 + i\gamma\omega} \tag{2.12}$$

The above equation can be separated into real and imaginary parts, $\epsilon(\omega) = \epsilon_{re}(\omega) + i\epsilon_{im}(\omega)$ given by [61]:

$$\epsilon_{re}(\omega) = 1 - \frac{\omega_p^2\tau^2}{1 + \omega^2\tau^2} \tag{2.13}$$

$$\epsilon_{im}(\omega) = \frac{\omega_p^2\tau^2}{\omega(1 + \omega^2\tau^2)} \tag{2.14}$$

where $\gamma = 1/\tau$ is used. It is insightful to study Eq. 2.12 for different frequency regimes with respect to the plasma frequency: i.e for $\omega < \omega_p$ and $\omega > \omega_p$. For high frequencies close to ω_p such that $\omega\tau \gg 1$, then $\epsilon(\omega)$ is predominantly real with negligible damping, in which case:

$$\epsilon(\omega) = 1 - \frac{\omega_p^2}{\omega^2} \tag{2.15}$$

It can be observed from the above equation that at frequencies less than the plasma frequency ω_p, the dielectric permittivity of the metals is negative, i.e the plasma of the excited electrons shields the interior of metals from the external applied field. Thus, metals (such as silver) in this regime tend to provide very low resistance to the external field, and therefore have a good conductivity [64, 65]. For frequencies larger than the plasma frequency, metals behave as a dielectric material with positive permittivity.

For very low frequencies where $\omega\tau \ll 1$, and therefore $\epsilon_{im} \gg \epsilon_{re}$, the metals are mostly absorbing. The above Drude model assumes an ideal lossless metal, in which the incident photon energy is lower than the band gap energy. At $\omega \gg \omega_p$, $\epsilon \to 1$ in the free electron model (see Eq. 2.15). At $\omega > \omega_p$, in noble metals such as gold, silver and copper,

an extension of this model is required because the validity of the Drude model breaks down due to interband electron transitions, in which electrons from the filled band below the Fermi level are excited to higher bands. This cause a highly polarised environment which is required to be included in the dielectric function of the free electron model as:

$$\epsilon(\omega) = \epsilon_\infty - \frac{\omega_p^2}{\omega^2 + i\gamma\omega} \tag{2.16}$$

where ϵ_∞ describe the effect caused due to the residual polarisation. The Drude free electron model described by Eq. 2.16 can be used for analysing the optical response of the metals for photon energies below the threshold for transitions between electron bands. The inter-band transitions of electrons begins to appear for frequencies greater than or equal to visible light frequencies for which increased absorption of the EM field is observed. When the oscillation of the plasma of electrons on a metal surface couples with the incident electromagnetic waves, it gives rise to SPPs. SPPs are EM waves which are confined at the interface between a conductor and a dielectric medium, and evanescently decay in the direction perpendicular to the interface [7, 61]. In the next section, we will see how Maxwell's equations can be applied to a simple metal-dielectric interface to obtain the electric and magnetic field equations that describe the surface plasmon EM waves.

2.2 Surface plasmon polaritons at metal-dielectric interfaces

In this section, the conditions for the existence of SPPs at a metal-dielectric interface are explored. The macroscopic Maxwell's equations can be easily applied to obtain the electromagnetic response of metals. This approach assumes that microscopic variation in the field are averaged over distances much larger than the microstructure, and therefore neglects the details of the fundamental interactions between the charged particles inside the media [61]. The two Maxwell curl equations are as follows:

$$\nabla \times \mathbf{E} = -\frac{\partial \mathbf{B}}{\partial t} \tag{2.17}$$

$$\nabla \times \mathbf{H} = \frac{\partial \mathbf{D}}{\partial t} \tag{2.18}$$

Now taking the curl of Eq. 2.17 and using $\mathbf{B} = \mu_0 \mathbf{H}$ (where μ_0 is the magnetic permeability of free space):

$$\nabla \times (\nabla \times \mathbf{E}) = -\nabla \times \frac{\partial \mathbf{B}}{\partial t} \tag{2.19}$$

$$= -\mu_0 \frac{\partial (\nabla \times \mathbf{H})}{\partial t} \tag{2.20}$$

$$= -\mu_0 \frac{\partial^2 \mathbf{D}}{\partial t^2} \tag{2.21}$$

By using the identities $\nabla \times (\nabla \times \mathbf{E}) \equiv \nabla(\nabla \cdot \mathbf{E})$ - $\nabla^2 \mathbf{E}$ and $\nabla \cdot (\epsilon \mathbf{E}) \equiv \nabla(\nabla \cdot \mathbf{E}) - \nabla^2 \mathbf{E}$, and due to the absence of an external charge ($\nabla \cdot \mathbf{D} = 0$), Eq. 2.21 can be rewritten as:

$$\nabla \left(-\frac{1}{\epsilon} \mathbf{E} \cdot \nabla \epsilon \right) - \nabla^2 \mathbf{E} = -\mu_0 \epsilon \epsilon_0 \frac{\partial^2 \mathbf{E}}{\partial t^2} \tag{2.22}$$

Assuming that the dielectric permittivity does not vary over a distance of the order of one incident wavelength along the propagation direction ($\nabla \epsilon = 0$), Eq. 2.22 reduces to the fundamental wave equation [61]:

$$\nabla^2 \mathbf{E} - \frac{\epsilon}{c^2} \frac{\partial^2 \mathbf{E}}{\partial t^2} = 0 \tag{2.23}$$

where $c = \frac{1}{\sqrt{\mu_0 \epsilon_0}}$ is the speed of light in free space.

In order to find confined propagating wave solutions at the metal-dielectric interface, a harmonic time dependence of electric field in space is assumed such that $\mathbf{E}(\mathbf{r}, t) = \mathbf{E}(\mathbf{r}) e^{-i\omega t}$, which is then inserted in Eq. 2.23:

$$\nabla^2 \mathbf{E} + k_0^2 \epsilon \mathbf{E} = 0 \tag{2.24}$$

where $k_0 = \frac{w}{c}$ is the wave vector of the propagating wave in free space. Figure 2.2

shows a metal-dielectric planar structure, in which the EM wave propagates in the x direction, and ϵ varies only in one dimension (i.e. the z-direction). In the simple planar structure, the plane at $z = 0$ comprising a metal-dielectric (air) interface will sustain the propagating EM waves. The electric field of the EM wave propagating in the x direction can be written as $\mathbf{E}(x, y, z) = \mathbf{E}(z)e^{i\gamma x}$ where $\gamma = k_x$ is the complex propagation constant of the EM wave in the direction of propagation [61].

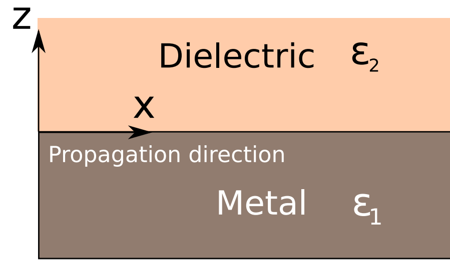

Figure 2.2: Schematic diagram of a planar waveguide in which the EM wave propagates in the x-direction.

Inserting $\mathbf{E}(x, y, z)$ into Eq. 2.24 results in [61],

$$\frac{\partial^2 \mathbf{E}(z)}{\partial z^2} + (k_0^2 \epsilon - \gamma^2)\mathbf{E} = 0. \tag{2.25}$$

An equation similar to this exists for the magnetic field $\mathbf{H}$ as well. Equation 2.25 represents the basic equation for guided EM modes in planar waveguides. This equation can be used to obtain the spatial field profile and dispersion relation, in which case it can be resolved into separate field components of $\mathbf{E}$ and $\mathbf{H}$. This can be obtained by using the curl of equations 2.17 and 2.18, which results in individual electric and magnetic field components of E_x, E_y, E_z and $H_x, H_y H_z$ [61]. For the planar structure shown in Figure 2.2, the propagation along the x-direction and homogeneity along the y-direction means that $\frac{\partial}{\partial y} = 0$ and $\frac{\partial}{\partial x} = i\gamma$, and therefore a reduced system of equations can be obtained [61]. The reduced equations can be further divided into two sets of self-contained equations depending upon the polarisation of the incident EM wave. For

the TM polarised modes along the x-direction, only the field component E_x, E_z and H_y are non-zero, and are related by the following set of equations [61]:

$$E_x = -i\frac{1}{\omega\epsilon_0\epsilon}\frac{\partial H_y}{\partial z}, \quad (2.26)$$

$$E_z = -\frac{\gamma}{\omega\epsilon_0\epsilon}H_y \quad (2.27)$$

where the wave equation for the TM mode is

$$\frac{\partial^2 H_y}{\partial z^2} + (k_0^2\epsilon - \gamma^2)H_y = 0 \quad (2.28)$$

A similar set of equations can be obtained for the TE polarised modes, in which only the field components H_x, H_z and E_y are non-zero.

In order to find the SPP EM wave solutions at the metal-dielectric interface, the solutions in the x-direction can be found for $z > 0$ and $z < 0$ in the conducting metal and dielectric space regions (Figure 2.2). Using Eq. 2.28 in both halves yields:

$$H_y(z) = A_2 e^{i\gamma x} e^{-k_2 z} \quad (2.29)$$

$$E_x(z) = iA_2\frac{1}{\omega\epsilon_0\epsilon_2}k_2 e^{i\gamma x} e^{-k_2 z} \quad (2.30)$$

$$E_z(z) = -A_2\frac{\gamma}{\omega\epsilon_0\epsilon_2}e^{i\gamma x} e^{-k_2 z} \quad (2.31)$$

for $z > 0$ and

$$H_y(z) = A_1 e^{i\gamma x} e^{k_1 z} \quad (2.32)$$

$$E_x(z) = iA_1\frac{1}{\omega\epsilon_0\epsilon_1}k_1 e^{i\gamma x} e^{k_1 z} \quad (2.33)$$

$$E_z(z) = -A_1\frac{\gamma}{\omega\epsilon_0\epsilon_1}e^{i\gamma x} e^{k_1 z} \quad (2.34)$$

for $z < 0$. Here $k_i \equiv k_{z,i} (i = 1, 2)$ is the wavevector component perpendicular to

the metal-dielectric interface and A_1, A_2 are the respective electric and magnetic field coefficients. Equations 2.31 and 2.34 show the electric field components of a TM mode which are confined at the metal-dielectric interface (if $\mathrm{k}_1 > 0$ and $\mathrm{k}_2 > 0$), and decay in a direction perpendicular to it (i.e z-direction). The reciprocal of the wavevector, $\hat{z} = \mid k_z \mid^{-1}$ defines the decay length of the fields perpendicular to the interface which quantifies the wave confinement, also known as the skin depth. At the interface (i.e at z=0), $H_y(z)$ and $E_x(z)$ are continuous, which leads to $A_1 = A_2$ and

$$\frac{k_2}{k_1} = -\frac{\epsilon_2}{\epsilon_1} \tag{2.35}$$

It must be noted from the sign conventions used in describing equations 2.29 to 2.34, that the confinement of the EM wave at the interface requires $\mathrm{Re}[\epsilon_1] < 0$, which would result in a maximum electric field intensity at the surface. Hence, the surface wave exists only in heterostructures of materials with the opposite signs of the real part of their dielectric permittivities.

The magnetic field H_y satisfies the wave equation 2.28, which yields,

$$k_1^2 = \gamma^2 - k_0^2\epsilon_1 \tag{2.36}$$

$$k_2^2 = \gamma^2 - k_0^2\epsilon_2 \tag{2.37}$$

The above equations combined with Eq. 2.35 can be used to obtain the dispersion relation of the SPPs at a metal-dielectric interface [61, 66]:

$$\gamma = k_{SPP} = k_0\sqrt{\frac{\epsilon_1\epsilon_2}{\epsilon_1 + \epsilon_2}} \tag{2.38}$$

where k_{SPP} corresponds to the component of the wave vector of the SPPs in the direction of propagation.

Similarly, the transverse electric (TE) polarised mode proceeds by satisfying the continuity of E_y and H_x at the interface, leading to the following condition:

$$A_1(k_1 + k_2) = 0 \tag{2.39}$$

In this case, the confinement of the EM wave at the interface requires $\mathbf{Re}[k_1] > 0$ and $\mathbf{Re}[k_2] > 0$, which can be achieved only if $A_1 = 0$. This leads to $A_1 = A_2 = 0$, which is possible but is trivial. Hence, no surface modes exist for TE polarisation, but only for TM polarisation [61].

2.3 Dispersion relation of SPPs at a metal-dielectric interface

The dispersion relation defines the variation of the material's refractive index with frequency of the incident light. Equation 2.38 gives the Drude dielectric function of an undamped free electron plasma (i.e it assumes lossless metals). Figure 2.3 shows a schematic dispersion of SPPs at the interface of a metal with negligible damping (Eq. 2.12) having a dielectric function given by Eq. 2.38 with air ($\epsilon_1 = 1$), and fused silica ($\epsilon_2 = 2.25$) as a dielectric medium [61]. The two linear curves show the light lines in air and silica, and the two curves at the right of their corresponding light lines shows the SPP excitation. Thus it can be seen from the figure that due to the mismatch of the wavevectors between the light line and SPPs curves, special phase matching techniques are required to excite SPPs [61]. These phase matching techniques can be provided by altering the surface of the metals, for example by introducing defects, which is discussed later in this chapter.

For mid-infrared and lower frequencies (or small wavevectors), the SPPs propagation constant is closer to the wavevectors of the respective light lines [61] and the EM waves extend over many wavelengths into the dielectric space. In this regime, the SPPs behave as Sommerfeld-Zenneck waves as they tend to propagate parallel to the metal-dielectric interface [61]. At large wavevectors, the frequency of the SPP approaches the surface plasmon frequency ω_{sp} given by $\omega_{sp} = \frac{\omega_p}{\sqrt{1+\epsilon_2}}$, and at the limit of negligible damping (i.e $\mathrm{Im}[\epsilon_1{=}0]$), the SPP propagation constant approaches infinity, which results in the group velocity $v_g \rightarrow 0$ [61]. Thus, in this frequency regime the mode acquires an electrostatic character and is known as surface plasmon.

Figure 2.3 assumes an ideal lossless metal to have the dispersion relation described

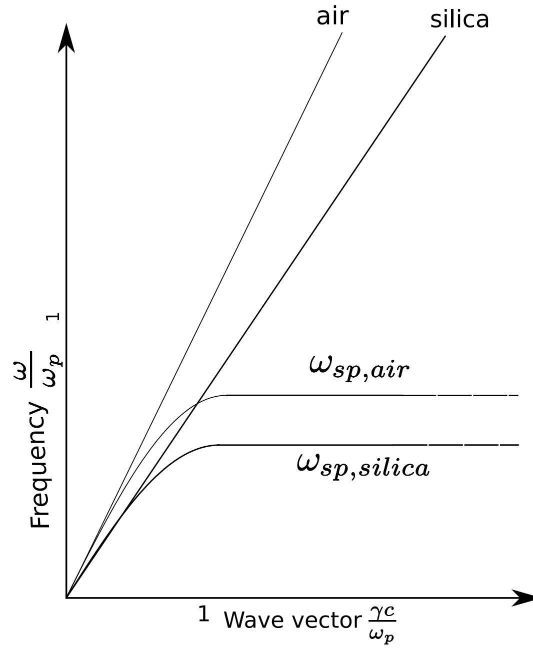

Figure 2.3: Schematic dispersion relation of the SPPs between an ideal metal with negligible absorption and air and SiO_2 [61].

by Eq. 2.15 in the previous section. However, real metals such as gold or silver suffer from inter-band transitions, which lead to increased damping, and therefore increased absorption of the EM waves by the metal surface. Due to the complex permittivity of real metals, the SPP propagation constant is also complex and therefore propagation along the metal-dielectric interface is damped with the degree of attenuation depending upon the type of materials used. The SPP propagation length is given by $L = (2[Im(\gamma)])^{-1}$.

Figure 2.4 shows the schematic diagram of the dispersion relation of the SPPs propagating along a silver-SiO_2 interface, in which case k_{SPP} approaches a finite value at the surface plasmon frequency, ω_{sp} [61]. This restricts the SPP wavelength which is given by $\lambda_{SPP} = 2\pi/Re[\gamma]$. Both the propagation length L and energy confinement (quantified by $\hat{z}$) in the dielectric show a strong dependence on frequency. SPPs at frequencies close to ω_{sp} exhibit large field confinement close to the interface but a smaller propagation length due to increased damping. Hence, a tradeoff between the SPP mode confinement and propagation length can be observed, as discussed further in the following section [61].

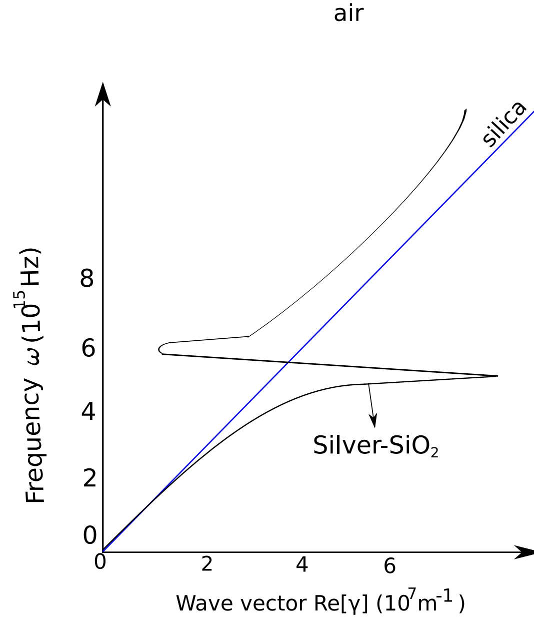

Figure 2.4: Dispersion relation of the SPPs between a simple Silver-SiO_2 interface ([61]).

2.4 Multilayer plasmonic systems

In this section, the solution of Maxwell's equations for EM waves confined in a three layer system comprising an insulator-metal-insulator (IMI) structure as shown in Figure 2.5 is considered. The metal is sandwiched between the two thick dielectric or insulator cladding layers.

A TM polarised mode propagating in the x-direction and confined to the metal-dielectric interface is considered. Using the fundamental wave equation (Eq. 2.22), the electric and magnetic field components of the mode in the region z> a can be written as:

$$H_y = Ae^{i\gamma x}e^{-k_3 z} \tag{2.40}$$

$$E_x = iA\frac{1}{\omega\epsilon_0\epsilon_3}k_3 e^{i\gamma x}e^{-k_3 z} \tag{2.41}$$

$$E_z = -iA\frac{\gamma}{\omega\epsilon_0\epsilon_3}e^{i\gamma x}e^{-k_3 z} \tag{2.42}$$

and for z< $-a$

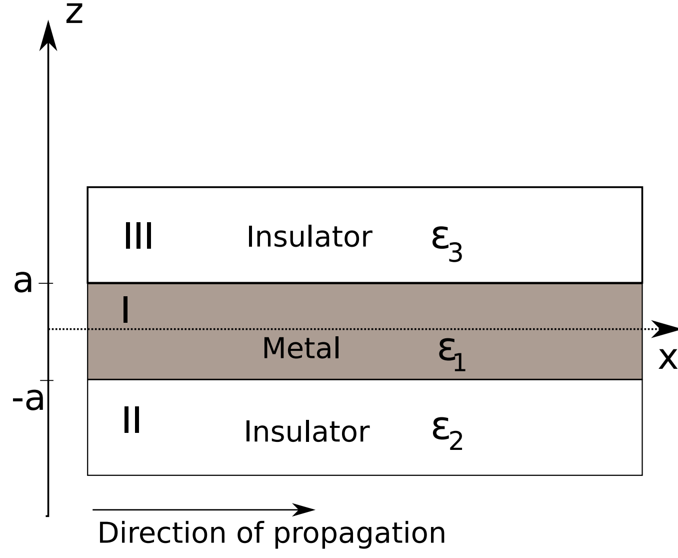

Figure 2.5: Schematic diagram of a three layer IMI system comprising a thin metal layer (I) sandwiched between two infinite half spaces (insulator layers) II and III.

$$H_y = Be^{i\gamma x}e^{k_2 z} \tag{2.43}$$

$$E_x = -iB\frac{1}{\omega\epsilon_0\epsilon_2}k_2 e^{i\gamma x}e^{k_2 z} \tag{2.44}$$

$$E_z = -B\frac{\gamma}{\omega\epsilon_0\epsilon_2}e^{i\gamma x}e^{k_2 z} \tag{2.45}$$

In the region $-a < \mathrm{z} < a$, both exponential field components of the TM mode exist, since the metal layer is of finite thickness, and the field equations can be written as:

$$H_y = Ce^{i\gamma x}e^{k_1 z} + De^{i\gamma x}e^{-k_1 z} \tag{2.46}$$

$$E_x = -iC\frac{1}{\omega\epsilon_0\epsilon_1}k_1 e^{i\gamma x}e^{k_1 z} + iD\frac{1}{\omega\epsilon_0\epsilon_1}k_1 e^{i\gamma x}e^{-k_1 z} \tag{2.47}$$

$$E_z = C\frac{\gamma}{\omega\epsilon_0\epsilon_1}e^{i\gamma x}e^{k_1 z} + D\frac{\gamma}{\omega\epsilon_0\epsilon_1}e^{i\gamma x}e^{-k_1 z} \tag{2.48}$$

Assuming that the dielectric permittivities in the regions II and III are equal, i.e. $\epsilon_2 = \epsilon_3$ and $k_2 = k_3$, then the continuity of H_y and E_x at each interface of the three layer system leads to a set of four linear equations relating A, B, C and D as:

$$\begin{aligned}
Ae^{-k_2 a} - Ce^{k_1 a} &= De^{-k_1 a} &(2.49)\\
\frac{A}{\epsilon_2}k_2 e^{-k_2 a} + \frac{C}{\epsilon_1}k_1 e^{k_1 a} &= \frac{D}{\epsilon_1}k_1 e^{-k_1 a} &(2.50)\\
Be^{-k_2 a} - Ce^{-k_1 a} &= De^{k_1 a} &(2.51)\\
-\frac{B}{\epsilon_2}k_2 e^{-k_2 a} + \frac{C}{\epsilon_1}k_1 e^{-k_1 a} &= \frac{D}{\epsilon_1}k_1 e^{k_1 a} &(2.52)
\end{aligned}$$

As mentioned in the previous section, the H_y component of the TM mode also satisfies the wave equation in the three regions, which leads to

$$k_i^2 = \gamma^2 - k_0^2 \epsilon_i \tag{2.53}$$

where k_i for i= 1,2,3 represents the wavevectors in the three layer system.

The above equations can be solved by using an initial value of $D = 1$, whereupon they reduce to the following set of equations:

$$\begin{pmatrix} e^{-k_2 a} & 0 & -e^{k_1 a} \\ \frac{k_2}{\varepsilon_2} e^{-k_2 a} & 0 & \frac{k_1}{\varepsilon_1} e^{k_1 a} \\ 0 & e^{-k_2 a} & -e^{k_1 a} \end{pmatrix} \begin{pmatrix} A \\ B \\ C \end{pmatrix} = \begin{pmatrix} e^{-k_1 a} \\ \frac{k_1}{\varepsilon_1} e^{-k_1 a} \\ e^{k_1 a}. \end{pmatrix} \tag{2.54}$$

This can be further reduced to:

$$e^{-4k_1 a} = \frac{(k_1/\varepsilon_1 + k_2/\varepsilon_2)^2}{(k_1/\varepsilon_1 - k_2/\varepsilon_2)^2}. \tag{2.55}$$

which can be separated into two sets of equations as

$$\begin{aligned}
\tanh(k_1 a) &= -\frac{k_2 \epsilon_1}{k_1 \epsilon_2} &(2.56)\\
\tanh(k_2 a) &= -\frac{k_1 \epsilon_2}{k_2 \epsilon_1}. &(2.57)
\end{aligned}$$

The above equations represent the dispersion relations describing the confined EM modes within the IMI structure (Figure 2.5). Equation 2.56 describes odd parity modes

as E_x(z) is odd while $H_y(z)$ and $E_z(z)$ are even functions. Similarly, Eq. 2.57 describes even parity modes as $E_x(z)$ is even, and $H_y(z)$ and $E_z(z)$ are odd [61]. In order to analyse the behaviour of the electric and magnetic fields at the IMI interface (Figure 2.5), a lossless case with Re[ϵ_{Au}] = -95.92, and a lossy case with complex ϵ_{Au} = -95.92 +i10.97 at a free space wavelength (λ_0) = 1.55μm were considered [67].

Using only the real value of ϵ_{Au}, the propagation constant γ between the 10nm thick Au and air interface was numerically calculated to determine even parity EM modes. This value was then inserted in Eq. 2.53 to calculate the wavevectors k_1 and k_2, which were used in Eq. 2.54 to determine the coefficients A, B and C. These coefficients and the wavevectors were then employed in equations 2.42 and 2.45 to determine the field components H_y, E_x and E_z for $z > a$ and $z < -a$. Figure 2.6 shows the even parity electric and magnetic fields along the distance perpendicular to the metal-dielectric interface (i.e z-direction) for the lossless case. The figure indicates that both the electric and magnetic fields have a maximum at the metal-dielectric interfaces (at z=a and z=$-a$), and decay exponentially from the interface, thereby demonstrating their confinement to it.

Figures 2.7 and 2.8 show the behaviour of odd and even modes of SPP electric and magnetic fields at a gold-air interface using the complex permittivity of gold. Similar to the lossless metal situation, the figures indicate that the SPP field components decay exponentially away from the interface with their maximum values located at the interface. Due to the absorption by the metal, which in turn is due to the complex permittivity, the length to which both the electric and magnetic field extend into the dielectric space (Figure 2.8) is reduced. Moreover, the large mode confinement at the interface also affects the SPP propagation length. The propagation length decreases as the mode confinement increases, demonstrating a trade-off between the SPP mode confinement and propagation length which is generally observed in plasmonic structures [61].

In an alternative MIM structure, an insulator layer (I) is sandwiched between the two metal layers (II and III). The SPP electric and magnetic field components can be obtained in the manner described for the IMI system by replacing ϵ_2=ϵ_3= $\epsilon_2(\omega)$, and ϵ_1 as the dielectric permittivity of an insulating layer. Figure 2.9 shows the odd modes of

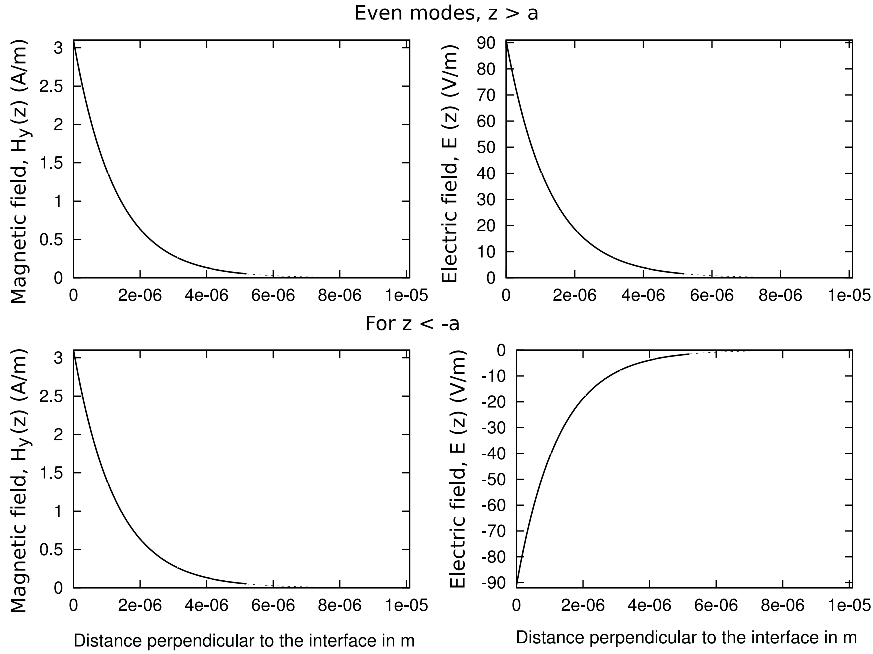

Figure 2.6: Even modes of electric and magnetic fields perpendicular to the interface for z $> a$ for real value of permittivity, $\varepsilon_{Au} = 95.92$

electric and magnetic field components existing in an Au-air (20nm)-Au structure. Very large electric and magnetic field maximum values of the confined EM mode at the metal-dielectric interface were obtained, which decay exponentially into the metal regions with very small penetration depth.

Thus, MIM based plasmonic structures can exhibit very large EM field confinement, which could eventually result in achieving very small device dimensions. However, such a plasmonic structure experiences a large insertion loss due to absorption by the metal layers. A special case of conductor-gap-dielectric system will be discussed in chapter five. In the next section, the confinement of SPP and dielectric waveguide modes within

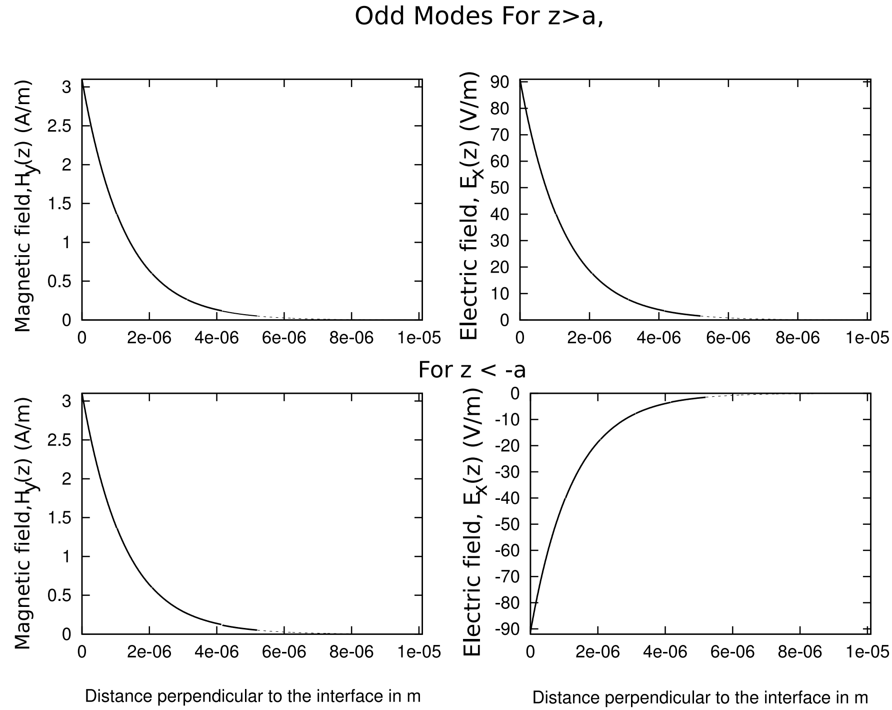

Figure 2.7: Odd modes of the electric and magnetic fields perpendicular to the metal-dielectric interface using ϵ_{Au} = -95.92 + i10.97

a periodic metal grating system was investigated in order to achieve a slow light effect.

2.4.1 EM field confinement and slow light effects in a periodic metal grating system

In this subsection, confinement of the SPP and single mode dielectric waveguide modes are analysed, by using a simple silicon-on-insulator waveguide structure with and without the metal gratings. Subsequently, the conditions required to achieve a slow light effect within a structure comprising a periodic metal grating on an SOI waveguide are also investigated.

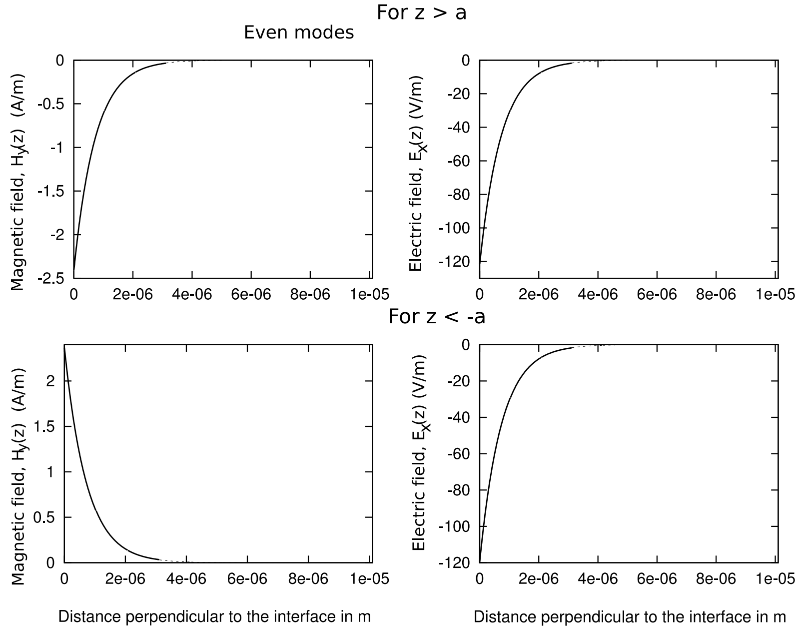

Figure 2.8: Even modes of electric and magnetic fields perpendicular to the metal-dielectric interface of an IMI structure with ϵ_{Au}=-95.92 +i10.97.

Coupling SPP modes with free propagating light is a difficult task since they cannot be directly excited by simply illuminating the metal surface with an incident light source. This is because the wavevector of a surface plasmon mode is always larger than the corresponding value for the EM wave propagating in vacuum [68]. However, since SPP modes are sensitive to surface features, defects can be introduced which aid coupling of SPPs to the incident light, and therefore control the SPP propagation in a guided medium [69]. These defects may be micro-scatterers or arrays of aligned nano-particles arranged in a periodic manner [69]. When SPP modes approach these defects, they are partly scattered, transmitted or reflected, which generally depends on their size, geometrical shape and wavelength [70].

A periodic metal grating structure on a silicon waveguide can be used to excite and guide SPP modes in a dielectric medium. When an incident light shines on such a

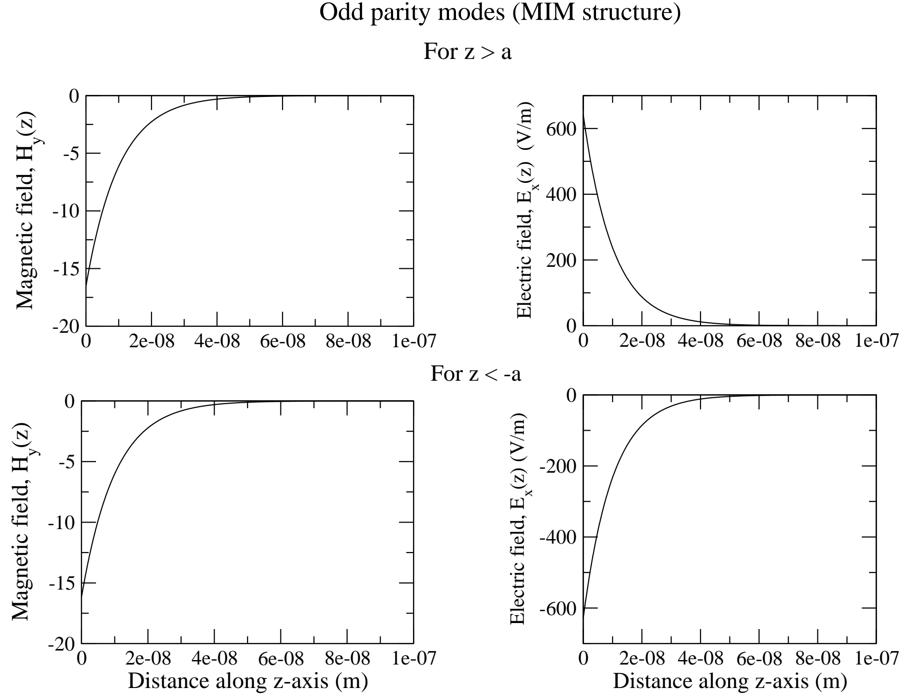

Figure 2.9: Odd modes of electric and magnetic field components perpendicular to the metal-dielectric interface with complex ϵ_{Au}=-95.92 +i10.97.

structure, the scattering of SPPs leads to interference between the scattered components, which gives rise to Bloch waves of SPP modes [71].

A periodically arranged metal grating structure on an SOI waveguide, as shown in Figure 2.10, was illuminated by TM polarised light from the left hand side of the structure. Copper gratings of width a, period d and spacing b were used.

The duty cycle of a periodic grating is defined as the ratio between its width and pitch, a/d [72]. The metal grating structure overcomes the momentum mismatch between the incident wavevector k_{inc} and SPP propagation constant γ_{SPP} by satisfying the following condition [61]:

$$\gamma_{SPP} = k_{inc} sin\theta + \nu g \tag{2.58}$$

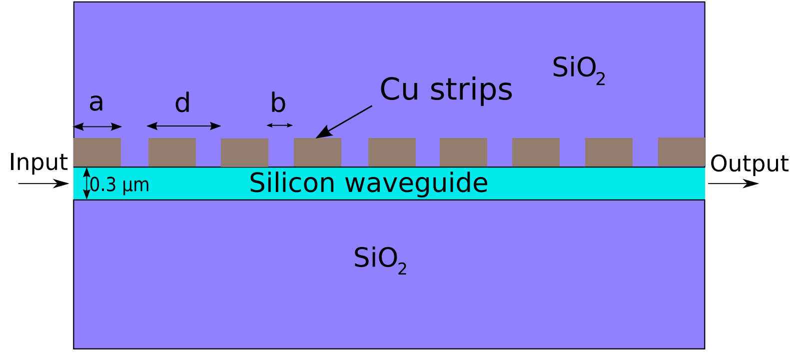

Figure 2.10: A schematic plan view of a metal grating structure with period d on top of a 300nm thick silicon-on-insulator waveguide.

where $g = 2\pi/d$ is the reciprocal vector of the grating, ν is an integer and θ is the angle between the normal of the grating plane and incident light.

A two dimensional (2D) finite element electromagnetic model (FEEM) of the grating structure was developed using Comsol EM software [73], and the system transmission was measured at the output of the waveguide (Figure 2.10). SPP resonance was obtained by tuning the duty cycle of the grating structure, for which a minimum transmission through the waveguide occurs, as indicated by the transmission spectra shown in Figure 2.11. For this purpose, the s-parameter S_{21} was calculated, which is defined as the ratio of the power transmitted at the output to that incident at the input.

Figures 2.12a and 2.12b show the simulated electric field displacement profiles with and without the grating structure on a dielectric waveguide, respectively. In the grating structure, the pinning of the SPP field intensity at the metal-dielectric interface was observed with the maximum intensity located at the interface, which decays exponentially in a direction perpendicular to it (Figure 2.12a). In this case, SPP resonance was obtained for a grating period of d=0.24μm, and a spacing of 0.2μm. Conversely, for the structure without any gratings (Figure 2.12b), the EM field intensity is symmetric with respect to the propagation axis of the dielectric waveguide, and the maximum intensity is located at the centre of the waveguide.

The wavevector k is defined as $k = 2\pi/\lambda$, where λ is the wavelength of the incident

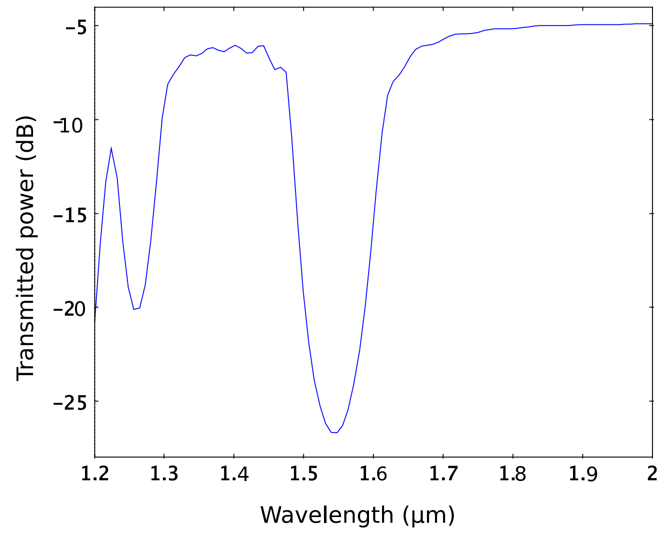

Figure 2.11: Power transmission spectrum of the metal grating structure (Figure 2.10), in which minimum transmission depicts the resonance condition at ≈1.55μm wavelength.

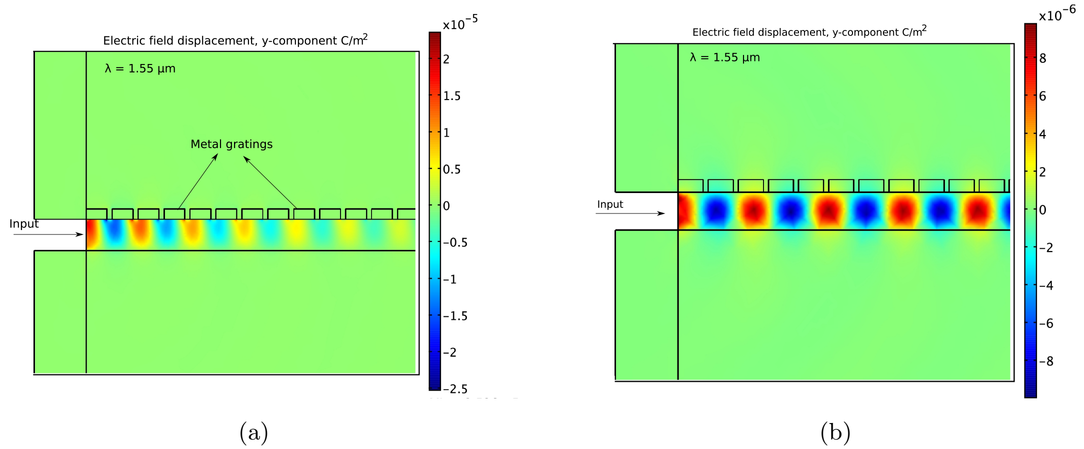

(a)

(b)

Figure 2.12: The electric field displacement (E_y) in (a) a periodic metal grating structure, where the pinning of the SPP modes is observed at the metal-silicon interface, and (b) a single mode dielectric waveguide structure without gratings.

light. The SPP dispersion within the grating structure (Figure 2.10) with materials of different refractive indices was obtained by calculating the SPP propagation constants at different incident frequencies, using the FEEM [73]. Figure 2.13 shows the dispersion curve of the plasmonic grating structure (black circles) along with the light lines of other bulk materials. The group velocity (v_g) is defined as the derivative of the frequency (ω) with respect to k [74]. For larger values of k, a reduction in v_g was observed, leading to slowing of light within the structure [75]. The EM resonance can be tuned by adjusting d or b between the metal strips of the grating structure. The figure indicates that at low wavevectors there is not much spectral dispersion, which is because the period of the gratings is sufficiently smaller than the incident wavelength (Figure 2.13). The applications of the slow light effect in such a grating structure includes, but are not limited to, enhanced optical data storage, on-chip integration of optical circuits, etc. [76].

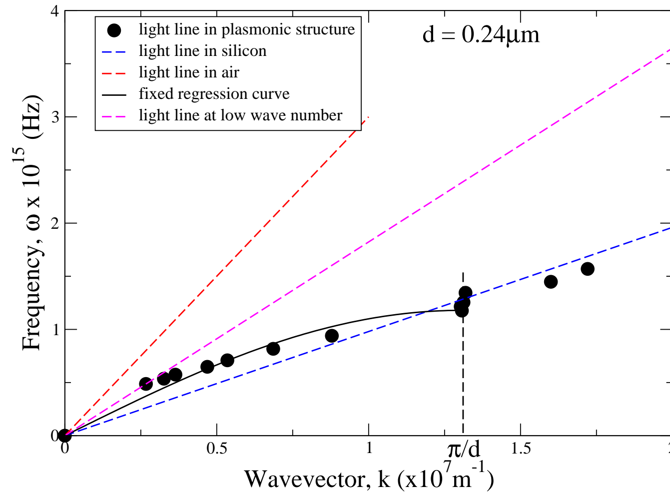

Figure 2.13: Dispersion curves obtained for the grating structure (Figure 2.10) comprising materials with different refractive indices. The black line shows a regression curve fitted to the dispersion data points from the metallised grating structure.

Figure 2.14 shows the dispersion curve in the first Brillouin zone, which is defined as the primitive cell in reciprocal space. It repeats periodically in the reciprocal space, with a period of $2\pi/d$. The second Brillouin zone was obtained by shifting the SPP modes

at higher frequencies by $2\pi/d$ (i.e by subtracting the SPP wavevectors by $2\pi/d$) in the x-axis [68].

The grating structure is analogous to energy bands for electrons in crystals, where the crystal lattice corresponds to periodic arrangement of the atomic potential. These bands are separated by band gaps, in which no electronic states exits [77]. The energy band gap occurs due to the interaction of the conduction electrons with ion cores of the crystals, resulting from the Bragg reflection. When the Bragg condition of $k = \pi/a$ (where a is the lattice constant) is satisfied, the travelling wave to the right is reflected to the left and vice-versa, which leads to the formation of a standing wave. These standing waves represent the accumulation of charge electrons at different regions, forming different energy bands which are separated from each other, forming an energy gap similar to the band gap appearing near the band edge in Figure 2.14 [77]. In the grating structure, Bragg's condition is obtained due to the constructive interference of the electromagnetic waves, which occurs when the path difference between the adjacent grating periods is a half-integer multiple of the incident wavelength λ [77]. For the structure described in Figure 2.10, the band gap occurs at the Brillouin zone edge corresponding to wavevector, $k = \pi/d$ (Figure 2.14).

Qualitative analysis of the field confinement between the silicon waveguide and metal grating in SOI waveguide structures was then carried out for the case of two different metals (Al and Cu). For this purpose, the power confinement factor within a particular region of the waveguide layer in both the plasmonic and non-plasmonic waveguides (as shown in Figure 2.15), were compared using the FEEM.

Arbitrary 10% and 25% portions of the silicon waveguide (shown as the shaded portion in the figure) were chosen, to compare the fractional confinement within these regions with and without the presence of a grating structure on the SOI waveguide. The confinement factor was determined by calculating the ratio between the normalised power confined within the specific region and within the whole silicon slab region. By varying the mark:period ratio (a/d) with the fixed period of 0.24μm, EM simulations were carried out to obtain the confinement factors for the top 10% and 25% portions

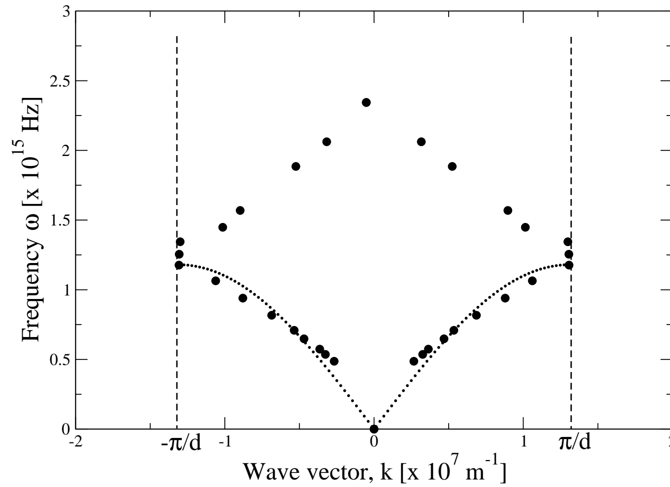

Figure 2.14: SPP dispersion of the periodically modulated structure shown in Figure 2.10, with the metal strip width $a = 0.2\ \mu$m and the grating period $d = 0.24\mu$m. A band gap is observed at the Bragg resonance condition.

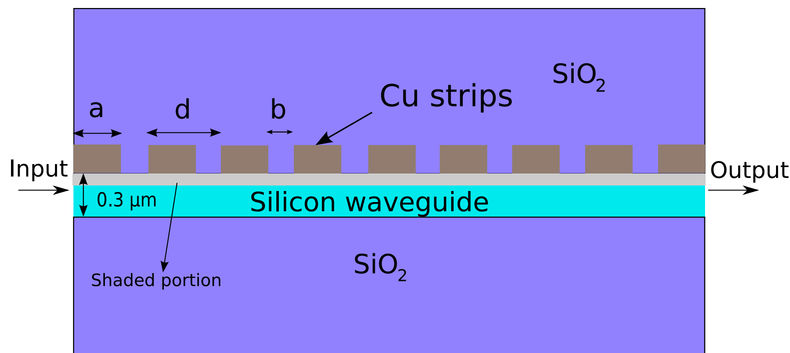

Figure 2.15: The metal grating structure used for the analysis of the SPP power confinement factor, in which the shaded region represents the portion of the dielectric Si waveguide layer where the integrated field intensity was obtained in both plasmonic and non-plasmonic structures.

of the Si waveguide as shown in Figure 2.16. The continuous red and blue curves in the figure correspond to the confinement factor for 10% and 25% portions of the Si waveguide in the non-plasmonic structure, and the circles (red and blue) corresponds to the confinement factor values in the respective regions in the plasmonic grating structure.

The figure indicates that the confinement of the SPP modes in the top 10% portion of the Si-waveguide is larger than that of the dielectric waveguide modes in the respective region by a factor of 6, which occurs at a/d=0.875. It appears that the confinement factor shows little variation with respect to the mark:period ratio or the width of the metal strips. Hence, metal gratings with smaller strip widths can be used to achieve similar confinement factor values, which will reduce the insertion loss due to absorption by the metal. The confinement factor values were also calculated using aluminium, and the results were found to be similar to those obtained using copper.

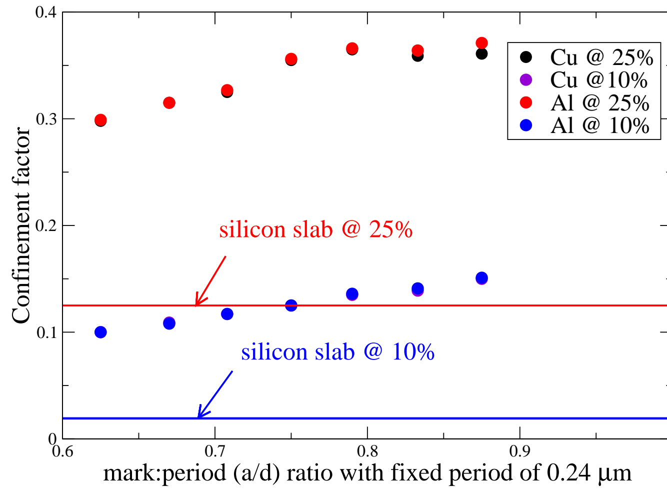

Figure 2.16: Comparison of fractional confinement of power in planar dielectric waveguides and plasmonic grating structures of similar dimensions, using copper and aluminium. The red continuous line and dots denote the confinement factors within the top 25% of the Si region within the planar dielectric waveguide and plasmonic grating structures, respectively. A similar comparison was made using the top 10% of the Si region of the dielectric waveguide as indicated by the blue continuous lines and dots.

,

The decay constant (α) of these SPP modes can be calculated from the power P_1 obtained at a point and power P_2 obtained at a point distant by L down the propagation path, i.e $P_2 = P_1 e^{-\alpha L}$. The propagation length can then be determined by calculating the inverse of α. Figure 2.17 shows the propagation lengths of the plasmon field in the

grating structure (Figure 2.10) for different mark:period ratios. The figure shows that longer propagation lengths can be achieved when the mark-period ratio is reduced, i.e with reduced metal width, while maintaining a large plasmon mode confinement.

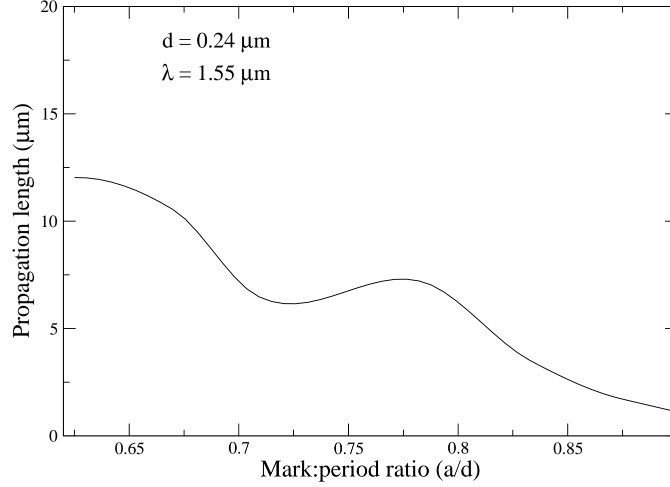

Figure 2.17: Propagation length calculated against the mark:period ($\frac{a}{d}$) ratio at 1.55μm free space wavelength using a copper grating structure

Figure 2.18 shows the effect of changes in wavevector k on the confinement factor for different grating periods, with all other parameters kept fixed. Due to the change in the period of the gratings, the corresponding resonance wavelength was changed, in which π/d=1.309$\times$10^{7}m^{-1} corresponds to the value at the resonant wavelength of 1.55μm. The figure indicates that the confinement factor is not very sensitive (with only <10% variation) to the location of the mode on the dispersion curve.

Figure 2.19 shows the effect of changes in mark:space (a/d) ratio on the SPP resonance wavelength, obtained using the FEEM. The figure indicates that the SPP resonance wavelength of the grating structure varies somewhat for different strip widths. This happens because the change in the mark:space ratio slightly alters the effective plasmon mode index, and therefore changes the SPP resonance wavelength.

Thus, it can be said from the study carried out on the metal grating structure on an SOI waveguide that such a structure could be employed to achieve strong confinement of the EM mode. Additionally, the structure could also be used for slowing light,

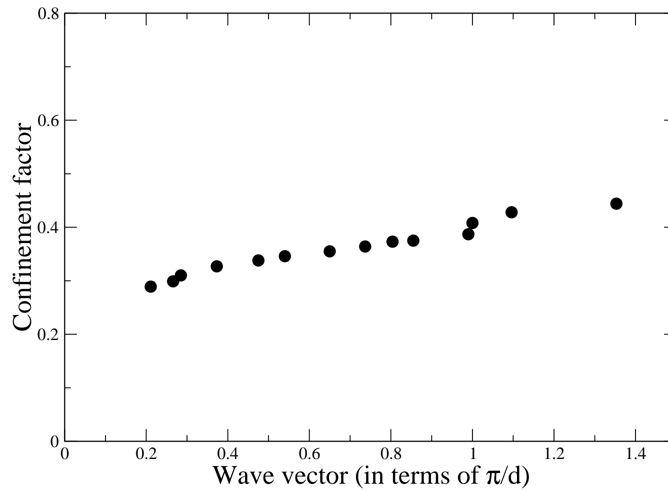

Figure 2.18: Dependence of the confinement factor on wavevector(k)

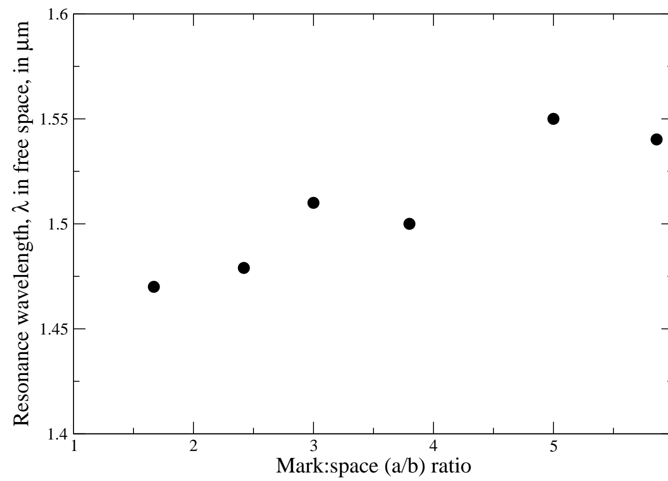

Figure 2.19: Variation in free space resonance wavelength with mark:space ratio for a grating structure with period $d = 0.24$ μm

which can be easily controlled by tuning the period of the gratings. Strong confinement of light in plasmonic structures aids reduction of device length, lower power consumption and therefore faster optical response, which can be used for applications such as modulators [46, 78], waveguides [79, 80] and photodetectors [81].

2.5 Choice of metals

In the context of the silicon photonics industry, the metals should be chosen such that they are CMOS compatible, cheap, and abundantly available. Therefore for most photonic applications, copper and aluminium are the metals which are commonly used for interconnects in CMOS processing. On the other hand, silver is also a good choice of metal due to its smaller damping rate. Table 2.1 show complex refractive indices at 1.55μm wavelength for copper, silver and aluminium which are used as the metals in various plasmonic structures [82], discussed in the following chapters.

Copper	Silver	Aluminium
0.716 + i10.655	0.144 + i11.37	1.578 + i15.658

Table 2.1: Shows the complex refractive indexes of different noble metals at 1.55μm wavelength.

In summary, different metallised configurations including IMI, MIM and grating structures were investigated theoretically. It was observed that the use of an IMI based structure leads to a low propagation loss, but this is achieved at the expense of a poor mode confinement. In contrast, MIM structures show a very strong mode confinement at the metal-dielectric interface, but introduce a larger IL, which is due to strong absorption by the metal.

In the final subsection, the EM mode confinement within a dielectric waveguide structure with and without the presence of the gratings was discussed. It was found that the plasmon modes are much better confined than the dielectric waveguide mode by a factor of almost 6. The grating structure was then explored to achieve slow light effect by tuning the periodicity of the gratings.

Chapter 3

A silicon based plasmonic enhanced stub modulator

3.1 Introduction

The highly confined nature of the surface plasmon modes in sub-wavelength photonic devices can be employed for applications in waveguides, wavelength selective filters, modulators, bends/splitters, and reflectors [83–87]. For example, a metal-dielectric-metal (MDM) waveguide with a stub structure (a branch from the waveguide of a finite length) can function as wavelength selective filter (see Figure 3.1). The transmission through such a structure can be tuned by tailoring the stub height, which corresponds to half the plasmon wavelength in the MDM waveguide, and therefore behaving as an effective filter [84]. The stubs have the advantages of small size, simple structure, and are easy to fabricate. Additionally, a MDM waveguide directly or side-coupled to a cavity filled with an active material was also investigated for use as an absorption switch, where a controlled transmission was obtained by varying the imaginary part of the refractive index of the material filling the cavity via an external bias [83].

However, MDM structures introduce high optical losses due to the use of a large amount of metal [88, 89]. Therefore, the amount of metal used in plasmonic structures

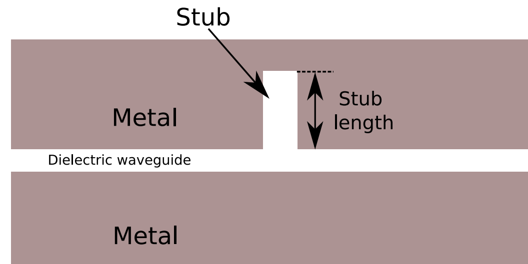

Figure 3.1: Schematic of a stub structure in an MDM waveguide.

should be minimised. Furthermore, the MDM geometry is not compatible for standard complementary-metal-oxide-silicon (CMOS) processing technology to integrate photonic and nano-electronic devices on a common SOI platform.

In this chapter, a sub-micron sized metal coated stub structure coupled to a dielectric waveguide (rather than an MDM geometry) as shown in Figure 3.2 is investigated. The height of the stub was varied to achieve different orders of EM resonance within the stub. These resonances can be damped by altering the imaginary part of the refractive index of the material filling the stub via an externally applied bias, which therefore modifies the transmission at the output of the waveguide.

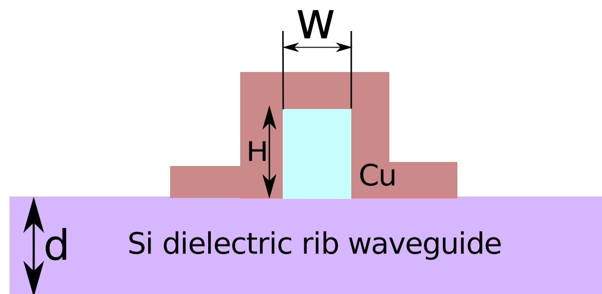

Figure 3.2: Schematic of a metallised stub coupled to an underlying dielectric rib waveguide.

3.2 The finite element and transmission line models of the metallised stub structure

The structure described in Figure 3.2 can be extended by coupling it to a 0.5μm thick underlying single mode SOI rib waveguide as shown in Figure 3.3. The structure was modelled and investigated theoretically using a two dimensional (2D) finite element electromagnetic model (FEEM) [73]. For modelling purposes, the structure was surrounded by perfectly matched layers, which absorb any EM waves radiated out, so that they are not reflected back. These radiated waves from the core waveguide are counted as lost and do not contribute to the transmission at the output. It was assumed that the structure extends infinitely in the third dimension (i.e. along the z-axis). The stub was surrounded by copper with relative permittivity ϵ_r, on both its vertical sides and on the top, for a 1.55μm wavelength operation [90], and SiO_2 was used as a cladding layer. Since SPP modes exist for a transverse magnetic (TM) polarised mode in a metal-dielectric structure [61], the fundamental TM mode of the waveguide was launched towards the structure from the left hand side. The side metal wings (width W_1) of the stub structure aid the efficient coupling of the guided TM mode into an SPP mode as the mode approaches the metallised section of the structure.

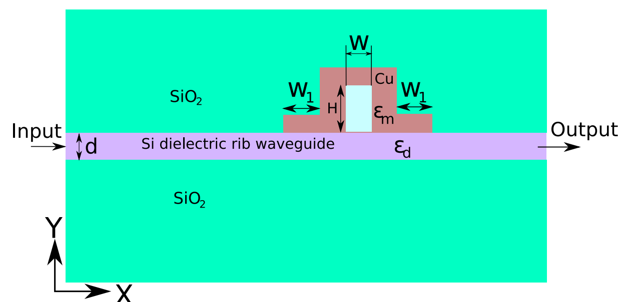

Figure 3.3: Schematic side view of a dielectric rib waveguide coupled to a metallised stub structure on a silicon-on-insulator substrate.

A metallised stub coupled to the silicon (Si) dielectric rib waveguide can be described by transmission line theory, in which a load of impedance Z_L is matched with the feeder

transmission lines of characteristic impedance Z_0 in order to minimise the loss due to the impedance mismatch between them. When such a condition is satisfied, minimum incident power is reflected, which leads to maximum absorption of the incident power by the load and therefore, maximum power transmission to the load. In transmission line circuit theory, this is generally achieved by connecting a short-or-open circuited stub between the feeder transmission lines and the load as shown in Figure 3.4a [83, 91]. According to this theory, the single mode dielectric waveguide in Figure 3.3 is equivalent to feeder transmission lines with a complex propagation constant γ_t, whose characteristic impedance Z_0 is given by [85, 92]:

$$Z_0 = \frac{\gamma_t}{j\omega\epsilon_t} d, \tag{3.1}$$

where ϵ_t and d are the dielectric permittivity and width of the input waveguide, respectively.

The complex propagation constant of the lowest order TM mode in the dielectric waveguide was determined by simulating a single mode silicon-on-insulator waveguide (width d) without the stub using the FEEM. According to the transmission line theory, the stub coupled to the dielectric waveguide is analogous to two parallel transmission line segments of height H, with a propagation constant γ_s and characteristic impedance Z_S. Z_L represents the load impedance connected to the stub, which accounts for the phase shift induced in the SPP wave reflected from the stub end [91]. This can be calculated approximately by equating the reflection coefficient obtained from circuit theory [91, 93] with the complex reflection coefficient amplitude (Γ) of the SPPs at the stub end:

$$\Gamma = \frac{Z_L - Z_S}{Z_L + Z_S} \approx \frac{\sqrt{\epsilon_d} - \sqrt{\epsilon_m}}{\sqrt{\epsilon_d} + \sqrt{\epsilon_m}} \tag{3.2}$$

which leads to

$$Z_L = \sqrt{\frac{\epsilon_d}{\epsilon_m}} Z_S \tag{3.3}$$

where ϵ_m, ϵ_d are the permittivities of the metal and dielectric at $\lambda = 1.55\mu$m. In Eq. 3.3,

since ϵ_m is relatively very large, Z_L tends to zero, which results in a short-circuited stub end. This means that the two parallel transmission line segments which were connected in parallel (Figure 3.4a) can now be connected in series with the feeder transmission lines as shown in Figure 3.4b.

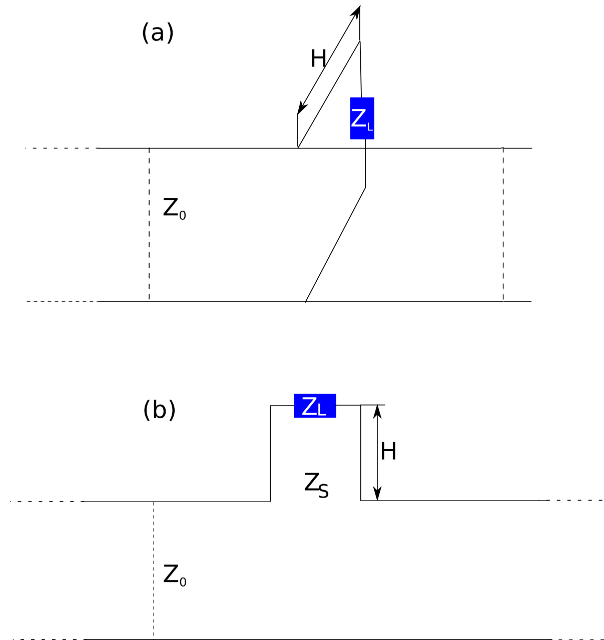

Figure 3.4: (a) Schematic equivalent of the metallised stub structure according to the transmission line theory. (b) Simplified representation of the single stub matching.

Based on a transmission line model (TLM), the transmission T of such a system is given by:

$$T = |1 + \frac{Z_S}{2Z_0}\tanh(\gamma_S H)|^{-2} \tag{3.4}$$

where $\gamma_S = \alpha_S + \mathrm{i}\beta_S$ is the complex propagation constant of the EM wave inside the stub, which was determined by simulating a metal-dielectric-metal waveguide using the FEEM.

It follows from Eq. 3.4 that transmission resonance within the stub can be achieved when $\beta_S H = (N + 1/2)\pi$ is satisfied, where H is the stub height and N is an integer.

Since both Z_S and α_S depend on the imaginary part of the refractive index (κ) of the material filling the stub, the transmission at resonance can be tailored by modifying κ (and therefore the absorption coefficient α) via an external electrical bias [83]. Thus, by spoiling the EM resonance within the stub, a variable transmission at the output waveguide can be obtained which can be optimised to achieve a maximum system performance.

3.3 Two dimensional finite element modelling of the metallised stub structure

In accordance with the transmission line theory discussed in the previous section, resonance within the stub can be achieved by tuning the width (W_s) and height (H) of the stub, and length of the side metal wings (W_1). In order to achieve a variable transmission with and without an applied bias, the stub should be filled with a material such that it exhibits an acceptable amount of change in its absorption coefficient, and therefore κ. This is possible if the stub cavity is filled with an optically active material, such as Ge-rich SiGe multiple quantum wells (MQWs) or layers of Ge quantum dots (QDs) grown on a silicon matrix [94–97]. An electrical bias applied to such a structure shifts the absorption edge (and therefore κ) in Ge quantum wells as shown in Figure 3.5, resulting in a transmission contrast between the biased and unbiased states. Thus, the metallised stub in Figure 3.3 was assumed to be filled with a material with refractive index n= 4+iκ, where the real part is the bulk Ge refractive index.

For κ=0, the resonance inside the stub is strongest and the incoming field is mostly absorbed by the stub (by the metal, not semiconductor), which results in a transmission minimum at the output of the Si waveguide. The quality factor of the stub (Q_S) is given by:

$$Q_S = \frac{\omega_0}{2\alpha_S v_g} \tag{3.5}$$

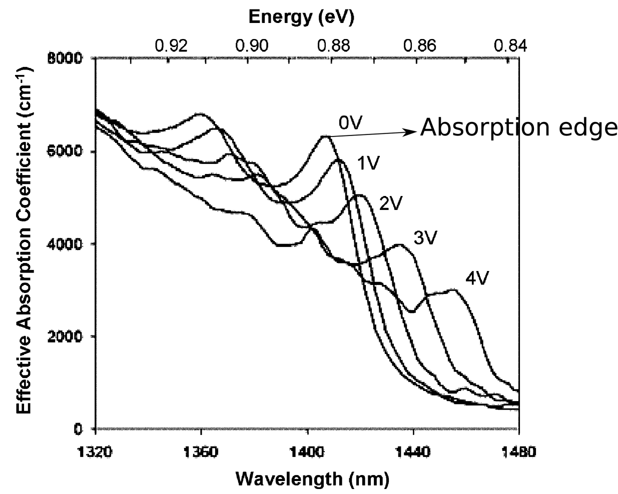

Figure 3.5: Change in absorption coefficient spectra at 300K of a heterostructure comprising 10nm Ge quantum wells and 16nm Ge/$Si_{0.15}Ge_{0.85}$barriers on a relaxed $Si_{0.1}/Ge_{0.9}$ buffer [94].

where ω_0 is resonance frequency and $v_g = \frac{\partial\omega}{\partial\beta_S}$. On increasing κ to an arbitrary value of 0.1, the quality factor of the stub degrades, and the EM resonance within the stub is damped, which leads to increased transmission through the Si waveguide as shown in Figure 3.6.

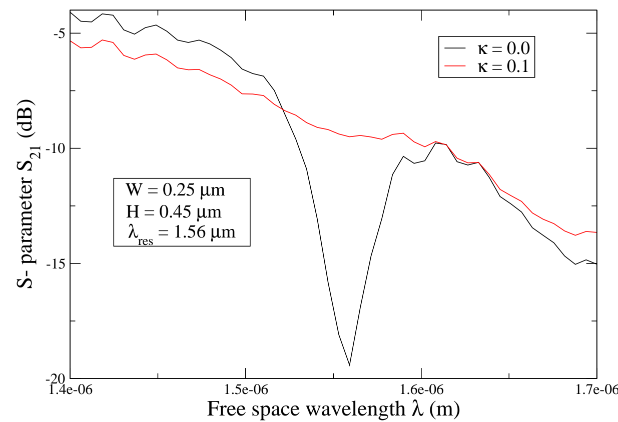

Figure 3.6: Effect of a change in the imaginary part of the refractive index of the material filling the cavity, on the transmission spectrum of the system

3.4 Comparison of the finite element and transmission line results

Simulations were carried out for different H using the 2D FEEM while keeping all other parameters fixed. The complex propagation constants γ_s and γ_t extracted from the FEEM were used in the TLM to calculate the transmission of the system using equation (3.4) under an absorbing (κ=0) stub condition and a non-absorbing (κ=0.1) stub condition. The extinction ratio (ER) is defined as the ratio of the transmission between the two stub conditions. Figure 3.7 shows ER in the metallised stub structure coupled to a dielectric waveguide as a function of H, calculated using both the TLM and FEEM. The figure shows good agreement between the TLM and FEEM results. The peaks correspond to different vertical orders of EM resonances within the stub (Figure 3.8), and show the maximum ER attainable due to damping of the stub resonance when switching between κ= 0.0 and κ= 0.1. At resonant heights, the stub behaves as a closed cavity within which standing-wave structures with integer multiples of half wavelength (in our case half the surface plasmon wavelength is 0.224μm) are formed, with increased electric field intensity. A maximum ER of approximately 8dB was attained for H=0.45μm and W=0.25μm. At non-resonant heights, the presence of the stub merely adds to the total loss incurred by the propagating SPP wave, which results in a lower transmission in the absorbing stub condition than that in the non-absorbing condition. This, in turn, results in a negative ER (if expressed in dB units) for non-resonant stub heights.

Figure 3.8 shows the electric field profiles (E_y) for different orders of vertical cavity resonant modes (at κ=0) within the stub for a fixed W= 0.25μm and different resonant heights (Figure 3.7). It can be seen from the figure that, when a dielectric waveguide mode approaches the metallised section of the structure, the field loses its symmetry; the maximum of the field intensity is shifted from the centre of the waveguide and becomes pinned at the metal-dielectric interface of the side metal wings. A careful observation of the field profile near the top of the stub shows that an incomplete vertical SPP mode is formed due to pinning of the SPP mode at the metal-dielectric interface.

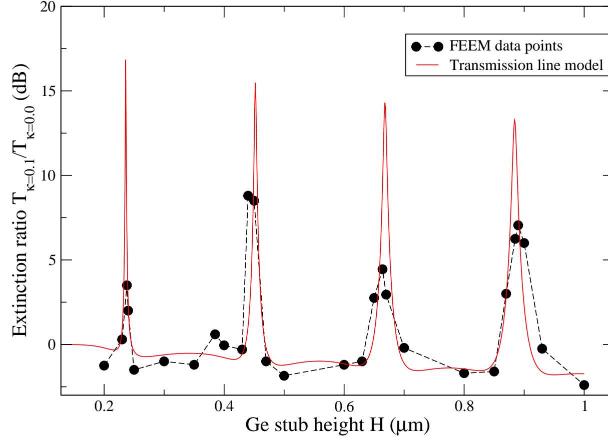

Figure 3.7: Extinction ratio $T(\kappa = 0.1)/T(\kappa = 0.0)$ calculated using the FEEM (black dots) and TLM (continuous curve) of a 0.25μm wide metallised stub coupled to a dielectric waveguide (Figure 3.3) at λ=1.55 μm.

Additionally, it was found that these resonant EM modes do not match exactly the metallurgical stub height. Instead, the first vertical EM mode formed at the bottom of the stub decays downward towards the stub-waveguide interface, because there is no hard boundary located at the interface. Therefore, in order to fit the analytical TLM result to the FEEM result, a correction length of $\triangle H$= 0.128μm must be subtracted from the geometrical height of the stub (Figure 3.8).

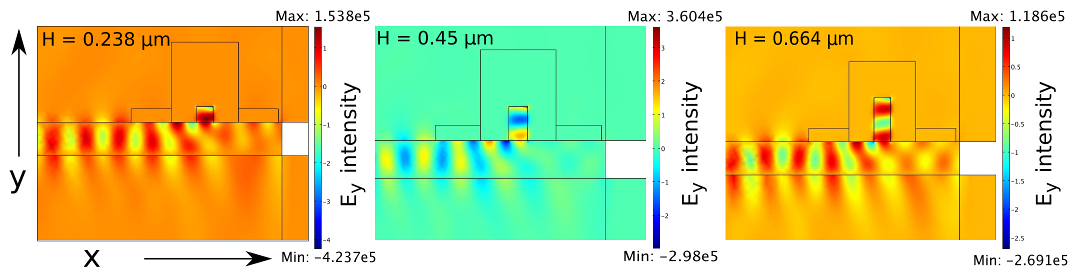

Figure 3.8: The y-component of the electric field for the 1st, 2nd and 3rd orders of vertical resonant cavity modes within the stub for different H.

3.5 Lateral stub resonance modes

In the previous section, W was kept fixed at 0.25μm since this value corresponds to approximately half the surface plasmon wavelength in silicon (which is also almost half the incident wavelength in silicon: $1.55/(3.43 \times 2) = 0.226\mu$m), which supported the 1st order lateral EM resonant mode. This means that higher orders of lateral EM resonant modes can be obtained within the stub for larger widths. Therefore, in order to analyse the effect of wider stub widths and heights on the extinction ratio and insertion loss of the metallised stub structure, EM simulations were carried out to investigate the transmission dependence on κ for different W and H as shown in Figure 3.9. Narrow stubs ($W < 0.4\mu$m) supported only the first order lateral resonance as explained before, compared to higher order lateral resonant modes for wider stubs. W=0.25μm and H=0.45μm corresponds to the stub which supports only a first order lateral resonance (circle) and its transmission dependence on κ has already been described in the previous section, i.e. the transmission increases with increasing κ due to the deterioration of the stub resonance. For narrower stubs, at non resonant heights (star and diamond curves), the transmission decreases slightly since the system becomes lossy with increasing κ, and tends to the same value at large κ. This means that for narrower stubs, the material loss dominates and the system becomes insensitive on κ for larger values of κ. However, this is not the case for wider stubs ($W > 0.4\mu$m), where a different behaviour was observed due to the formation of the 2nd order lateral resonance mode, which is mostly responsible for the transmission behaviour (square and triangle curves). Figure 3.10 shows the electric field intensity (E_y) of the 2nd order lateral resonant mode at W=0.45μm and H=0.6μm. Similar to the 1st order lateral resonance mode, the SPP antinodes formed at the top of the stub are incomplete due to pinning of the modes at the metal-dielectric interface, and a portion of the EM mode near the bottom of the stub spills into the adjacent dielectric waveguide region. The system transmission in the FEEM is defined by the power of the EM mode which can be coupled into the single mode output waveguide at the exit port (Figure 3.3). The transmission first decreases with increasing κ, leading

to a sharp minimum (which occurs at κ=0.06 for the 0.5μm wide stub, and κ=0.09 for the 0.45μm wide stub as shown in Figure 3.9). However, the transmission recovers with further increase of κ. For larger values of κ, the transmission is limited by the system loss as indicated by its convergence for different stubs (see square, triangle and brown curves).

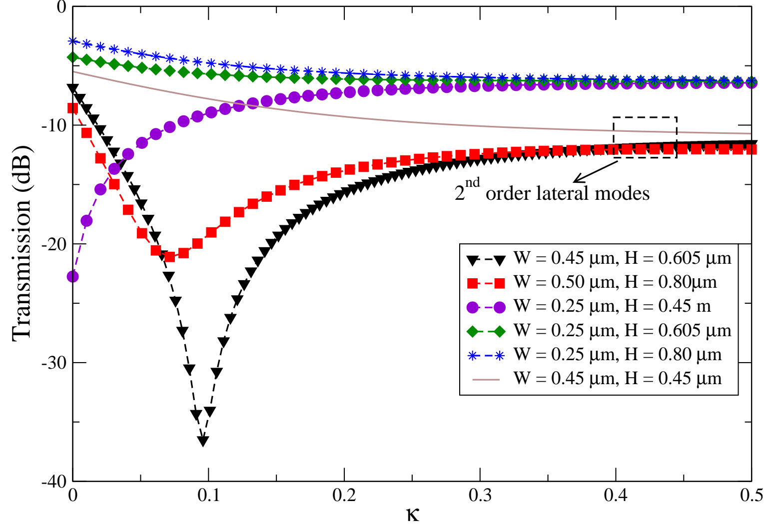

Figure 3.9: Effect of varying κ on the transmission performance of the system for different W and H. W= 0.25μm corresponds to the first order and W > 0.40μm corresponds to the higher order lateral regime.

To investigate the unusual transmission dependence on κ for wider stubs, the magnetic field profile of the EM mode in the waveguide section after the stub was examined for κ ≈0.09, as shown in Figure 3.11, which corresponds to the transmission minimum in Figure 3.9 (triangle curve). Moreover, the output magnetic field profiles across a line in the dielectric waveguide just after the stub were obtained for three values of κ as shown in Figure 3.12. For κ= 0.095, which corresponds to the transmission minimum in Figure 3.9, the symmetric field profile of the incoming EM mode approaching the stub is transformed into an asymmetric field profile of the outgoing EM mode (Figure 3.11), as indicated by almost equal positive and negative magnetic flux density. This leads to a small EM overlap with the field of the single mode output waveguide (which is simply

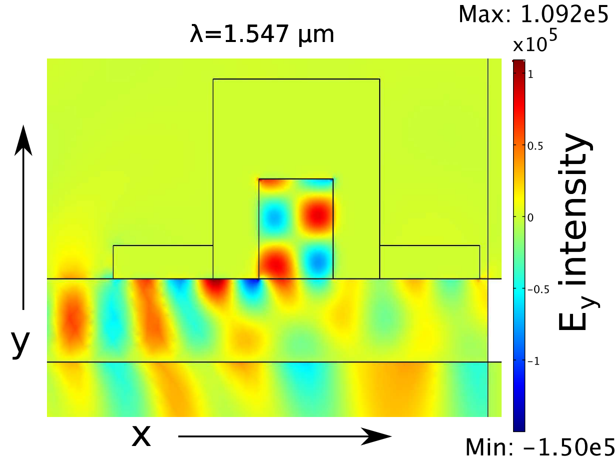

Figure 3.10: The y-component of the electric field intensity showing the 2nd order lateral mode resonance within the stub obtained using the FEEM.

a continuation of the SOI waveguide), and is therefore weakly coupled to it, resulting in minimum transmission at the output. Assuming that the waveguide has no higher bound modes, this output EM field couples to the unbound modes and will be radiated out. For smaller or larger values of κ (for example at κ=0.01 and 0.2), the output EM field is only partially asymmetric, which leads to improved coupling to the output waveguide mode, which explains the transmission dependence on κ in Figure 3.9 (square and black triangle curves). Most of the power modulation for wider stubs was thus provided by the mode conversion phenomenon by the stub itself, rather than the variable reflection phenomenon which is responsible in waveguide-coupled resonator structures [98]. This was also verified by determining the reflected power across a line placed before the stub, which was found to be relatively small (≈0.7dB).

The field profile after the stub depends on the exact stub dimensions, and in some designs may, for a particular value of κ, be almost completely orthogonal to the output waveguide mode. In Figure 3.9, for W=0.45μm and H= 0.605μm, negligible transmission (-37.5dB) can be attained at κ ≈0.1. However, in practice, the precision with which κ can be tuned is limited, which restricts the maximum attainable extinction ratio in such a structure.

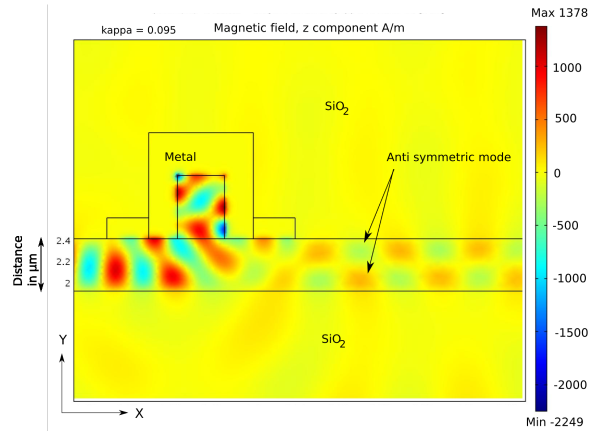

Figure 3.11: The z-component of the asymmetric magnetic field profile obtained within the output waveguide just after the stub with W=0.45μm, H=0.605μm.

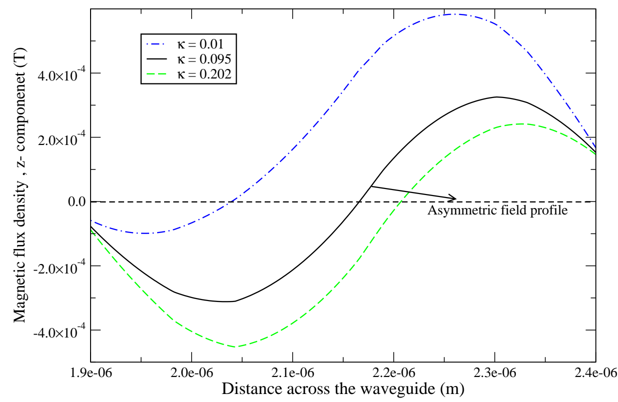

Figure 3.12: 1D magnetic field profile across the waveguide obtained at resonance for the stub with W=0.45μm and H=0.6μm, just after the stub metal flaps for different values of k.

3.5.1 Optimisation

Optimisation of the system performance was carried out with respect to different H and W to achieve maximum ER and minimum IL using the 2D FEEM. A single mode dielectric waveguide of dimensions similar to the stub structure described in the section 3.2 (Figure 3.3) was simulated in the absence of the metallised stub to account for the waveguide loss. This was subtracted from the total insertion loss achieved in the presence of

the stub in order to obtain the loss due to the metallised stub structure. EM simulations were carried out by progressively increasing W, and the stub height was varied to achieve maximum extinction ratio. The practically attainable range of κ is 0.01-0.05 (for an applied bias of 0-1.5V), which has been experimentally demonstrated for electrical modulation of κ using true quantum confined Stark effect (QCSE) in Ge/SiGe multiple quantum wells (although at a shorter wavelength of 1460nm) [94, 99]. Hence κ=0.01 was used in the previous section as a lower value of the absorption coefficient of the stub filling in the unbiased state.

Figure 3.13 shows the dependence of the maximum attainable ER on stub widths for the given range of κ. The extinction ratio increases with stub width up to 0.35μm, but at the expense of increasing insertion loss. For $W \geq 0.4\mu$m, the stub supports 2nd and higher order lateral resonant modes, which show a complex behaviour with increasing W. A very large ER of 23dB and an IL of $\approx$12.2dB was predicted for stub dimensions of W=0.5μm and H= 0.8μm. In another geometry, an ER and IL of 7.8dB each can be attained for W= 0.45μm and H=0.6μm (point a). A good modulator should have a large ER and as small an IL as possible. Hence, if we consider the maximum acceptable IL to be 10dB, then the point a in the figure may be considered as the best choice for the stub design, in order to achieve an optimum system performance within a practically attainable range of κ.

3.6 Biasing schemes for the electrical control of the plasmonic stub modulator

An appropriate electrical biasing scheme of the active material filling the stub was required for the practical consideration of the whole system. Therefore the FEEM was used in an electrostatic mode in order to obtain equipotential lines across the stub for different possible cases as discussed below. This may be achieved in two possible configurations. First, an insulation gap in the metal layer at the top of the stub can be used to allow lateral biasing of an array of Ge quantum dots (QDs), in order to induce the QCSE.

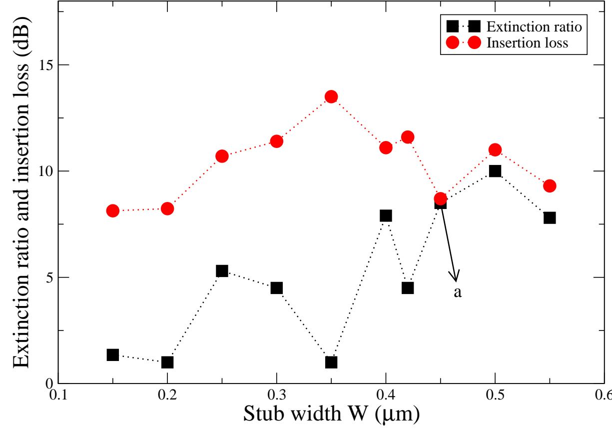

Figure 3.13: Simulated extinction ratio and insertion loss for varying H and W, which correspond to different orders of lateral and vertical resonances within the stub when switching from κ=0.01 to 0.05.

Figure 3.14 shows the lateral biasing scheme across the the stub with an insulating gap region between the two metal portions at the top of the stub. The gap is filled with an oxide material, such as SiO_2. The figure shows a uniform distribution of the equipotential lines in the lateral direction in most of the volume of the stub, which facilitates homogeneous QCSE modulation and prevents any localised electrical breakdown of the Ge QD material within the stub. However, the presence of the gap layer affects the EM mode confinement within the stub due to the leakage of the mode from the stub into the low index oxide region at the top, which aids to the total loss of the system. The gap layer between the two metal portions appears to support its own plasmon modes, which were pinned at the two vertical metal-dielectric interfaces. Additionally, the presence of the oxide layer changes the optical operating regime of the stub. For W=0.48μm and H= 0.61μm, the ER decreases to 7dB with an increased IL of ≈12dB. If the range of κ is increased to 0.001-0.05, which has been previously demonstrated in III-V QDs [100], then an ER of 9.8dB and IL of 9.5dB can be attained.

Secondly, a vertical biasing scheme can be employed, in which the underlying silicon is doped to serve as a contact and thin oxide barriers (for example SiO_2) are grown between the metal and silicon region, as shown in Figure 3.15. Ge/SiGe MQWs could

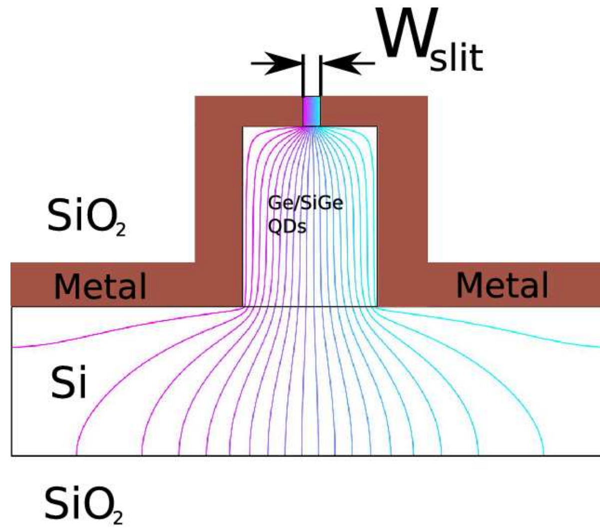

Figure 3.14: Electrostatic equipotential lines in the metallised stub structure with a 60nm wide SiO_2 gap region at the top of the stub, which enables lateral electrical biasing.

then be used as the electro-absorption material provided that the oxide barriers on the sides are also extended between the metal and Si region, which would prevent short-circuiting across the doped Si region. Ge QDs may also be used as an active material to achieve electrical modulation of κ. The oxide thickness (t_{ox}) along the vertical sides and between the metal and the Si region was varied from 10nm to 50nm while keeping all other parameters fixed, and the system performance was investigated using the 2D FEEM.

For example, if the underlying Si region is doped and a bias is applied to the metal, then a maximum electric field is obtained near the top of the stub, which decreases uniformly in the vertical direction towards the underlying Si layer. A uniform electric field distribution within the stub is important in order to achieve a stronger QCSE throughout the active material filling the stub for a given value of applied bias. Figure 3.15 shows the equipotential lines across the stub, with 25nm oxide barriers around the stub, obtained using the 2D electrostatic field simulations. It was found that the static electric field in the vertical direction varies by a factor of 2 within the stub, which may still be acceptable for digital modulation. A more uniform static electric field can be obtained by increasing

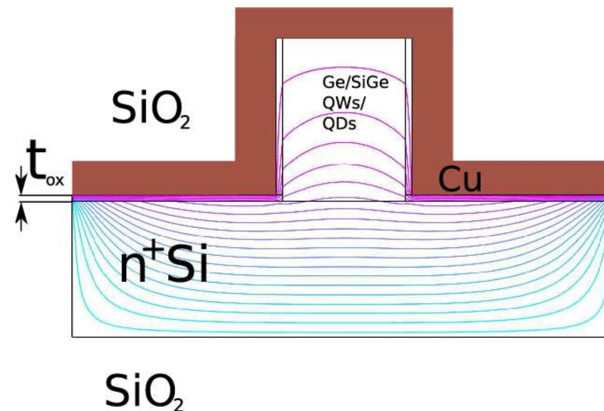

Figure 3.15: Electrostatic equipotential lines in the metallised stub structure with a thin oxide liner along the vertical sides and between the metal and Si region, which enables vertical biasing.

t_{ox}, but the device performance deteriorates. Figure 3.16 shows the electric field component E_y of the simulated electromagnetic mode in the stub structure with oxide liners. No strong stub resonance was obtained in the non-absorbing condition (κ=0.01), which resulted in a poor system performance with a large insertion loss. The EM mode was mostly confined within the thin oxide layers due to the large refractive index contrast between SiO_2 and Ge, and SiO_2 and Si. The highly confined plasmon mode within the oxide layer is similar to a subwavelength gap plasmon mode, which exists in a low index oxide region sandwiched between a conductor and high-index dielectric layer [101, 102].

Although the insertion loss improves with decreasing t_{ox}, the ER shows very poor performance. Moreover, SiO_2 may not be a very good choice for the oxide material, since the use of a 5nm SiO_2 barrier resulted in an ER of 7.3dB and a large IL of 13.8dB for W=0.45μm and H=0.65μm. Alternatively, oxides with large dielectric constants (such as HfO_2) were considered, since they have been extensively studied for a range of CMOS applications [103]. The influence of the dielectric constant of the oxide barrier (ϵ_{ox}) surrounding the stub on the system performance was investigated and the results are shown in Figure 3.17. It can be seen from the figure that for t_{ox}=5nm with ϵ_{ox}=6.25, an ER of 6.6dB and an IL if 7.7dB can be attained for a practically achievable range of

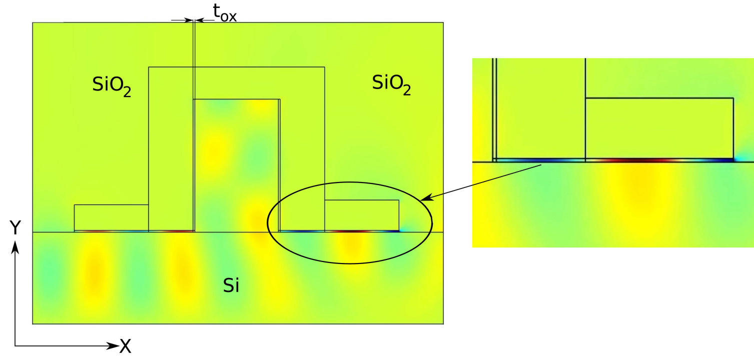

Figure 3.16: Simulated electric field profile (E_y) in the modified stub structure with (W=0.45μm and H=0.725μm) surrounded by SiO_2 barriers along the vertical sides and between the metal and dielectric waveguide.

κ from 0.01-0.05.

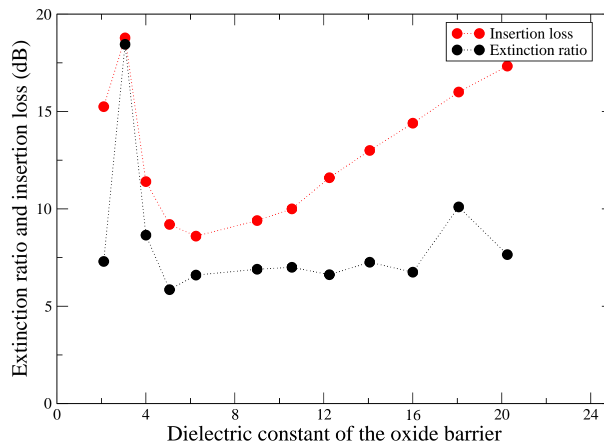

Figure 3.17: Variation of ER and IL with the dielectric constant in a metallised stub surrounded by a 5nm oxide liner (Figure 3.15) with W=0.45μm and H= 0.65μm.

By keeping ϵ_{ox}= 6.25, further EM simulations were carried out by progressively increasing the oxide (ϵ_{ox}=6.25) thickness up to 45nm, and the ER and IL were obtained using the FEEM, as shown in Figure 3.18. It can be seen from the figure that both the ER and IL decrease for t_{ox} > 15nm. Although a large ER of approximately 13dB was predicted for t_{ox}=15nm, the predicted IL is also very large. It was observed that the

confinement of the EM mode within the oxide layer increased with increasing t_{ox}, which resulted in a reduced influence of the change in κ of the stub filling on the resonant mode, and therefore a reduced mode conversion effect, resulting in a smaller ER. The effect of an oxide barrier between the metal and dielectric layer is further investigated in the next chapter. However, an optimum t_{ox} of 5nm was identified for which a minimum IL with an acceptable ER were predicted.

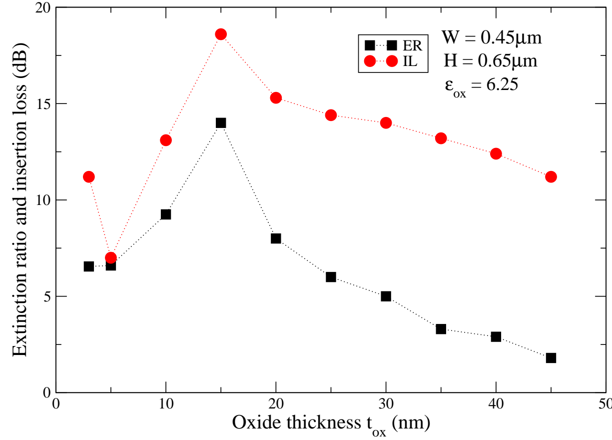

Figure 3.18: Dependence of t_{ox} with ϵ_{ox}=6.25 on the ER and IL of the metallised stub surrounded by oxide layers (Figure 3.15) for W=0.45μm and H= 0.65μm.

In summary, the metallised stub coupled to a dielectric waveguide shows promising results with respect to its predicted extinction ratio and insertion loss for a range of values of W and H. For narrower stubs (W <0.45μm), spoiling of the Q factor of the stub by increasing the absorption coefficient of the stub filling is mostly responsible for obtaining the transmission contrast for κ=0.0 to 0.1. However, it was found that for W > 0.45μm, the EM mode conversion effect introduced by the stub to the incoming EM mode is mostly responsible for achieving large ER for a practically attainable range of κ values. Such a metallised stub structure can be realised by growing thin oxide liners on the sides and between the metal and dielectric waveguide, in order to facilitate lateral electric biasing to induce the QCSE when changing the κ of the stub filling material from 0.01 to 0.05.

Chapter 4

Three dimensional modelling of a plasmonic-enhanced stub modulator

4.1 Introduction

In the previous chapter, transverse magnetic (TM) polarised light was used as the input into the metallised stub structure coupled to a single mode dielectric waveguide [104]. The electric field E_y component of the incident mode was normal to the metal wings (Figure 4.1), which aids excitation and coupling of the SPP modes into the stub. However, absorption of the incident light increases with increasing W and H, due to the increasing path over the metal used, which adds to the insertion loss of the system.

In this chapter, the possibility of using TE polarisation of the incident light as the input mode, launched towards the stub structure, has been investigated using the FEEM. The use of a TE mode requires only one component of the electric field (E_z), which exists in the direction normal to the propagation direction (i.e in the xy-plane of the Figure 4.1). Additionally, the excitation of SPPs requires the electric field component (E_z) of the incident light to be normal to the metal surface. Therefore, in order to excite

SPPs, the original stub structure was modified so that the metal is situated at the front and back relative to the propagation axis as shown in Figure 4.2. In such a case, the E_z component of the TE input mode is not perpendicular to any metal, until it couples into the stub, thus exciting SPP modes within the stub. Hence the side metal wings present in the original stub structure (Figure 4.1) are not required anymore, which leads to a significant reduction of the amount of metal, and therefore reduced absorption of light by the metals.

For simulation purposes, three dimensional (3D) finite element electromagnetic modelling of the modified stub structure was required [73]. The TE mode was launched at the input assuming a sinusoidal variation with respect to the perpendicular (y) axis. The widths of the metallised stub and underlying silicon waveguide (along the z-axis) were kept the same for easy fabrication. Hereafter, the modified stub structure will be defined as the TE stub device.

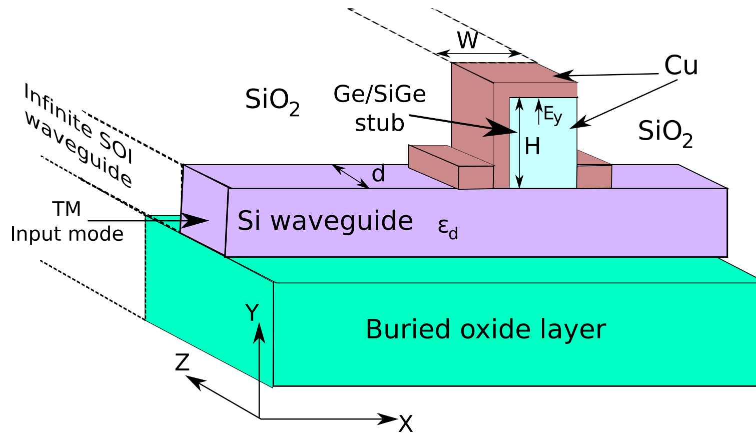

Figure 4.1: Schematic side view of the dielectric rib waveguide side coupled to a metallised stub structure on a buried oxide layer (BOX), which extends infinitely in the third dimension (shown as dotted lines).

As discussed in the previous chapter, the stub was assumed to be filled with an active material (for example Ge/SiGe multiple quantum wells or Ge quantum dots in a Si matrix) whose absorption coefficient, and therefore imaginary part of the refractive index κ, can be varied within the practically attainable values of κ ranging from 0.01 to

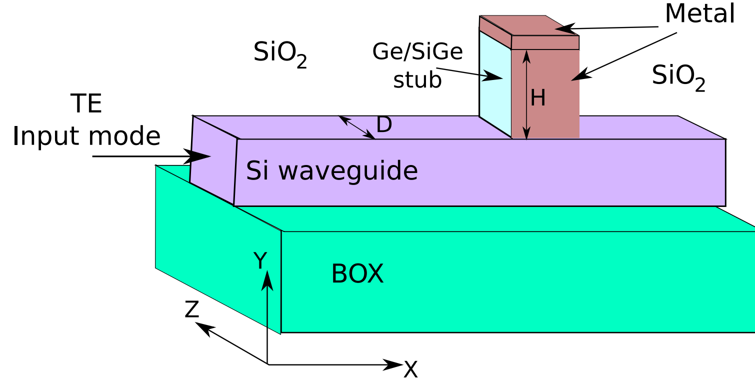

Figure 4.2: Schematic side view of the modified stub structure using TE polarised input mode, in which metal layers are situated at the front and back ends (not visible in this diagram) with respect to the propagation axis, and at the top of the stub.

0.05 by an externally applied field [94, 95, 105]. Figure 4.3 shows the simulated electric field profile (E_z) along the yz-plane through the middle of the stub (Figure 4.2), obtained using the 3D FEEM. The figure shows the pinning of the SPP modes at the sidewalls of the stub with the maximum electric field intensity located at the metal-stub interface, which then decays into the stub region.

EM simulations of the TE mode device were carried out by varying both W and H, in order to achieve different orders of vertical and lateral EM resonances within the stub. At resonance, the imaginary part of the refractive index of the material filling the stub was varied from non-absorbing (κ=0.01) to absorbing (κ=0.05), in order to achieve variable system transmission at the output of the waveguide. The ER was then determined by calculating the difference in the transmission when switching between the two stub conditions, whilst the IL was obtained as the loss incurred by the system in the transmitting state. Figure 4.4 shows the maximum attainable ER (diamond curve) and the corresponding IL (square curve) for different W and H at 1.55 μm wavelength. For $W < 0.55\mu$m, almost negligible ER (< 0.5dB) was obtained. The figure shows that ER slightly improves on increasing W up to 0.88μm, but at the expense of large IL (>8dB).

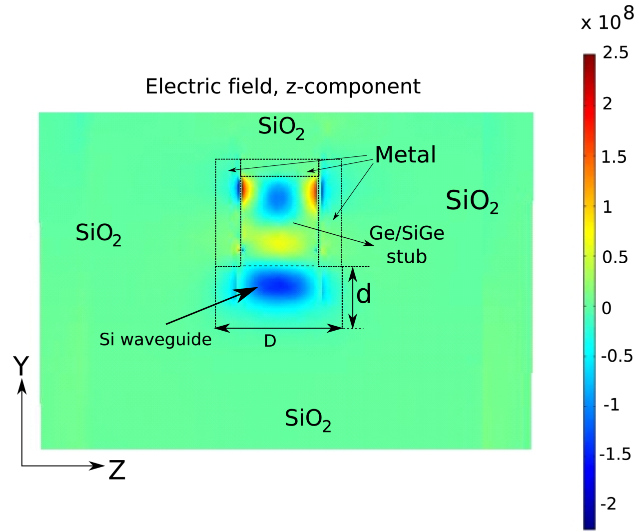

Figure 4.3: Electric field profile (E_y) in the plane yz of the stub structure shown in Figure 4.1.

However, the overall system performance degrades for the TE mode compared to TM mode device, which was observed even for wider stubs (W >0.9μm) as IL remained much larger than the ER.

Figures 4.5a and 4.5b show the electric field profiles (E_y) at particular values of W=0.92μm and H=0.605μm when changing κ of the stub filling. It was established from the study carried out in the previous chapter, on the TM mode device, that most of the power modulation was obtained due to the ability of the stub to transform the symmetric field profile of the input mode into an asymmetric profile of the mode in the waveguide after the stub. This leads to minimum coupling of this mode with the single mode output waveguide, resulting in minimum transmission of the system. However, the EM mode conversion effect was not observed in the TE mode device, which was why very small extinction ratios were predicted in the device when switching between absorbing and non-absorbing stub conditions. This is evident from the field plots: even

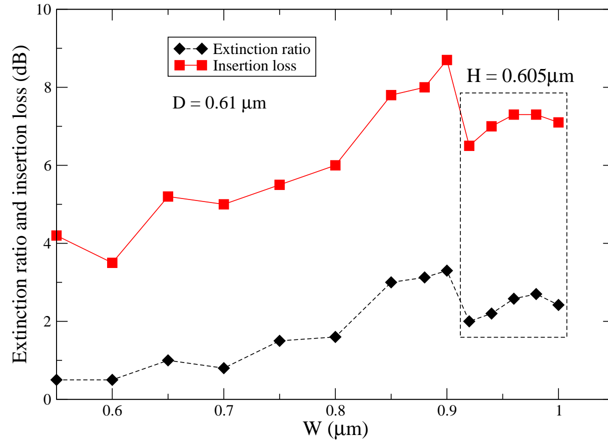

Figure 4.4: Simulated ER and IL obtained for a TE mode device for practically attainable range of κ values, using the 3D FEEM.

though a 4th order lateral resonant mode was obtained within the stub, the field profile of the mode in the waveguide just after the stub appears to be only slightly affected when changing κ from 0.05 to 0.01. This leads to a smaller change in overlap of this mode with the output waveguide mode, and therefore results in negligible ER. For the TE mode device, a simulated maximum ER of only 3dB was predicted, with an IL as large as 8.5dB for W and H at 0.9μm and 0.605μm respectively (Figure 4.4). Hence, it can be concluded that the TE mode device is not the best option for achieving optical modulation.

4.2 Three dimensional modelling of the original metallised stub structure

In the previous chapter, the two dimensional modelling of the stub structure coupled to an underlying dielectric waveguide assumed that both the metallised stub and dielectric waveguide extend infinitely in the third dimension (i.e along the z-axis shown in Figure 4.1), which may not be an accurate approximation for practical devices. The TM input mode used in the 2D FEEM of the metallised stub structure was assumed to be

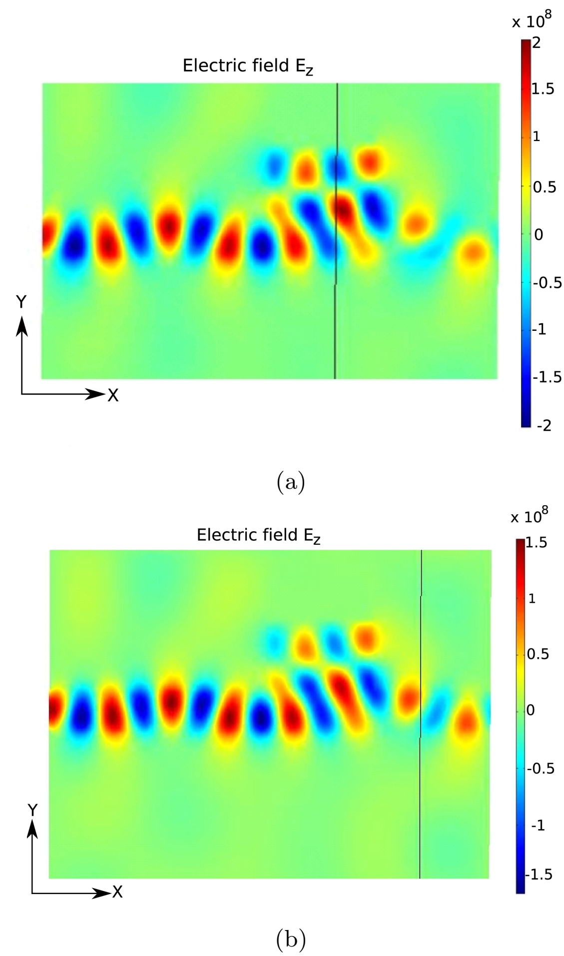

Figure 4.5: The simulated electric field (E_y) profiles along the xy-plane of the TE mode device (Figure 4.1) at: (a) κ=0.01 and (b) κ=0.05, which indicates poor EM mode conversion phenomenon at the output waveguide after the stub.

invariant along the third dimension. Additionally, the condition of launching the TM input mode was approximated by having a sinusoidal approximation for the incident mode within the dielectric waveguide (Figure 4.6a). However in practical waveguide structures, the fundamental mode would penetrate into the surrounding oxide cladding region (Figure 4.6b). Thus in practice, the surrounding oxide cladding should be incorporated in launching the input mode towards the stub structure. Therefore, a complete three dimensional FEEM of the metallised stub structure coupled to a dielectric waveg-

uide was carried out, in which the fundamental mode supported by the silicon waveguide, including its oxide cladding was used for launching. As discussed in the 2D stub model, perfectly matched layers (PML) surrounding the complete structure were used to absorb the EM waves which were not confined, but were radiated out of the silicon core waveguide, without producing any reflections. These radiated waves from the silicon waveguides to the surrounding media are counted as lost and do not contribute to the output.

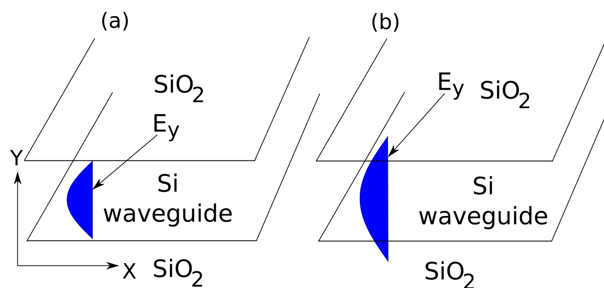

Figure 4.6: The approximated sinusoidal variation of E_y component of the incident TM launched at the input port (a) in the 2D stub FEEM and (b) in actual practice.

A schematic diagram of the 3D metallised stub structure coupled to dielectric waveguide on a buried oxide layer is shown in Figure 4.7. The thickness of the stub in the third dimension was kept the same as the width D of the dielectric waveguide, as this would make for easier fabrication.

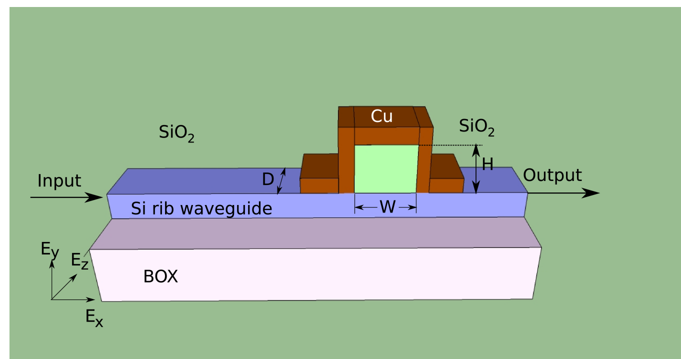

Figure 4.7: Three dimensional view of the schematic plasmonic enhanced stub structure.

As discussed before, the stub was assumed to be filled with an active material such as Ge MQWs on a silicon substrate, whose imaginary part of the refractive index κ and therefore absorption coefficient was varied between 0.01 to 0.05 via an external bias in order to achieve tunable transmission at the output of the waveguide. For particular resonant stub dimensions, Figure 4.8 indicates that system transmission can be controlled when varying κ from an absorbing to a non-absorbing stub conditions. Strong EM mode conversion of the symmetric input field profile into an almost asymmetric field profile after the stub was observed: however in contrast to the 2D FEEM results, the effect occurs in the non-absorbing stub condition, which results in a transmission minimum at κ= 0.01 and maximum at κ=0.05. The reliability of the 2D FEEM results in comparison with the 3D results is discussed later in this section.

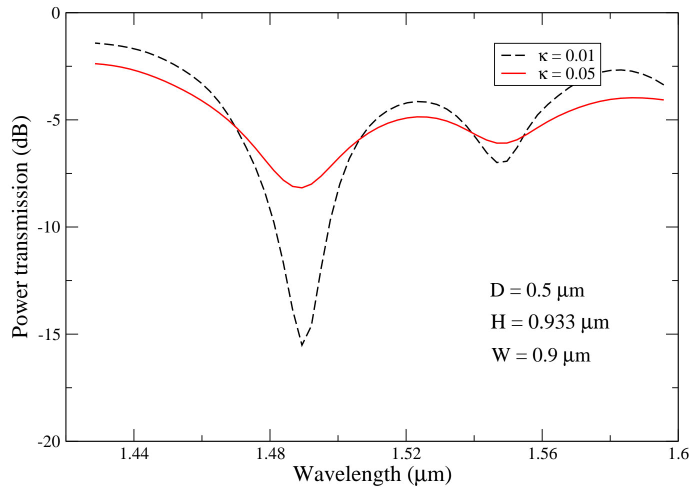

Figure 4.8: Modulation of the power transmission at the output of the stub structure using the 3D FEEM, when switching κ from 0.01 to 0.05.

Figure 4.9 shows the simulated electric field profile (E_y) of the third order lateral and vertical resonant EM modes within the stub, obtained using the 3D FEEM. In accordance with the 2D FEEM results, the maximum of the incident EM mode shifts from the centre of the silicon waveguide and becomes pinned at the metal-dielectric interface as it approaches the metal wings of the structure. The resonant modes at the top of the stub waveguide are incomplete due to the formation of the pinned plasmon

modes at the metal-dielectric interface. Moreover, the bottom of EM resonant modes near the stub-waveguide interface appears to decay into the silicon waveguide, since there is no hard boundary between them.

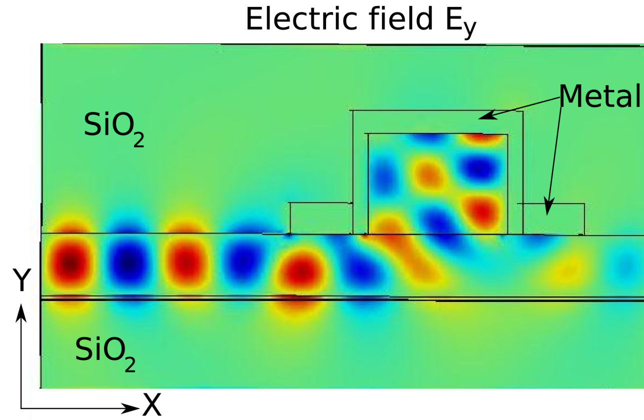

Figure 4.9: Simulated electric field profile (E_y) using the 3D FEEM at κ=0.01 with W=0.9μm and H=0.65μm.

4.3 Optimisation

The main motivation of carrying out EM simulations of the metallised stub structure using a 3D FEEM was to investigate and compare the system performance with respect to the results obtained from the 2D FEEM. Optimisation for the system performance (ER and IL) was carried out for different W, H and D. As described previously, the extinction ratio was obtained by calculating the ratio of the transmission of the system when switching from an absorbing to a non-absorbing stub condition. In order to exclude the loss incurred due to the input and output port mismatch from that incurred only by the metallised stub (i.e plasmonic loss), the dielectric waveguide was simulated without the stub. The residual insertion loss was found to be very small (0.1dB), and therefore it can be neglected.

Figure 4.10 shows maximum ER and minimum IL attainable for different stub widths,

with all other parameters kept fixed. Different lateral orders of electromagnetic resonance were obtained for different resonant W. Very weak EM mode conversion effect was observed for stub widths up to 0.5μm, which resulted in negligible ER (< 1dB), beyond which both the ER and IL increased monotonically for W up to 0.8μm as shown in the figure. For wider stubs ($W > 0.85\mu$m), stronger EM mode conversion was obtained at a reduced value of κ=0.01, in which the symmetric field profile of the input mode was transformed into an almost orthogonal field profile, as shown in Figure 4.11, which leads to reduced coupling with the single mode output waveguide, and therefore results in minimum transmission. On increasing the absorption coefficient (κ=0.05), the EM mode conversion effect is reduced, which results in increased coupling of the EM mode after the stub with the single mode output waveguide, and therefore increased transmission.

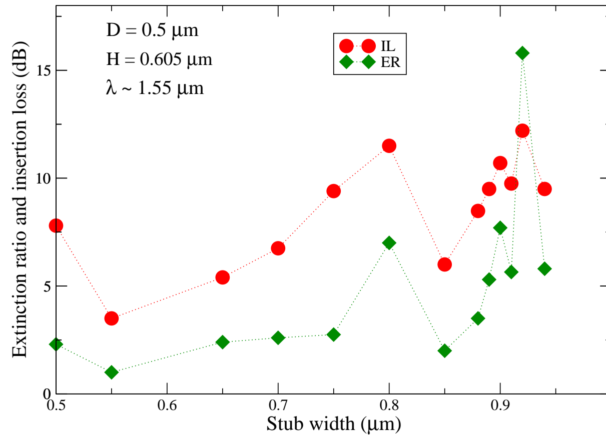

Figure 4.10: 3D FEEM simulated results predicting the extinction ratio and insertion loss as a function of W.

The figure indicates that ER as large as 15.5dB is attainable for W=0.92μm (Figure 4.10), however IL at this width is also quite large ($\approx$12.5dB). Hence, if IL was required to be kept as low as possible, the ER and IL of 8dB and 11dB obtained at W=0.9μm can be considered as a suitable design for further analysis.

Thus, by keeping W=0.9μm, the effect of different H on the system performance was investigated using the 3D FEEM. Figure 4.12 shows the simulated ER and IL as a function of H at 1.55μm wavelength. For $H > 0.6\mu$m, a significant increase in the

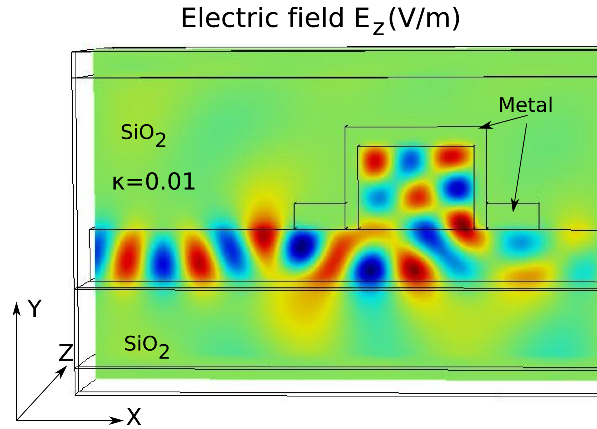

Figure 4.11: 3D FEEM simulated results showing the electric field profile (E_y), in which the symmetric input mode is converted into an almost asymmetric mode in the waveguide section after the stub.

extinction ratio was obtained up to 0.65μm, beyond which it decreases. For H=0.65μm, the figure predicts an ER as large as 23dB because of the large EM mode conversion effect introduced by the stub as shown in Figure 4.13a. On increasing κ to 0.05, the field profile of the outgoing EM mode becomes less antisymmetric (Figure 4.13b), which somewhat improves its coupling with single mode output waveguide, but it still suffers from a large insertion loss of 12.5 dB, as indicated in Figure 4.12.

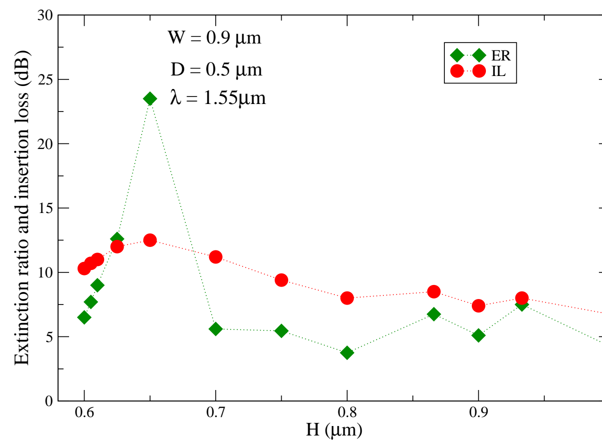

Figure 4.12: 3D FEEM simulated results predicting the extinction ratio and insertion loss as a function of H.

In accordance with the results obtained in the previous chapter, the extent to which the power modulation can be achieved in such a structure depends strongly on the ability of the stub to transform the incoming light into a completely orthogonal EM mode, which could lead to theoretically zero system transmission at the output, and hence infinite ER. However, the system may still have a large IL, making it unsuitable for practical optical modulation purposes. Therefore, the design with H=0.933μm and W=0.9μm, corresponding to a minimum IL of 8dB and a maximum attainable ER of 7.5dB was considered as the best performing device within the practically attainable range of κ.

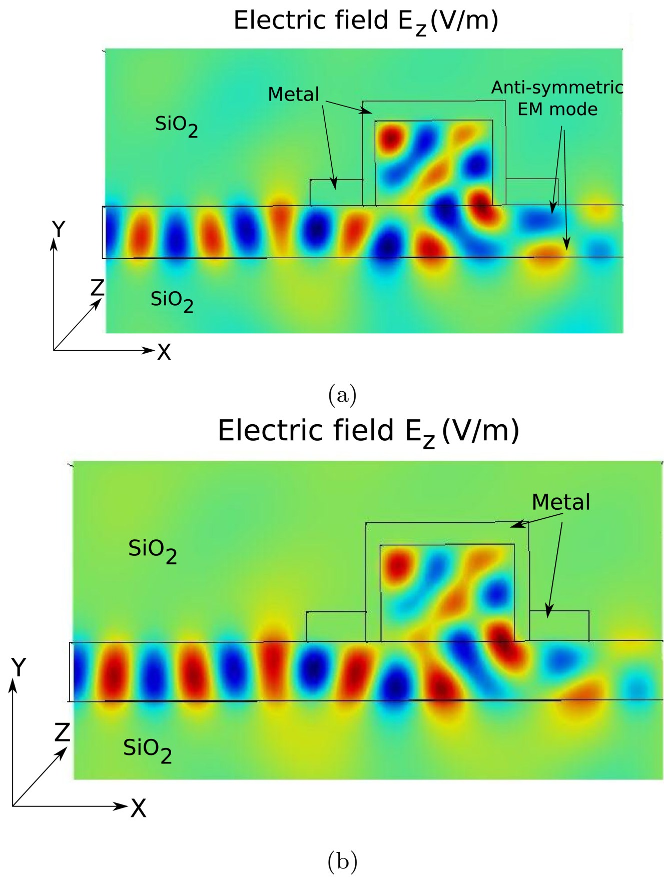

Figure 4.13: Electric field (E_y) profiles along the xy-plane of the 3D simulated stub structure with W=0.9μ and H=0.65μ depicting: (a) anti-symmetric EM modes at κ=0.01 and (b) fairly symmetric EM modes at κ=0.05.

4.4 Discussion

The Q spoiling phenomenon observed for narrow stubs (W <0.4μm) in the 2D FEEM was expected to be the same in the 3D FEEM. For wider stubs ($W > 0.45\mu$m), an EM mode conversion effect using both the 2D and 3D FEEM was observed. However, in contrast to the latter case, the EM mode becomes anti-symmetric for lower values of absorption coefficient of the stub filling (i.e at κ =0.01). The mode conversion effect reduces with increasing κ, which makes the EM field in the output waveguide less anti-symmetric, and therefore improves its coupling with the single mode output waveguide. Thus, it appears that in the 3D modelling, the spoiling of the EM mode conversion effect by the stub is a more dominant effect than the absorption by the stub, and these effects behave in an opposite manner. This is in contrast with the 2D FEEM results in the previous chapter where both the EM mode conversion and increase in absorption coefficient effects occur, i.e the mode conversion effect increases with increasing absorption coefficient of the stub filling (for example, for κ=0.01 to 0.05), resulting in larger transmission at lower values of κ. However, in either case the mode conversion is the major modulating mechanism.

Since the wider stubs which support 2nd or higher lateral orders of EM resonance show better predicted system performance (as discussed in the previous chapter), the 3D modelling of the stub was performed in this regime in order to investigate any performance improvement with respect to the ER and IL.

On comparing the 2D and 3D FEEM results, it was found that, even for a smaller value of W, a larger ER was obtained in the former case. For example, an ER of 10.5dB at W= 0.45μm was obtained using the 2D FEEM, while a negligible ER (<1dB) was achieved using the 3D FEEM. This was attributed to a very small EM mode conversion effect observed for stubs in this regime. Additionally, it must be noted that in the 2D FEEM, both the metallised stub and silicon waveguide extend infinitely in the third dimension (along the z-axis, Figure 4.7). The 2D stub model assumed that there exists a large number of higher order EM modes in the third dimension within the stub as well as the dielectric waveguide. This aids transformation of the symmetric input field

profile into an asymmetric profile of the EM mode in the output waveguide after the stub, which leads to an improved mode conversion effect. However in the 3D FEEM of the stub structure, only the fundamental mode is supported by the structure, and therefore there isn't any mode conversion effect for smaller values of W and H.

It was expected that for larger values of D, the three dimensional modelling may predict better system performance. For this purpose, EM simulations were carried out by varying D from 0.5μm to 2.5μm (with fixed W=0.45μ and H=0.61μm), however no performance improvement with respect to ER and IL was obtained, which was also because of a very weak EM mode conversion effect, resulting in negligible extinction ratios for any value of D.

Nevertheless, the study carried out using the 2D FEEM was useful in gaining an understanding that, in order to achieve a pronounced EM mode conversion effect, the stub dimensions (W and H) must be increased. This was indeed verified from the 3D FEEM results, which predicted an increased ER for larger W, particularly for $W >$ 0.85μm shown in Figure 4.10. The transmission line theory (or Q spoiling phenomenon) for narrow stubs, observed in 2D simulations may also apply for 3D simulations, however for wider stubs the EM mode conversion effect was mostly responsible for achieving maximum optical modulation.

Chapter 5

Conductor-gap-dielectric systems and MOS-type optical modulators

5.1 Introduction

In this chapter, theoretical investigations into a special type of plasmonic structure are carried out, in which a low index gap layer is sandwiched between a conductor and a high index dielectric layer. The potential for application of such a conductor-gap-dielectric (CGD) system in an optical modulator is explored. Based on the CGD system, a double waveguide Mach-Zehnder (MZ) structure and its single waveguide variant are investigated for modulation purposes, in which each arm of the MZ device comprises a metal-insulator-semiconductor-insulator-metal structure.

Optical modulation in a silicon photonic device can be achieved by electrically biasing the structure to modulate the induced free carrier density in the silicon layer. This changes both the real and imaginary parts of the effective mode index of the electromagnetic (EM) mode, and optical modulation based on these mechanisms are defined as electro-refractive or electro-absorption modulation, respectively [106–108]. A change in the real part of the effective mode index ($\triangle n_{eff}$) is typically used in an interference-based Mach-Zehnder (MZ) device which comprises two waveguides with a splitter and a

combiner arrangement. The application of MZ structure as shown by the cross-sectional view in Figure 5.1 has been theoretically investigated for the optical modulation purpose. The lengths of the arms of the MZ device are chosen so that a bias applied to one of the arms introduces an optical π phase change in the EM mode relative to the other arm. This leads to destructive interference between the EM modes from the two arms of the MZ device in a biased state, resulting in minimum transmission (also known as blocking or off state). Conversely, constructive interference occurs in an unbiased state (also known as transmitting or *on* state). Thus, the light intensity at the output of the MZ device can be varied by switching between the two states.

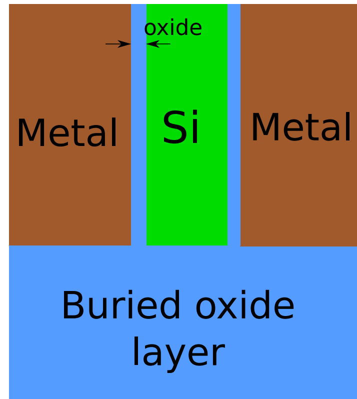

Figure 5.1: Cross-sectional view of one arm of the double waveguide Mach-Zehnder device comprising of metal-insulator-semiconductor-insulator-metal structure.

5.2 Conductor-gap-dielectric systems

A low index gap layer within the CGD system supports a strongly confined plasmon mode due to the large refractive index contrast between the gap and dielectric layers[109]. The EM mode confinement of such a plasmon mode is quite sensitive to the variation in the refractive index of the underlying dielectric material. Figure 5.2 shows the simulated electric field intensity (E_y) of a strongly confined gap plasmon mode in the conductor-

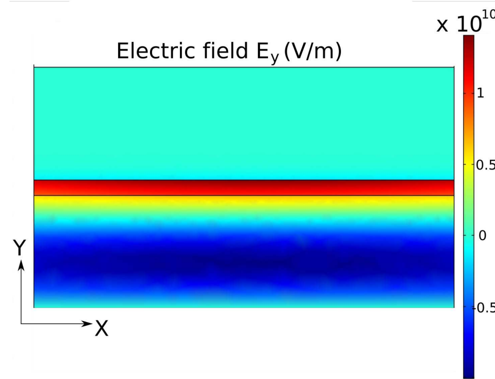

Figure 5.2: Electric field E_y of the gap plasmon mode, which is strongly confined within the gap layer sandwiched between the metal and high index dielectric layers.

gap-dielectric (CGD) system obtained using the FEEM. Here, silicon and germanium are used as the gap and dielectric layers with refractive indices of 3.48 and 4.0 respectively, thus providing the necessary index contrast between the layers to confine the EM mode within the gap layer. Copper was used as the metal with its refractive index obtained from the table 2.1.

EM simulations were carried out to analyse the effect of changes in gap thickness (t_{gap}) on the confinement factor of the gap plasmon mode as shown in Figure 5.3, where the dielectric layer thickness was kept at 400nm. The confinement factor of the mode was determined by calculating the ratio between the power of the confined gap plasmon mode inside silicon (P_{Si}) and that within the CGD system (P_{tot}), for a given t_{gap}. On increasing t_{gap}, the proportion of the EM mode within the gap layer decreases while that within the dielectric layer increases, resulting in a reduced EM mode field intensity, and therefore a reduced confinement factor within the gap layer. However, the confinement factor of the gap plasmon mode becomes very sensitive near the t_{gap} ranging from 50nm to 60nm, during which a sharp reduction of the mode confinement within the gap layer was observed. This is also known as the critical range of t_{gap} for the CGD system. On further increasing t_{gap} ($>$ 70nm), the EM mode becomes increasingly confined within the dielectric layer, resulting in a very low confinement factor within the gap layer.

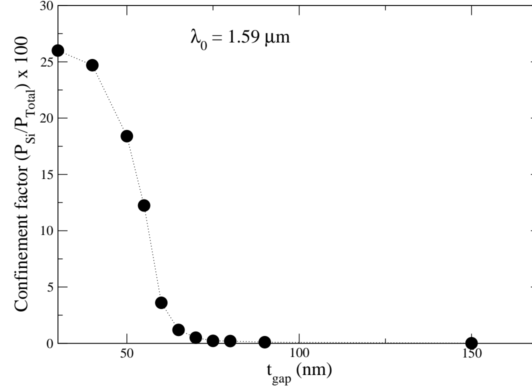

Figure 5.3: Dependence of the confinement factor (P_{gap}/P_{total}) of the highly confined plasmon mode on t_{Si}, obtained using FEEM.

The propagation loss per unit length of the plasmon mode within the CGD system (Figure 5.2) can be determined from the imaginary part κ of the effective mode index, which is also related to the absorption coefficient α as discussed before. Figure 5.4 shows the propagation loss of the CGD system as a function of t_{gap}, obtained using the FEEM. A large reduction in the propagation loss from 900 dB/cm to 140 dB/cm occurs for the same range of t_{gap} in accordance with the behaviour of the confinement factor (Figure 5.3). Previously, analytical work was carried out by Avrutsky et al. [109] on the conductor-gap-dielectric systems (Au-Si-Ge), which predicted lower propagation loss than that shown in the figure at t_{gap}=61nm. However, the structure extended infinitely with respect to the conductor and dielectric layer thicknesses, which aids mode confinement within the gap layer, resulting in a reduced propagation loss. Such a CGD system cannot be applied in practical situations. In contrast, a finite CGD structure is considered here with fixed dimensions for potential application in a modulator, where the change in imaginary part of the refractive index (and therefore κ) via an externally applied bias is explored using the FEEM. If the gap layer is doped (with either n^+ or p^+ dopants), a change in the κ of the effective plasmon mode index can be achieved by varying an external bias, which in turn modifies the electro-absorption response and therefore the transmission through the system [110].

Keeping t_{gap}= 60nm, the propagation loss for a 100μm long CGD system as a function of the change in refractive index of the gap (Si) layer was obtained as shown in Figure 5.5. For a particular length, the extinction ratio (ER) due to the CGD multilayer system was determined by calculating the difference between the propagation loss of the system for the two states. For this length, the insertion loss (IL) can also be determined from the propagation loss incurred by the plasmon mode in the transmitting state. The predicted IL does not include the coupling loss to the device or the loss associated with the geometry of the final device, but only the plasmonic loss due to the CGD system alone. Figure 5.5 shows a predicted ER and insertion loss (IL) of 8.4dB and 5.7dB respectively for a 100 μm long CGD system, obtained for a change in Si index ($\triangle n_{Si}$) of $\approx 7\times10^{-2}$.

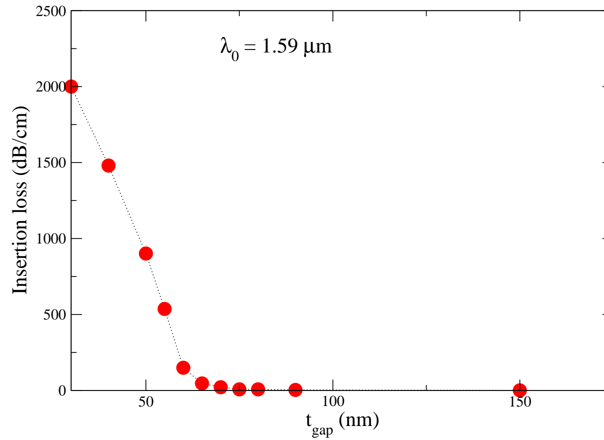

Figure 5.4: Dependence of the plasmon mode propagation loss per unit length (dB/cm) through the CGD system on t_{gap}

$\triangle n_{Si}$ of $\approx$ 7x10^{-2} is quite difficult to realise in practice, but with some modification in the CGD structure, for example, by including a thin oxide layer between the metal and gap layers, a large change in Si index may be achieved via the charge carrier accumulation effect when a bias is applied [111–113]. Figure 5.6 shows the electric field intensity (E_y) of the gap plasmon mode in a metal-oxide-Si-Ge (MOS-Ge) system, in which SiO_2 was used as the oxide. As discussed before, due to a large index contrast between the oxide

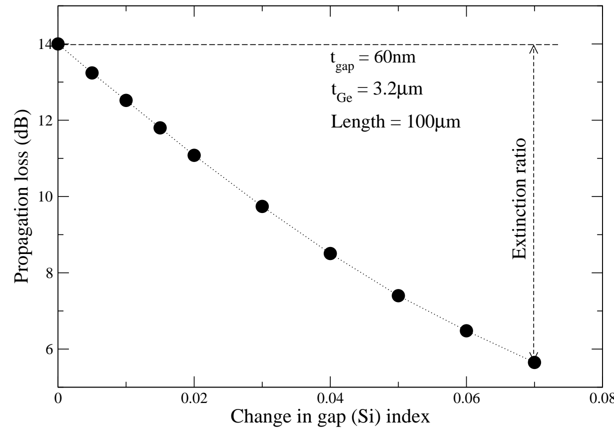

Figure 5.5: Dependence of the plasmon mode propagation loss in a 100μm long CGD system on the change in gap (Si) layer refractive index.

and gap layers, the EM mode prefers to sit within the low index oxide layer, resulting in a high electric field intensity within the oxide (red region) as indicated in the figure, which then decays into the underlying silicon (light blue) gap layer. This results in a significant reduction of the plasmon mode confinement within the gap layer in the MOS-Ge system.

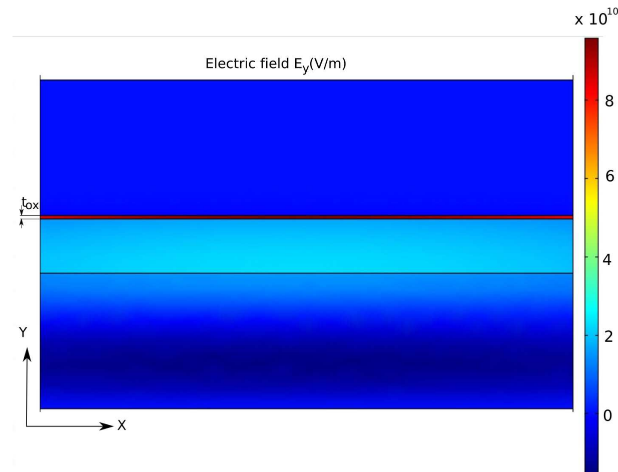

Figure 5.6: Shows the electric field E_y of the plasmon mode strongly confined within the oxide layer and sparsely confined within the gap (Si) layer.

EM simulations were then carried out to determine the propagation loss of the gap

plasmon mode in the modified MOS-Ge system for different oxide thicknesses (t_{ox}) and t_{gap} using the FEEM. For a fixed t_{gap}, the propagation loss of the plasmon mode decreases with decreasing t_{ox}, and therefore a thinner oxide layer ($t_{ox} < 3$nm) was considered suitable to achieve lower IL for modulation purposes. Keeping t_{ox}= 2nm, propagation loss for a 100μm long MOS-Ge system as a function of t_{gap} was obtained using the 2D FEEM, as shown in Figure 5.7. The loss generally decreases monotonically with increasing t_{gap}, which occurs due to increased EM mode confinement within the gap (Si) layer, leading to absorption of a decreasing proportion of the mode by the metal, and therefore resulting in a reduced propagation loss. However, in contrast to the CGD system (Figure 5.4), the presence of an oxide layer affects the sensitivity of the propagation loss of the MOS-Ge system with increasing t_{gap}. The overall system performance degrades due to the presence of an oxide layer, resulting in a very low ER of only 1dB and an insertion loss of $\approx$ 3dB for a 100μm long MOS-Ge system.

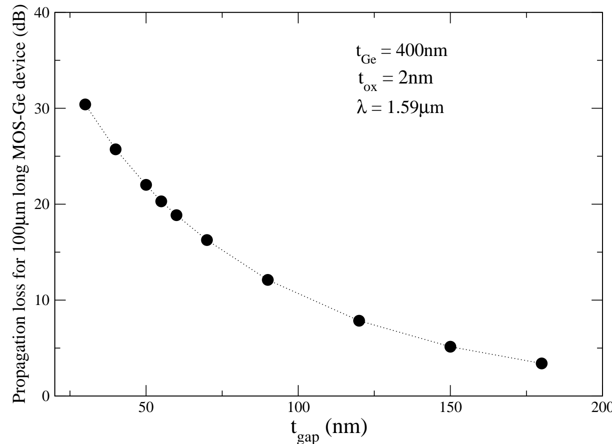

Figure 5.7: Dependence of the plasmon mode propagation loss (dB) in a 100 μm long MOS-Ge waveguide device on the Si layer thickness, t_{gap}.

Nevertheless, MOS structures have been previously investigated and demonstrated for optical modulation purposes. For example, a single waveguide plasmonic modulator (plasmostor) comprising metal-oxide-Si-metal structure was experimentally demonstrated by Dionne et al. [46], as shown in Figure 5.8. The structure was designed to

support (i) a gap plasmon mode within the thin oxide gap layer and (ii) a guided mode within the silicon dielectric layer. The silicon layer was doped with an n type impurities. In the off state, both a photonic mode in the silicon guided layer and a plasmon mode in the thin oxide channel were supported by the structure. The plasmostor was designed to operate such that the photonic mode was extremely sensitive to the changes in complex refractive index of the layers. In the *on* state, an electron accumulation layer is formed near the oxide-Si interface, pushing the photonic mode into the cut-off region, where the remaining plasmonic mode was guided through the oxide channel into the output slit. Thus, most of the plasmon field was channelled through the oxide region, while the field intensity inside the Si region was significantly reduced. The modulation in the device was achieved by choosing the source-drain distance such that the photonic and plasmon modes interfere destructively in an unbiased condition at the output slit, while a maximum transmission was achieved in the biased condition. Although the propagation loss of the plasmon mode incurred along the length of the device was very small ($\approx$ 1dB for an active length of $\approx 2.2\mu$m), the structure suffered from approximately 16dB coupling losses.

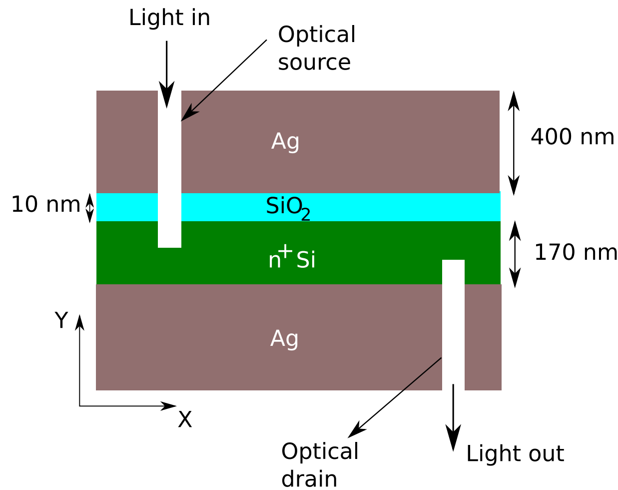

Figure 5.8: Cross sectional schematic diagram of the plasmostor modulator proposed in [46].

Motivated by the above work, theoretical investigations of the application of a single

waveguide MOS-Ge structure in an electro-optic modulator were carried out, using the FEEM. Keeping t_{ox} and t_{gap} at 10nm and 160nm (similar to that chosen in the plasmostor device), EM simulations were carried out in order to obtain the gap plasmon and dielectric guided modes within the MOS-Ge system. It was indeed found that these modes existed at different complex mode indices. Using their effective mode indices, the combined electric field intensities in the *on* (I_{on}) and *off* (I_{off}) states could be written as:

$$
\begin{aligned}
I_{off} &= \mid e^{i(n_1+ik_1)zk_0} + Ae^{i(n_2+ik_2)zk_0} \mid^2 \\
I_{on} &= \mid e^{i(\bar{n_1}+i\bar{k_1})zk_0} + Ae^{i(\bar{n_2}+i\bar{k_2})zk_0} \mid^2
\end{aligned}
$$

where A is the amplitude of the guided mode field (relative to that of the gap mode). n_i, k_i and $\bar{n_i}$, $\bar{k_i}$ for i=1 and 2, are the combined complex effective indices of the plasmon and guided modes in the *off* and *on* states, and z is the direction of propagation. Using Eq.5.1, variation of the electric field intensity of the superimposed gap plasmon and guided modes along the propagation distance was obtained numerically when switching between the two states, as shown in Figure 5.9a. In this case, the amplitude (A) of both the guided and plasmon modes at the input were kept the same. A shift in the electric field intensity in the *on* state relative to the *off* state can be observed, which produces a maximum intensity contrast at a propagation distance of $\approx$ 23 μm indicated by the point p in the figure. Thus, if the MOS-Ge device length was chosen to be 23μm, then the dielectric guided mode and gap plasmon mode interfere destructively in the *on* state and constructively in the *off* state. The insertion loss (IL) of the structure at this length can then be determined by calculating the ratio between the maximum intensity at z = 0 (I_{off} =4) and intensity at the point p in the figure, resulting in an IL of 2.04dB. The extinction ratio can also be determined by calculating the intensity contrast between the two states at this point, resulting in an ER of $\approx$ 9dB for $\triangle n_{Si}$ = 8×10^{-2}. If the amplitude A of the guided mode was assumed to be a half the gap-

plasmon mode at the input of the MOS-Ge system, then almost zero intensity would occur at a certain propagation distance (for example at 22.5μm) as shown in Figure 5.9b, which theoretically gives an infinite ER together with very low insertion loss. However, launching both the plasmon and guided modes with different amplitudes could be very challenging in practice.

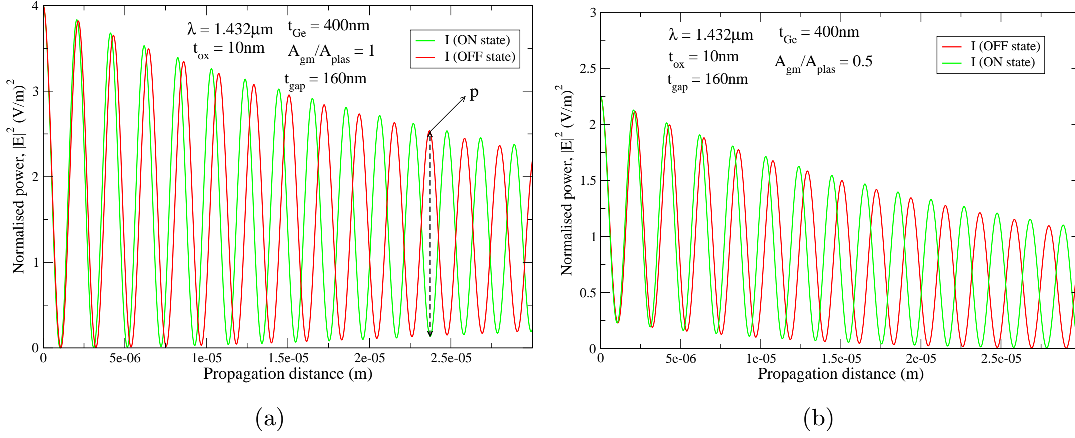

Figure 5.9: The electric field squared of the superimposed gap plasmon and dielectric guided modes in a single waveguide MOS-Ge structure along the propagation distance when switching between the *on* and *off* states when the amplitude ratio between the guided mode and plasmon mode is: (a) 1 and (b) 0.5.

Alternatively, an interference-based Mach-Zehnder (MZ) configuration was investigated, in which each arm comprises a MOS-Ge structure, and only the gap plasmon modes were used for modulation purposes. The length of each arm was chosen such that the plasmon modes from the two arms of the MZ device interfere destructively at the output of the MZ device. This happens when the plasmon mode in one of the arms undergoes a π phase change relative to the other arm, which in turn can be achieved by an externally applied field. In the absence of any bias in both the arms, maximum field intensity of the plasmon mode was obtained at the output of the MZ MOS-Ge system. Thus, using the complex refractive indices obtained from the FEEM, the variation in the electric field intensities of the plasmon mode with respect to the propagation distance

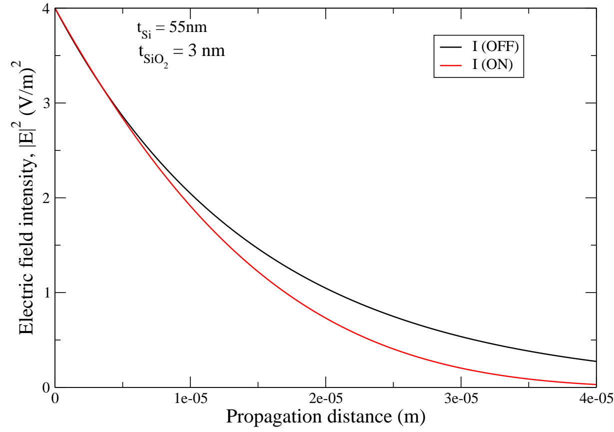

Figure 5.10: The electric field squared of the gap plasmon mode along the propagation distance in the MOS-Ge MZ configuration between the *on* and *off* states.

was numerically calculated in both the *on* and *off* states, as shown in Figure 5.10. In contrast to the single waveguide MOS-Ge device (Figure 5.9a), due to a strong absorption of the plasmon mode by the metal, the field decays quite strongly as it propagates along the length of the device, resulting in a very small intensity contrast, and hence a very small ER between the two states.

However, the subwavelength confinement nature of such a plasmon mode can be used in metal-oxide-semiconductor plasmonic structures to achieve optical modulation due to a large effect of charge carriers near the oxide-semiconductor junction, which will be explained in detail in the following section.

5.3 Electro-optic MOS plasmonic modulators

From the previous section, it was established that a highly confined subwavelength plasmon mode exists in a low index gap layer sandwiched between the metal and high index dielectric layer. Several silicon based plasmonic enhanced optical modulators, which use the change of the real or imaginary part of the effective mode index have been previously investigated [46, 78, 114–117]. A MOS plasmonic slot waveguide MZ modulator was theoretically investigated for the limiting case of large device heights [114]. Unlike the single

waveguide plasmostor device described in the previous section, each arm of the MZ device comprises metal-SiO_2-Si-metal (MISM) structure. A V-shaped splitter/combiner configuration was used for coupling light into the structure. As explained earlier, the device operates as a MZ interference modulator. The authors neglected Quantum mechanical effects when modelling the distribution of electrons across the thin silicon layer, giving rise to a large predicted peak electron density at the oxide-Si interface.

In this section, a silicon compatible Mach-Zehnder plasmonic modulator of finite cross-section was investigated using a 2D FEEM [73]. Each arm of the MZ device comprises a metal-insulator-semiconductor-insulator-metal (MISIM) structure. Note that, unlike the MZ structure described above, each arm comprises an insulator layer at both sides of the Si layer. Figure 5.11 shows the cross-sectional view of one arm of the MISIM MZ structure on a buried oxide layer. A very fine triangular mesh density was used with an element size of ≈0.2nm and 2nm in the insulator and semiconductor layers, respectively. For all the further investigations in this section, aluminium was used as the metal layers, with complex refractive index given in table 2.1 from [82] for a wavelength of 1.55 μm. Aluminium is a good choice of metal since it is CMOS compatible and abundantly available.

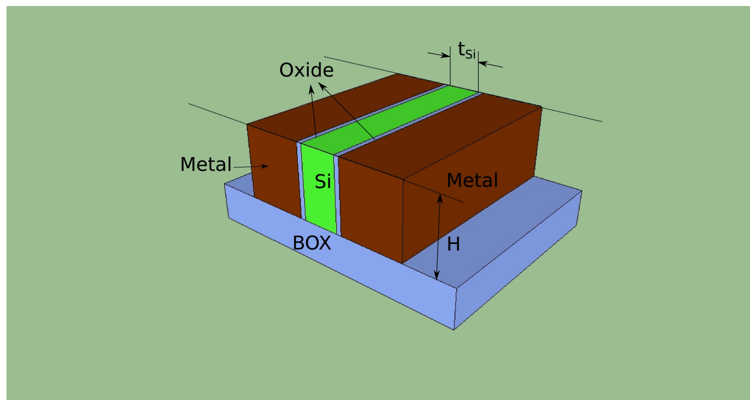

Figure 5.11: Schematic of an arm of the MISIM MZ modulator.

5.3.1 Inversion and accumulation mode devices including quantum mechanical effects

When the thicknesses of the MOS-type structures approaches nanoscale dimensions, it becomes necessary to include quantum mechanical (QM) effects for an accurate theoretical modelling of such devices. With gate voltage applied, a very large electric field across the oxide-Si interface leads to the formation of a potential well in silicon. Consequently, confinement of the charge carriers in the direction normal to the oxide-Si interface takes place, leading to the energy quantisation with discrete energy states, localised near the interface, as shown in Figure 5.12 [118, 119]. Due to the QM effects, the shape of the electron density profile across the semiconductor layer, especially near the oxide-Si interface, differs quite significantly from the situation when these effects are neglected [120, 121]. The electron density peaks near the interface have a large influence on the electromagnetic behaviour of the confined mode within the MOS structure. Thus a self-consistent one-dimensional Schrodinger-Poisson (SP) solver [122] was used to model the electron density distribution across the thin Si layer in one arm of the MISIM device.

Both accumulation and inversion mode MISIM devices were considered. For the accumulation mode device, an n^+ type MISIM structure was considered, where a positive bias applied to the metal attracts electrons, forming an accumulation charge layer (ACL) in the Si region near the oxide-Si interface. In the case of inversion mode device, a p^+ type MISIM structure was considered, where a positive bias applied to the metal attracts the minority carriers, forming an inversion layer near the interface. Electrons are generally more effective than holes in changing the refractive index of silicon: therefore, the device should be designed such that a large change in electron density occurs when a bias is applied. Figures 5.13a and 5.13b show the electron density distributions achieved in the MISIM accumulation mode device with a donor doping density of $n^+ = 5\text{x}10^{18}\text{cm}^{-3}$ and an inversion mode device with an acceptor doping density of $p^+ = 2\text{x}10^{16}\text{cm}^{-3}$ for different biases. Both figures show a high electron concentration at the oxide-Si interface. Due to the QM effects, the shape of the electron density distribution differs significantly from that in the classical approximation [123].

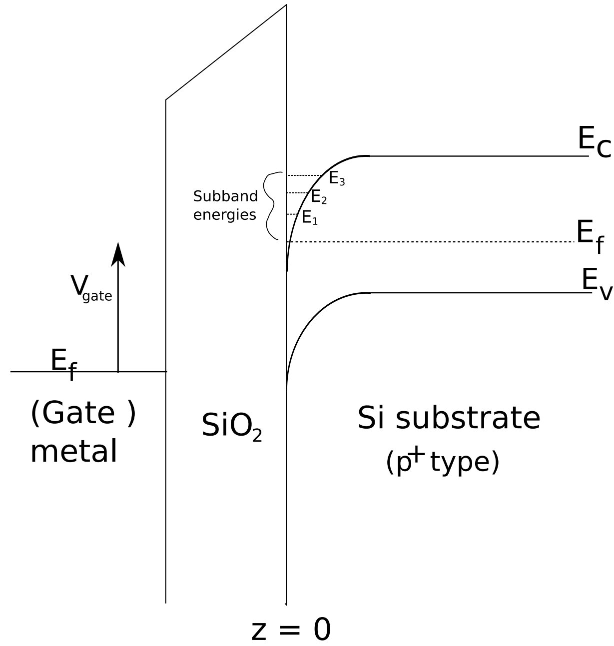

Figure 5.12: A 2D schematic band energy diagram of a p^+-type metal/SiO_2/Si structure in the inversion mode condition.

The quantum confinement effects can be observed in the region close to the interface for both types of device, in which case the peak electron density in the Si region was shifted away from the oxide-Si interface in contrast to the classical model where the peak electron density is located at the interface [123]. Since, for a p-doped silicon in the inversion mode device, some part of the applied bias is spent to drive the holes away, slightly larger electron concentration was achieved in the MISIM accumulation device than the inversion mode device. Hence, the MISIM accumulation mode device was considered for all further investigations in this chapter.

Moreover, an even larger electron density in the Si layer can be achieved for an applied bias with the use of high-K oxide material (where K is the dielectric constant of the oxide). Therefore, HfO_2 with $K \approx 17$ is advantageous over SiO_2. Since the effective oxide thickness of HfO_2 is smaller than that of SiO_2, a smaller potential drop occurs within the oxide layer, which means that a larger portion of the applied

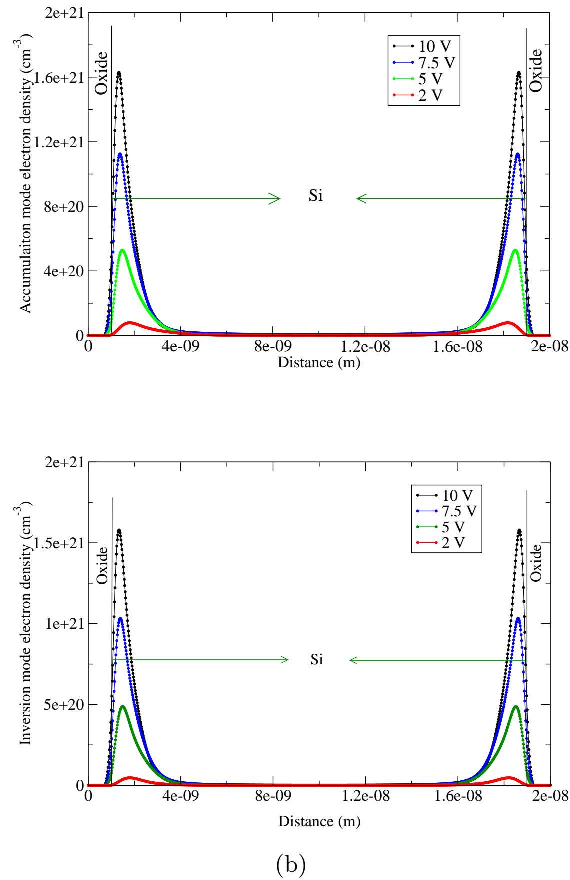

(b)

Figure 5.13: The electron density distribution across the Si layer in the MISIM accumulation and inversion mode structures.

bias is available across the Si layer to cause an accumulation of electrons near the oxide-Si interface. Figure 5.14 shows the electron density distribution across the Si layer using HfO_2 as the oxide layer in the MISIM accumulation mode device. For an applied bias of 7.5V, the peak electron density near the oxide-Si interface with the use of HfO_2 is larger by a factor >6 than that obtained using SiO_2 (Figure 5.13a). Another advantage of using of HfO_2 was related to the electromagnetic behaviour of the optical mode within the MISIM structure, which will be discussed in the next section.

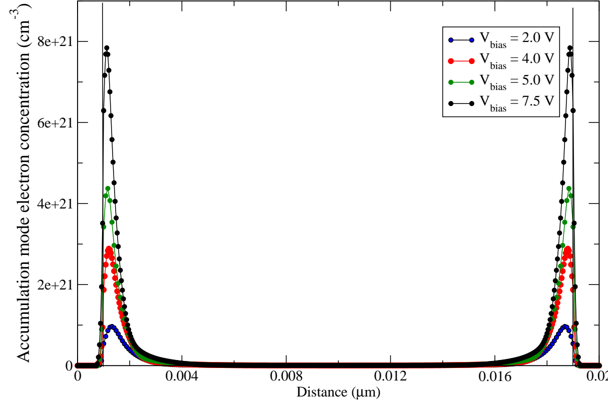

Figure 5.14: The electron density distribution across the Si layer in the MISIM accumulation mode structure using HfO_2 as the oxide material.

5.3.2 2D optimisation and electro-optic modulation

Optimisation of one arm of the MISIM MZ device with respect to its physical parameters was carried out using a 2D FEEM to minimise the insertion loss. Figure 5.15 shows the electric field distribution (E_x) of the electromagnetic (EM) mode across the Si layer in the off state. The EM mode is strongly confined within the thin oxide layers, and decays further into the Si region forming a subwavelength gap-plasmon mode between the metal and the Si layer, which was also discussed earlier in chapter two [124, 125]. Figures 5.16a and 5.16b show the electric field (E_x) and refractive index (n) profiles in the Si layer along the line normal to the oxide-Si interface for different applied biases. The exact electron density distribution obtained for an applied bias across the Si layer using the SP model[122] was imported into the EM model to calculate the $\triangle n_{eff}$ of the gap plasmon mode within the MISIM structure. In the *on* state, for example at V_{bias} = 4V (Figure 5.16a), the electric field (E_x) intensity obtained in the ACL near the oxide-Si interface was much larger than that obtained in the oxide layer, while the converse was true in the off state. This is because the refractive index of the EM mode in the Si region near the interface becomes much smaller than that of the oxide layer due to the formation of ACL (Figure 5.16b). This results in a large EM mode overlap of the plasmon mode with the Si region, resulting in a large $\triangle n_{eff}$ of the confined plasmon

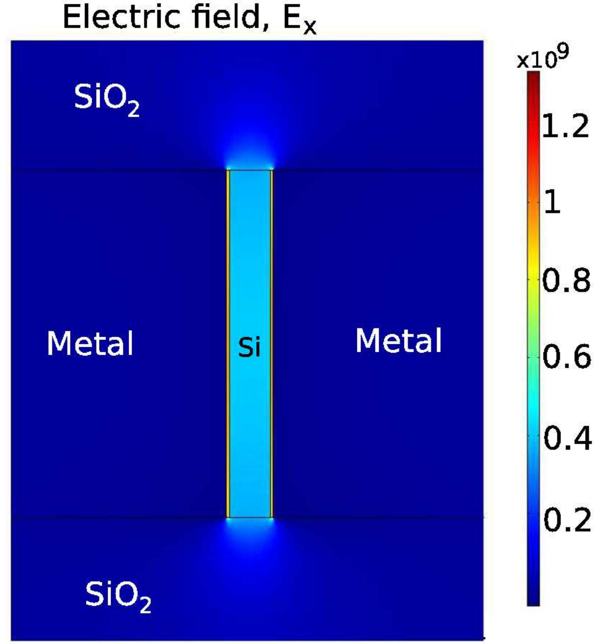

Figure 5.15: The two-dimensional electric field distribution (E_x) of the confined gap plasmon mode in the *off* state of the MISIM accumulation mode device.

modes between the two states. For $V_{bias} > 4$ V, the above effect increases so that the permittivity of the EM mode within the ACL becomes negative (see Eq. 5.1), which leads to a reduced $\triangle n_{eff}$. Thus, an applied bias of 4V was considered suitable for maximum system performance.

The Soref model is often used to calculate the change in refractive index for an applied bias at 1.55 μm wavelength [112]; however, the scattering dependent Drude model has shown to be a better approximation in heavily doped Si [114, 126]. This is because the latter also includes the effects of acoustic phonon scattering to obtain the change in free carrier absorption with varying electron concentration, which is neglected in the Soref model [126]. The change in refractive index ($\triangle n$) according to the Drude model at λ=1.55μm is given by:

$$\triangle n = -[1.2 \times 10^{21} \triangle N_e + 8 \times 10^{-22} \triangle N_h] \tag{5.1}$$

where N_e and N_h are the electron and hole concentrations.

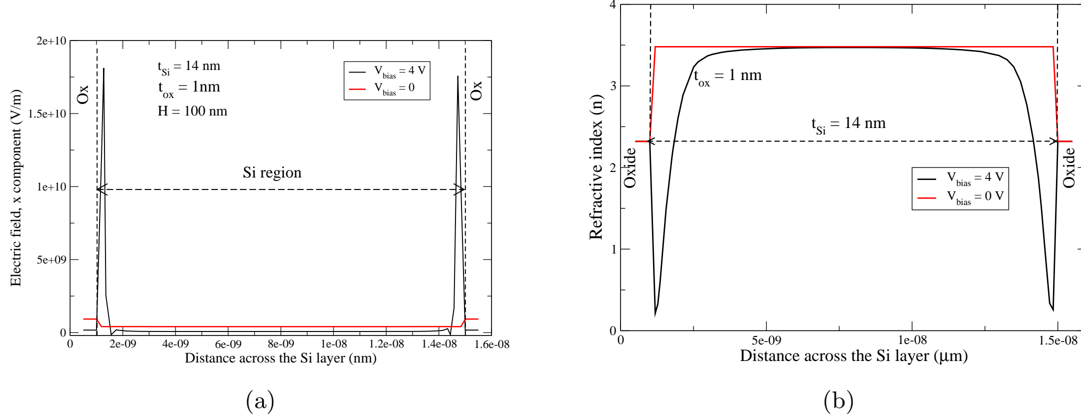

(a) (b)

Figure 5.16: *a*). The electric field profile across the Si layer in the MISIM accumulation device in the *on* and *off* states. *b*). Refractive index profile across the Si layer in the MISIM accumulation device at V_{bias} = 0 and 4 V.

The device loss of the structure is defined as the loss incurred by the plasmon mode as it propagates along the length of the device. The length (L_π) required to achieve destructive interference between the optical modes from the two arms of the MZ device was calculated from $L_\pi = \lambda_0 / 2 \triangle n_{eff}$ (where λ_0 is the free space wavelength) [114]. Figure 5.17 shows the dependence of the device loss on the height (H) of the structure using both the Soref and Drude models, with the other parameters kept fixed. For smaller values of H ($<$ 40 nm), a large portion of the EM mode spills from the top and bottom openings of the MISIM structure, which leads to a reduced confinement of the EM mode within the structure. Thus, a smaller proportion of the EM mode experiences the variation in the electron density, resulting in an increased device length and therefore an increased device loss. However, as H increases, the EM mode confinement improves, which results in a decreased device loss. For $H >$ 100nm, the EM mode is almost fully confined in the Si region, and therefore any further increase in H does not significantly change $\triangle n_{eff}$, and hence no additional improvement in device loss is obtained. Since the Drude model (see Eq. 5.1) predicts a larger $\triangle n_{eff}$ for a given applied bias (which results in a shorter device length), the device loss was found to be much smaller than that obtained using the Soref model.

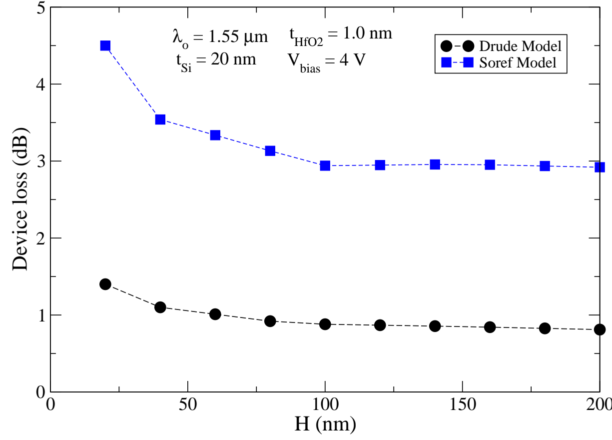

Figure 5.17: Effect of variation of H of the MISIM structure on the device loss.

Figure 5.18 shows the maximum attainable $\triangle n_{eff}$ of the plasmon mode in the MISIM accumulation mode device for a range of applied biases and different silicon layer thicknesses (t_{Si}), with the other parameters kept fixed. As discussed before, the accumulation mode electron density profiles obtained from the QM model for a given t_{Si} and V_{bias} were employed in the EM model to calculate $\triangle n_{eff}$. The large electron densities obtained in the Si layer help in achieving a large perturbation of the complex mode index of the plasmon mode. The size-quantisation effect near the oxide-Si interface leads to a slightly broader peak electron density near the interface than within the classical approximation [114], which aids large overlap of the plasmon mode with the ACL in the Si region. Additionally, the use of HfO_2 rather than SiO_2 as the oxide layer leads to a reduced refractive index contrast between the oxide and Si layers, which results in reduced confinement of the EM mode in the thin oxide layer, and hence a larger influence of the ACL in the Si region when a bias is applied. As discussed earlier, for $V_{bias} > 4$V a very large peak electron density is obtained in the ACL near the interface (see Figure 5.14), which leads to an increasingly negative dielectric permittivity of the EM mode in the ACL close to the interface (Figure 5.16b), therefore resulting in a reduced $\triangle n_{eff}$.

Figure 5.19 shows the effect of increasing the silicon layer thickness on the device loss for a fixed H of 100nm and V_{bias}= 4V. The device loss was calculated using both the

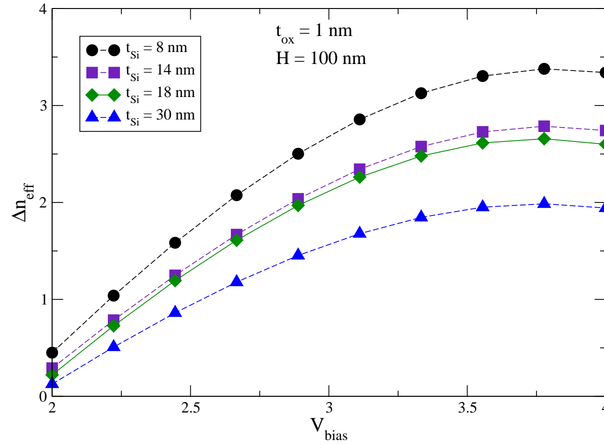

Figure 5.18: Change in effective mode index obtained in the MISIM structure as a function of bias for different silicon layer thickness.

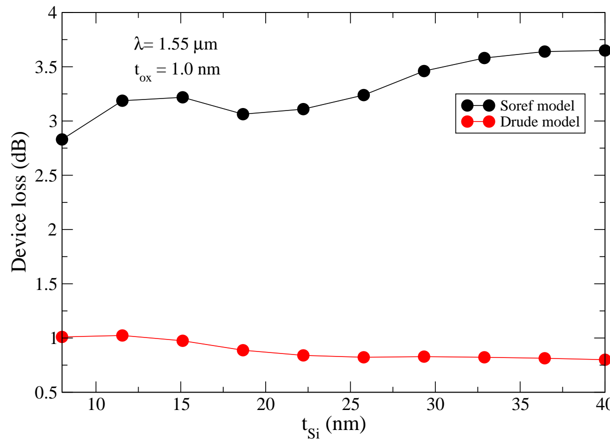

Figure 5.19: Influence of varying silicon layer thickness (t_{Si}) on the device loss.

Soref and Drude models. The loss increases with increasing t_{Si} using the Soref model. This is due to a reduced EM mode overlap with the ACL in the Si region, which leads to a reduced $\triangle n_{eff}$ of the plasmon mode within the MISIM device, and hence an increased device loss. However, the device loss obtained from the Drude model shows the opposite effect, in which the loss increases slightly with decreasing t_{Si}, which can be explained as follows. A very large $\triangle n_{eff}$ from the Drude model results in a very small device length ($\leq$ 0.25 μm). Although the $\triangle n_{eff}$ of the plasmon mode within the device increases

with decreasing t_{Si} (see Figure 5.18), the absorption loss due to the metal increases significantly as shown in Figure 5.20. For very small length-scales, the loss is mostly dominated by the absorption of the plasmon mode due to the metal, hence increasing the overall device loss (Figure 5.19). The simulated results predicted the device loss to be as low as $\leq$ 1dB (device length $\approx$0.25μm) for a broad range of t_{Si} from 20-40 nm, when using the scattering dependent Drude model.

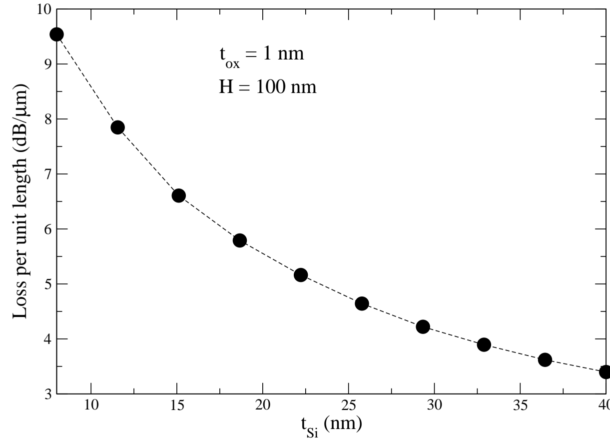

Figure 5.20: Absorption loss per unit length with increasing t_{Si} in a MISIM accumulation device in an unbiased state.

Figure 5.21 shows the electron concentration distribution across the Si layer in the MISIM accumulation device for different oxide layer thicknesses (t_{ox}) for V_{bias}= 4V, with all other parameters kept fixed. The electron density decreases with increasing t_{ox} because of the increased potential drop across the oxide layer. The effect of varying t_{ox} on the system performance was investigated by importing the electron concentration distribution obtained from the electrostatic simulations into the EM model. Figure 5.22 shows the device loss dependence on different t_{ox}. The device loss increases significantly with increasing t_{ox} because a smaller portion of the applied bias is available across the Si layer, which strongly affects the electron density distribution especially at the ACL (for example the peak electron density for t_{ox} = 1nm is almost 1.8 times that for t_{ox} = 2nm, Figure 5.21). Furthermore, the EM mode confinement in the oxide layer increases,

which leads to a reduced EM mode overlap with the Si region, resulting in a reduced $\triangle n_{eff}$. Hence, to achieve minimum device loss, the oxide layer thickness of the MISIM arm of the MZ modulator must be as small as possible.

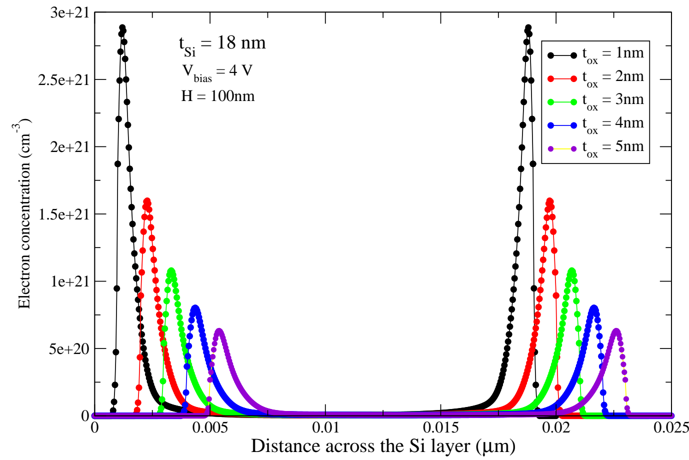

Figure 5.21: Electron density distribution across the Si layer in the MISIM accumulation mode device as a function of varying t_{ox}.

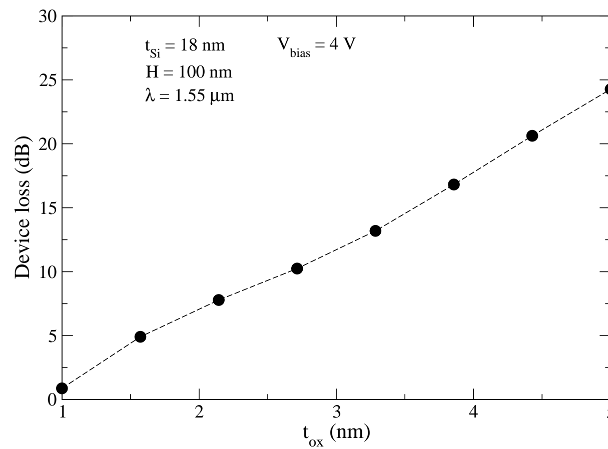

Figure 5.22: The influence of varying t_{ox} on the device loss.

5.3.3 Asymmetric biasing scheme

The insertion loss of the MISIM MZ accumulation mode device can be further reduced by minimising the device length. This can be achieved by implementing a configuration where in one of the arms of the MZ device a fixed $\pi/2$ phase shift is introduced, e.g. by incorporating a dielectric waveguide section of appropriate length in one arm of the MZ device (for example at the beginning and end of the left arm, as shown in Figure 5.23). A positive bias applied to this arm (while the other arm is unbiased) will then introduce another $\pi/2$ phase shift causing destructive interference with the optical mode from the other arm at the output of the MZ device (see Figures 5.24 a and b), resulting in logic 0 (Figure 5.24c). When the bias to the left arm is removed, a positive bias applied to the other arm will cause the plasmon modes from the two arms of the MZ device to be in phase (since both the EM modes will now have a phase of $\pi/2$), resulting in constructive interference between the two modes, resulting in logic 1 (Figure 5.24c). Since the free carrier absorption loss in silicon is much smaller than that incurred by the metal, the loss in each arm of the MISIM device is essentially the same in both the biased and unbiased states.

Thus, an asymmetric bias alternating between the two arms of the MZ device was required in order to switch between the constructive and destructive interference states, also known as push-pull operation [127]. Since the two arms of the MZ device are biased asymmetrically, they must be insulated by an oxide layer as shown in Figure 5.23b. To facilitate easy fabrication for metallisation, oxide layers can be deposited on the sides, and at the top of the silicon layer of each MISIM arm (see Figure 5.23b).

In order to couple light effectively from a wide input waveguide into the two nano-slot plasmonic waveguides, an efficient plasmonic coupler is required, otherwise, the proposed modulator may suffer from very large coupling losses. A simple V-shape 1x2 nano-plasmonic splitter was proposed [114], in which the light from a single mode SOI waveguide efficiently couples (via a tapered structure) into two plasmonic slot waveguides. In this case, the splitter length was optimised to about 0.2-0.4μm, with a predicted maximum coupling efficiency of 76%.

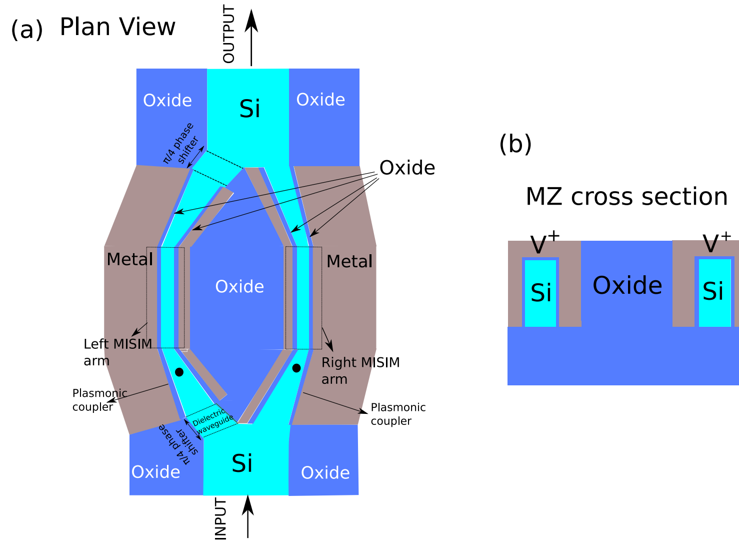

Figure 5.23: (*a*) A schematic plan view of the asymmetric MISIM accumulation mode electro-optic modulator, including the splitter and combiner configurations. (*b*) Cross-sectional view of the the MISIM MZ structure proposed for asymmetric biasing between the two plasmonic arms separated by an oxide layer.

5.4 MISIM electroabsorption device

In contrast to the interference based MZ device which comprises two plasmonic waveguides, an absorption based single MISIM waveguide device was also theoretically investigated using the FEEM. In this device, the absorption coefficient (rather than the real refractive index) of the plasmon mode was varied via an externally applied bias, in order to achieve optical modulation for a particular device length. The motivation for this work was to investigate and compare any performance improvement over the interference-based MZ device. Hereafter, the single waveguide device will be referred as the MISIM electro-absorption (EA) device.

Figure 5.25 shows the cross-sectional view of the MISIM EA device where the silicon layer is surrounded by the metal and oxide layers both at the vertical sides and top of Si region. The metal used in this device was Copper, for which the refractive index at a wavelength of 1.55μm was obtained from Table 2.1. The propagation loss of the

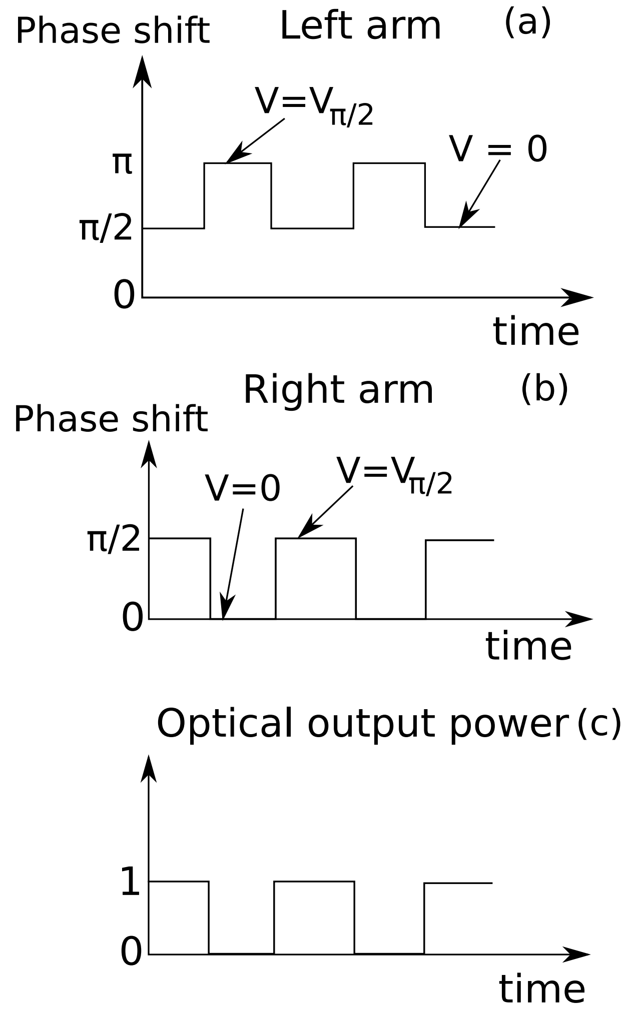

Figure 5.24: Schematic of the proposed asymmetric biasing scheme employed in the left and right arms of the MISIM MZ device. The left arm is assumed to have a built-in phase shift of $\pi/2$ (independent on the bias). $V_{\pi/2}$ represents the voltage required to shift the phase of the optical signal in one arm by $\pi/2$, compared to the unbiased case. The top and middle figures show the graphs for bias applied vs time. The vertical axis of the bottom figure represents the output power (in arbitrary units) due to the constructive or destructive interference between the waves from the two arms of the MZ modulator.

plasmon mode per unit length was determined from the imaginary part κ of the effective mode index, which is related to the absorption coefficient α as: $\alpha = (4\pi/\lambda_0)\kappa$ (where

λ_0 is the free space wavelength). In the absence of an applied bias or the *off* state, a minimum absorption of the plasmon mode occurs, which results in a high transmission at the output of the MISIM EA device. In contrast, the incoming light is attenuated in the *on* state, which leads to a large propagation loss and minimum transmission at the output of the MISIM EA device. Thus a variable transmission in the MISIM EA device can be achieved between the *on* and *off* states. For a particular device length, modulation depth was obtained by calculating the difference in the propagation loss of the plasmon mode between the two states.

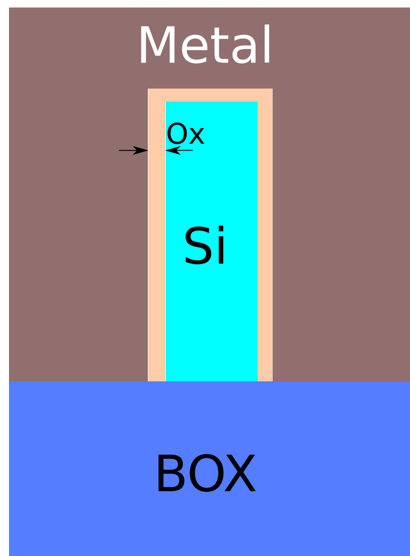

Figure 5.25: Schematic cross section of the MISIM electro-absorption single waveguide device.

As discussed previously in section 5.3.1, QM effects near the oxide-Si interface were included when calculating the electron concentration distribution across the MISIM structure along a line normal to the interface. Also, the accumulation mode operation was considered for an n-type MISIM EA device, in which the silicon layer was n-doped, with the donor density of n= 5x10^{18}cm^{-3}. A positive bias applied to the metal leads to the formation of an ACL near each oxide-Si interface. Figure 5.26a shows the accumulation mode electron concentration distribution across the silicon layer of the MISIM EA device

obtained using Poisson-Schrodinger solver [122]. For a given applied bias, the calculated electron density distribution was used in the Drude model approximation [126] to obtain the n_i distribution across the silicon layer for a given t_{Si}, as shown in Figure 5.26b. This was then imported directly into the FEEM to obtain the change in absorption coefficient of the plasmon mode

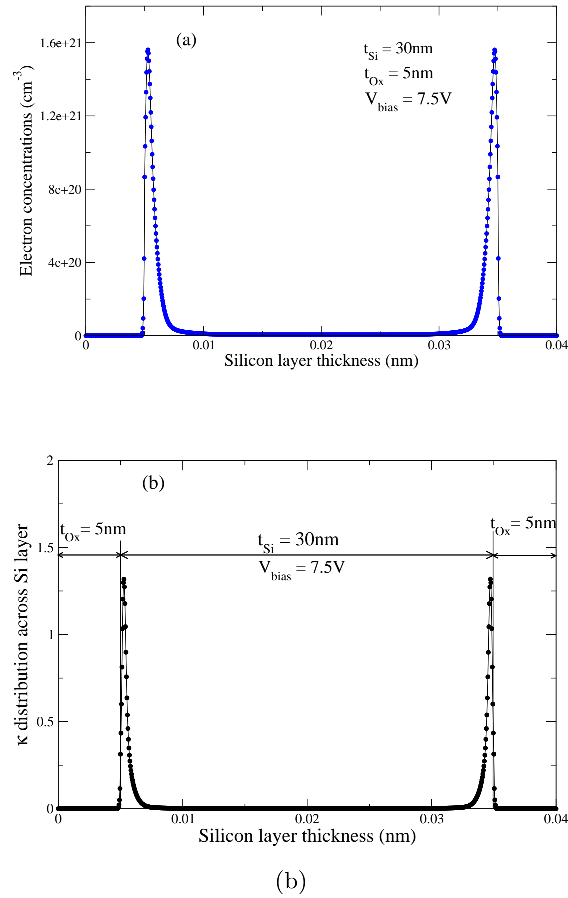

(b)

Figure 5.26: (a). The electron concentration distribution across the Si layer in the MISIM accumulation mode EA device for an applied bias of 7.5V. (b). Distribution of n_i of the silicon refractive index across the Si layer calculated from the Drude model for V_{bias} = 7.5 V.

Figure 5.27 shows the electric field profile across the thin Si layer in the MISIM EA device in the unbiased state. Similar to the result obtained in the sub-section 5.3.2

(Figure 5.15), a strongly confined subwavelength gap plasmon mode was obtained in the low index oxide layer between the metal and semiconductor layers which decays further into the Si region. The dependence of the device performance on the height (H) of the structure was investigated using the FEEM. In this case, the device loss is defined as the propagation loss per unit length (dB/μm) experienced by the plasmon mode within the MISIM EA device in the unbiased state. The insertion loss of the MISIM EA system can then be calculated for a particular device length. Figure 5.28 shows the device loss for different H, with all other physical parameters kept fixed. For smaller values of height ($H < 150$nm), an increased spilling of the plasmon mode from the bottom opening of the structure into the surrounding oxide layer was observed. This leads to poor confinement of the EM mode within the structure, and therefore an increased device loss. In addition, an increased influence of the metal layer at the top of the Si region was observed, which also affected the mode confinement, due to increased absorption by the metal. However, the situation improves for $H > 150$nm, when the EM mode confinement increases. For $H > 450$nm, the plasmon mode is least influenced by the presence of the top metal layer, leading to a negligible increase in the absorption of the mode by the metal, and therefore resulting in saturation of the device loss.

Figure 5.29 shows the effect of varying the oxide layer thickness on the MISIM EA device loss. As discussed earlier in the sub-section 5.3.2, HfO_2 performs better better than SiO_2 as the oxide material. The device loss increases with decreasing t_{ox} because the field intensity of the confined plasmon mode within the thin oxide layer increases, which leads to larger overlap of the plasmon mode with the lossy metal at the sides, and hence, a larger device loss. Although a larger t_{ox} reduces device loss, the modulation depth obtained was negligible. This was because the use of a thick oxide layer leads to a smaller peak electron density near the oxide-Si interface across the MISIM structure for a given bias, which eventually resulted in a smaller change in the absorption coefficient of the plasmon mode. Conversely, the use of thinner oxide layer allows a larger portion of the applied bias to be available across the Si layer, causing larger peak electron density near the oxide-Si interface. This results in a larger change in the absorption coefficient

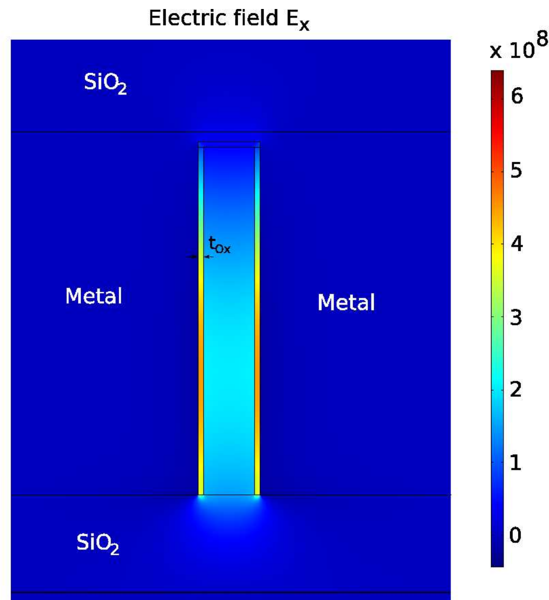

Figure 5.27: Electric field (E_x) profile across the MISIM EA device in the *off* state.

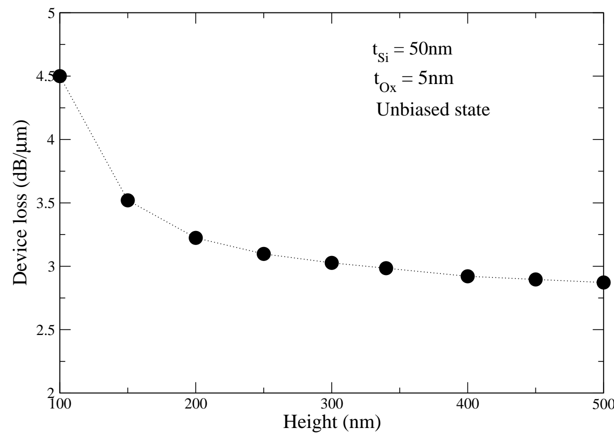

Figure 5.28: Device loss (dB/μm) as a function of H in the MISIM EA device.

of the plasmon mode between the biased and unbiased states, and therefore an increased modulation depth.

Figure 5.30 shows the dependence of the modulation depth and device loss on t_{Si}, obtained using the FEEM with all other parameters kept fixed. The device loss increases with decreasing t_{Si} because of the increasing confinement of the EM mode within the

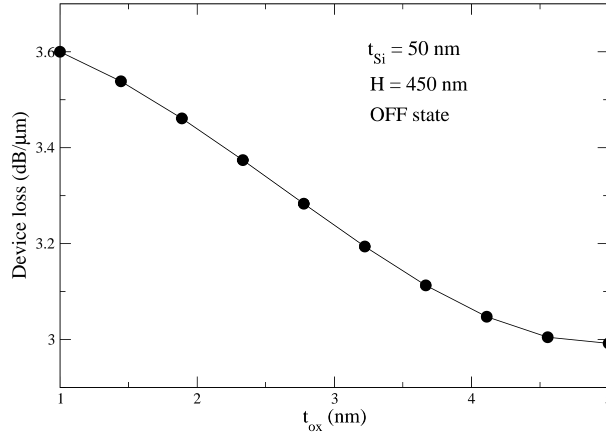

Figure 5.29: Effect of varying t_{ox} on the MISIM EA device performance.

thin oxide layer, which results in absorption of an increased proportion of the mode by the metal layer. When a bias is applied, due to the accumulation of electrons near the oxide-Si interface, the EM mode is pushed closer to the interface. This leads to even larger absorption by the metal, resulting in a further increase in the propagation loss per unit length, and therefore results in an increased modulation depth between the two states with decreasing t_{Si}. Thus a trade off between the modulation depth and device loss with t_{Si} was observed. For an applied bias of 7.5V to a 1μm long device, a modulation depth of 5.1dB and a device loss of 7.11 dB was attained using a 20nm t_{Si} and a 1nm t_{ox}.

A somewhat similar work was also carried out by Shiyang et. al [128] to achieve EA modulation in a plasmonic slot MISIM structure, in which an approximated averaged electron density distribution of 8x10^{20}cm^{-3} was assumed within 1nm of the accumulation layer near the oxide-Si interface for the simulation purpose. However in the work described here, the exact electron density distribution across the Si layer for a given applied bias was imported into the EM model in order to obtain the change in propagation loss per unit length of the plasmon mode in the unbiased and biased states. Nonetheless, Shiyang et. al also carried out experimental work for the same design, which predicted a promising performance of 3dB modulation depth, and 4dB insertion loss for a 3μm long device length for V$_{bias}$=6.5V. Additionally, they used SiO_2 rather than HfO_2. The

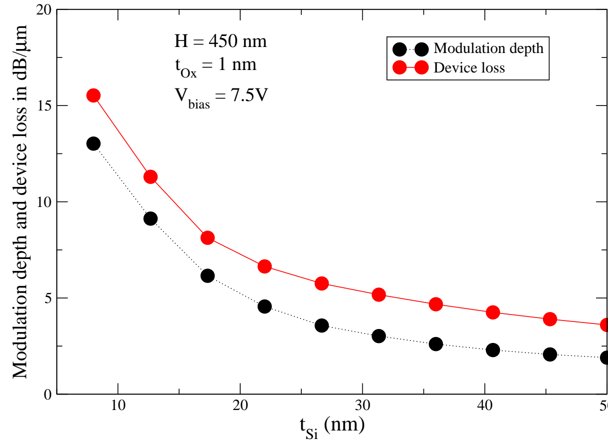

Figure 5.30: Effect of varying t_{Si} on the device loss (dB/μm) in the unbiased state and the modulation depth (dB/μ) loss between the biased and unbiased states.

investigations (described in this chapter and Shiyang et. al) suggest that the use of oxides with large dielectric constant, thinner oxide and optimised narrower silicon layers offer improved system performance with respect to modulation depth and insertion loss.

The theoretical investigations carried out on the MISIM MZ and EA devices indicate that these devices are promising candidates for future plasmonic modulators. Specifically, the MISIM EO MZ modulator is very small in size, with just 0.25-0.5μm device length and predicts an acceptable IL (of only 1-2dB) even without the implementation of the push-pull configuration. On the other hand, the MISIM EA device is quite simple and easy to fabricate compared to the MZ device, but its performance (ER (5dB), IL (7dB), and device length (1μ)) is not as good. Nevertheless, these devices can be efficiently integrated with electronics as they are silicon compatible.

Chapter 6

Silicon-based plasmonic coupling to nano-slot and SOI waveguides

6.1 Introduction: optical transmission in different plasmonic structures

For maximum performance of the electro-optic Mach-Zehnder modulator discussed in the previous chapter, an efficient coupler is required to couple light from a wide fibre grating opening into the nanoscale MISIM plasmonic arms. Plasmonic nanostructures can be used to achieve effective coupling of the incident light by coherently exciting and focusing SPPs as they propagate towards the nanoscale hole or aperture, resulting in a field or transmission enhancement. Such an effect opens up a new possibility of using specially designed silicon-based plasmonic optical couplers to provide the passive front-end in a future plasmonic transceiver system.

An important aspect of the realisation of on-chip integration between nano-electronics and photonics on the same platform is the efficiency with which light from an external fibre grating couples into a silicon-on-insulator (SOI) or nano-plasmonic waveguides on the same chip [129–135]. Excitation of surface plasmons on a patterned metal surface allows light to be focused into subwavelength apertures [136–142], resulting in a large

transmission through a central hole, which would otherwise be too small according to the standard theory. Enhanced optical transmission (EOT) of up to a factor of three was demonstrated experimentally when normally incident light impinged on a bull's eye (BE) structure comprising a single circular aperture on a periodically corrugated silver surface with air above and below the structure [129, 137](see Figure 6.1).

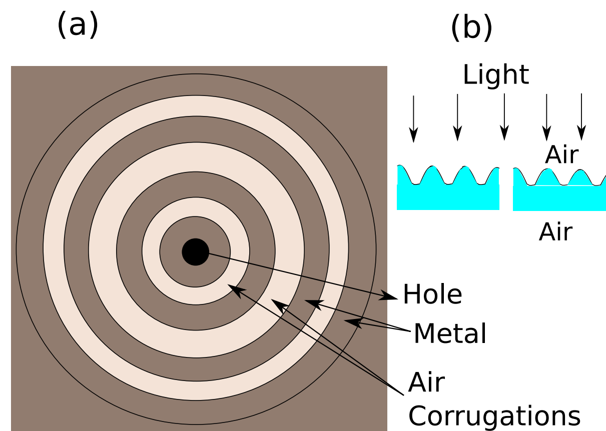

Figure 6.1: (a) Schematic illustration of a bull's eye structure [137] comprising a single subwavelength circular aperture surrounded by periodic corrugated circular grooves. (b) The two dimensional cross sectional view of the BE structure with air above and below a thin metal film.

It has been known from chapter two that since the real part of the surface plasmon wave-vector (k_{SPP}) remains below the light line, SPPs cannot be excited by simply illuminating the surface with freely propagating light. Periodically corrugating the metal surface with circular grooves provides the necessary momentum, leading to a resonance condition which can be determined by the periodicity of the grooves. This enables incident light to couple with the SPPs at the metal surface, which results in a resonant transmission [137, 143, 144]. Even larger transmission enhancement is possible if the output surface surrounding the central hole in the BE structure is corrugated as well; this is known as the double sided BE structure [137, 145, 146]. In this case, the light emerging from the exit of the aperture couples with the periodic corrugations on the exit surface and the existing groove modes, and then interferes with the light directly

incident on the central hole, resulting in a stronger focused beam. Since the discovery of the BE structure, several other structures have been investigated for applications in sensing, imaging, high resolution near-field microscopy, and ultra high density optical data storage [39, 141, 147–151]. In a two dimensional equivalent of the BE configuration, the distance between the central slit and the nearest groove was explored in order to achieve EOT from a normally incident light [139]. The study revealed that, since the phase of the magnetic field of the SPPs was in antiphase with that of the incident field at the centre of a groove, the optimised slit-to-groove distance was approximately half the surface plasmon wavelength. This resulted in an increased magnetic field intensity at the slit entrance, and hence maximum energy transmission.

Recently, a metal antenna structure as shown in Figure 6.2 was investigated theoretically in order to achieve EOT [152]. The structure comprised symmetrically arranged rectangular grooves with air above and below, in which the incident light impinges at an oblique angle to the normal of the surface. The phenomenon of constructive interference between the SPPs excited from adjacent grooves was investigated in order to achieve enhanced energy transmission through the central slit [152, 153]. However, their structure was not CMOS compatible.

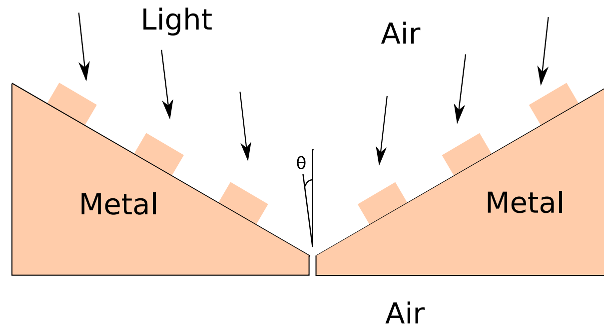

Figure 6.2: Schematic diagram of a rectangular corrugated metal antenna structure.

Here, a silicon-based plasmonic coupling structure is discussed in the following section. It can be used for coupling light from wide fibre grating waveguide openings into silicon-on-insulator (SOI) plasmonic or dielectric waveguides. Furthermore, the struc-

ture was investigated for simultaneous coupling and splitting of light from a wide input opening into two nano-plasmonic slit waveguides.

6.2 Silicon-based metallised grooved plasmonic nano-focusing coupler

Figure 6.3 shows a schematic plan view of the plasmonic nano-focusing structure on a silicon substrate. The structure comprises periodically arranged rectangular grooves, which converge towards a metal-silicon-metal nano slit waveguide at the apex of the structure. The light was projected from the same plane as that of the plasmonic coupler. The light falling on each groove excites SPPs, which constructively interfere as they propagate towards the central nano-slit, thereby achieving an enhanced transmission at the slit entrance.

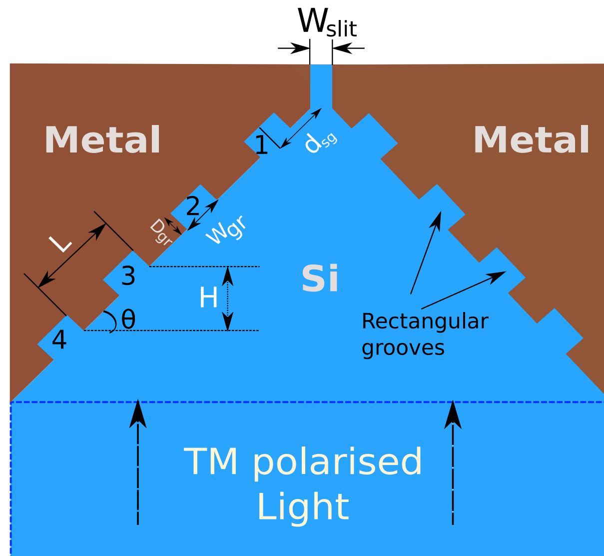

Figure 6.3: Plan view of the symmetrically grooved metallised nano-focusing structure.

The period (L) and angle of the grooves were determined by the requirement that the excited SPPs and the incident light falling on each groove remain in phase [150]. The phase shift (ϕ_{SPP}) of the excited SPPs from one groove (for example, SPPs from

groove number 4 in Figure 6.3) arriving at the next adjacent groove (groove number 3) closer to the slit is given by:

$$\phi_{SPP} = \frac{L}{\lambda_{SPP}} \tag{6.1}$$

where $\lambda_{SPP} = \lambda_0/n_{SPP}$ (λ_0 is the free space wavelength) is the SPP's wavelength at the metal(m)-Si interface, and $n_{SPP} = \sqrt{\frac{\epsilon_{Si}\epsilon_m}{(\epsilon_{Si}+\epsilon_m)}}$. Assuming that the adjacent grooves are separated by a vertical spacing of H (see figure 6.3), the phase of the incident light at groove 2 is given by:

$$\phi_{Si} = 2\pi\frac{H}{\lambda_{Si}} \tag{6.2}$$

where $\lambda_{Si} = \lambda_0/n_{Si}$.

Therefore, in order to achieve constructive interference between the SPPs arriving at the adjacent groove (number 2) and those generated in it, the difference between their phases should be an integer multiple of 2π:

$$\phi_{SPP} - \phi_{Si} = 2m\pi \tag{6.3}$$

where m is an integer. The angle (θ) of the optical path of the propagating SPPs with the horizontal plane of the structure can be expressed as:

$$\theta = \sin^{-1}\frac{\lambda_{Si}}{(N\lambda_{SPP})}$$

where N is an integer. Since the incident wavelength in silicon (λ_{Si}) is slightly larger than λ_{SPP}, $N \geq 2$. N=2 (and not N=3,4..) was therefore chosen because this will allow for a minimum taper length in the structure. Assuming that most metals have dielectric constants with a large negative real part, n_{SPP} and therefore λ_{SPP} tend to remain the same value of $\approx 32°$. This means that the angle θ required to satisfy Eq. 6.3 is almost independent of the choice of metal or dielectric material, and the particular wavelength used. The structure was optimised with respect to the groove depth (D_{gr}), width (W_{gr}), number of grooves (N_{gr}), and slit-to-groove distance (d_{sg}) to achieve maximum power coupling from a wide input opening into the nano-slit. For all the following investigations, the metal used was silver, with a refractive index from Table 2.1.

The power coupling efficiency of incident light from a broad input opening into the 30nm narrow slit was investigated theoretically for different N_{gr}, using a 2D FEEM [73]. Figure 6.4 shows the power coupling efficiency as a function of N_{gr} with all other parameters kept fixed. In each case, the figure shows the maximum simulated power coupling efficiency obtained near the exit of the narrow slit at the apex of the structure for incident wavelengths within the range of 1.538-1.562μm. The coupling efficiency decreases for $N_{gr} > 4$. This is because the SPPs excited from the outermost grooves are mostly absorbed, due to an increasing path length over the metal. This adds to the total loss incurred by the SPPs, which results in a decreasing power coupling efficiency into the slit. However, for N_{gr} <3, a larger power coupling efficiency was obtained. In this case, the structure is short, and therefore the amount of metal used in the structure is reduced. Hence, most of the incoming light couples directly into the slit with minimum absorption by the metal and therefore, the losses are reduced. However, the input aperture width is small, which is disadvantageous for the purpose of coupling light from wide input fibre apertures. For $N_{gr} = 4$, the simulations predicted a maximum power coupling efficiency of $\approx$ 40% for an input aperture width of $\approx$6.1μm. Comparison of the electric field profiles (E_x) for the structures comprising 3 and 4 number of grooves were carried out using the FEEM. Strong lateral resonant modes pinned at the side-walls were obtained within the grooves for N_{gr}=4, which resulted in a stronger transmission coupling into the slit. In contrast for N_{gr}=3, very weak lateral resonances were obtained within the grooves, which resulted in a poor coupling efficiency into the slit. Hence, N_{gr}=4 was used for all the further investigations.

6.3 Two dimensional finite element and transfer matrix models

The dependence of D_{gr} on the power coupling efficiency was investigated using the FEEM. Figure 6.8(a) shows the power coupling efficiency as a function of D_{gr}, with all other parameters kept fixed. For $D_{gr} > 20$nm, an increasing power coupling efficiency

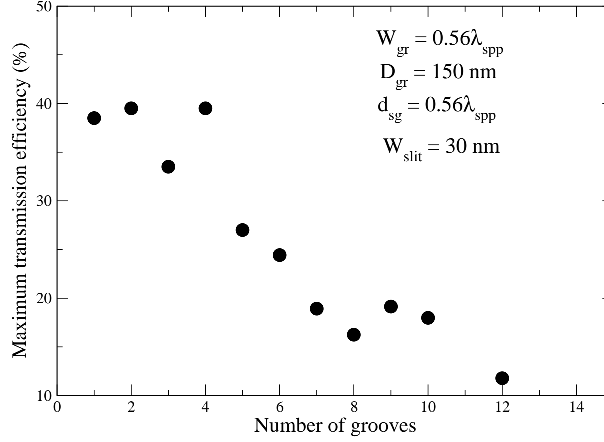

Figure 6.4: Effect of varying the number of grooves of the plasmonic coupler on the coupling efficiency of light from a broad input opening into the narrow slit.

was obtained, with a maximum at D_{gr} = 50nm, beyond which the coupling efficiency decreases, leading to a minimum at D_{gr}= 70nm. The coupling efficiency increases again for $D_{gr} > 70$nm, resulting in a maximum of ≈40% for a broad range of D_{gr} varying from 120-170nm.

To analyse the unusual dependence of groove depth on the coupling performance, a transfer matrix model (TMM) was developed using parameters extracted from the FEEM. An array of n identical grooves were considered, which were separated by a length L and labelled as 1,2,3...n, where the groove 1 was assumed to be nearest to the slit. The array was tilted with respect to the wavefront of the incident light, and the vertical spacing along the propagation direction between the adjacent grooves was assumed to be H (see Figure 6.5). The wave amplitudes from the two sides of the array can be related by a transfer matrix equation, including source terms. For the right hand side of the plasmonic coupler in Figure 6.3, the equation reads:

$$\mathbf{B}_n = (\mathbf{T}_G\mathbf{T}_L)^{n-1}\mathbf{T}_G\mathbf{A}_1 + \sum_{i=1}^{n}(\mathbf{T}_G\mathbf{T}_L)^{n-i}\exp(j(n-i)\phi)\mathbf{C_i} \tag{6.4}$$

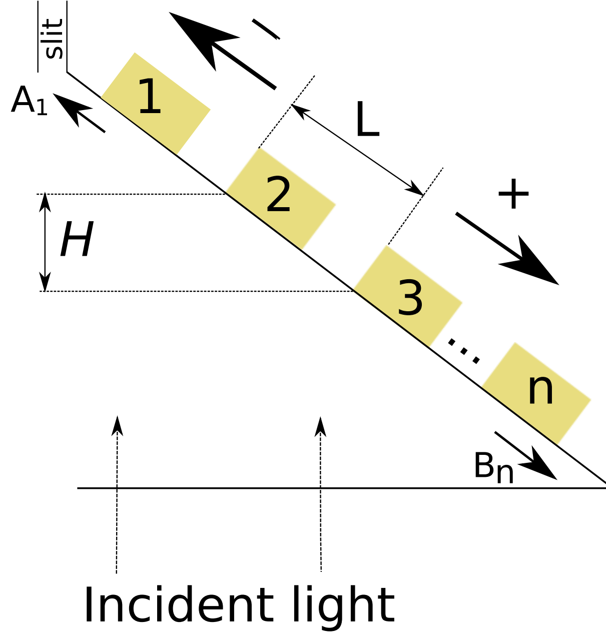

Figure 6.5: Schematic diagram of the right hand side of the plasmonic coupler comprising an array of n grooves.

where

$$\mathbf{A}_1 = \begin{bmatrix} A_1^+ \\ A_1^- \end{bmatrix}, \quad \mathbf{B}_n = \begin{bmatrix} B_n^+ \\ B_n^- \end{bmatrix}, \quad \mathbf{C_i} = \begin{bmatrix} C_i^B - rC_i^F/t \\ -C_i^F/t \end{bmatrix} \tag{6.5}$$

$\mathbf{A_1}$ and $\mathbf{B_n}$ are the wave amplitudes on the left and right of the array respectively, with + and − denoting waves travelling to the right or left (Figure 6.5); C_i^F and C_i^B are the amplitudes of the plasmons travelling in a forward and backward direction (see Figure 6.7), excited in a groove by an obliquely incident light beam. The subscript i allows different grooves to generate different amplitudes of plasmon waves because the incident light intensity may vary across the array according to the form of the TM mode assumed at the input. Furthermore,

$$\mathbf{T}_G = \begin{bmatrix} t - r^2/t & r/t \\ -r/t & 1/t \end{bmatrix}, \quad \mathbf{T}_L = \begin{bmatrix} \exp(j\gamma_{SPP}L) & 0 \\ 0 & \exp(-j\gamma_{SPP}L) \end{bmatrix} \tag{6.6}$$

are the transfer matrices, which relate the plasmon waves of the groove and flat

metal path length L. r and t are the complex coefficients denoting the amplitude of the plasmon reflection and transmission coefficients including the phase shift, while γ and

$$\gamma_{SPP} = \frac{2\pi}{\lambda_0}\sqrt{\frac{\epsilon_{Si}\epsilon_m}{\epsilon_{Si}+\epsilon_m}} \tag{6.7}$$

are the propagation constants of light and plasmons in Si, and may also be complex to allow for losses. $\phi=\gamma$H is the phase lag in plasmons excited in adjacent grooves.

In these equations, a groove was considered as a point-like scatterer, and is generally lossy: i.e. an incident plasmon may scatter into free light or be partially absorbed, rather than only being transmitted or reflected, which implies that $|t|^2+|r|^2<1$. In this approximate formulation, the scattered radiation is counted as lost and assumed not to return into the system. Equation 6.4 can be written as:

$$\begin{bmatrix} B_n^+ \\ B_n^- \end{bmatrix} = \begin{bmatrix} T_{11} & T_{12} \\ T_{21} & T_{22} \end{bmatrix} \begin{bmatrix} A_1^+ \\ A_1^- \end{bmatrix} + \begin{bmatrix} S^+ \\ S^- \end{bmatrix} \tag{6.8}$$

where S^{+-} are the collection of the source terms given by the sum in Eq. (6.4). In the system described above, it was assumed that there were no incoming plasmons to the array, which means that $A_1^+=0$ and $B_n^-=0$. Hence, solving equation (6.8) results in outgoing plasmon amplitudes which travel towards the slit (A_1^-) and away from the slit (B_N^+):

$$A_1^- = -\frac{S^-}{T_{22}}, \qquad B_n^+ = S^+ - \frac{T_{12}S^-}{T_{22}} \tag{6.9}$$

where the A_1^- component carries energy towards the slit. The magnitudes of the transmission ($|t|$) and reflection coefficients ($|r|$) used in the TMM were determined from FEEM simulations of a single groove structure as shown in Figure 6.6. An in-plane SPP field launched towards the groove from the left hand side of the structure was assumed, which can be obtained as described below.

The x and y components of the electric field of the TM EM wave for $y>0$ are given as [61]:

$$E_{x2}(y) = iA_2 \frac{k_2 e^{i\gamma x} e^{-k_2 y}}{\omega \epsilon_0 \epsilon_2}, \quad (6.10)$$

$$E_{y2}(y) = -A_2 \frac{\gamma}{\omega \epsilon_0 \epsilon_2} e^{i\gamma x} e^{-k_2 y} \quad (6.11)$$

and for $Y < 0$

$$E_{x1}(y) = -iA_1 \frac{k_1 e^{i\gamma x} e^{k_1 y}}{\omega \epsilon_0 \epsilon_1}, \quad (6.12)$$

$$E_{y1}(y) = -A_1 \frac{\gamma}{\omega \epsilon_0 \epsilon_1} e^{i\gamma x} e^{k_1 y} \quad (6.13)$$

where k_1,ϵ_1 and k_2, ϵ_2 are the wavevectors and permittivities in the two media as depicted in Figure 6.6. At $x = 0$, assuming $A_1 = A_2 = 1$ [61], the above equations reduce to:

$$E_{x2}(y) = i \frac{k_2 e^{-k_2 y}}{\omega \epsilon_0 \epsilon_2}, \quad (6.14)$$

$$E_{y2}(y) = -\frac{\gamma}{\omega \epsilon_0 \epsilon_2} e^{-k_2 y} \quad (6.15)$$

for $y > 0$, and

$$E_{x1}(y) = -i \frac{k_1 e^{k_1 y}}{\omega \epsilon_0 \epsilon_1}, \quad (6.16)$$

$$E_{y1}(y) = -\frac{\gamma}{\omega \epsilon_0 \epsilon_1} e^{k_1 y} \quad (6.17)$$

for $y < 0$. The surface plasmon electric field ($E_x(y)$) decays exponentially in the Si layer (for $y > 0$) and also in metal (for $y < 0$). Therefore, the total SPP electric field ($E_x(y)$, $E_y(y)$) launched towards the in-plane Si-metal structure containing a single groove within the two media can be assumed to be:

$$E_x(y)(V/m) = E_{x1}(y)\Big[\frac{1 + \tanh(y/(10^{-3}\mu m))}{2}\Big] + E_{x2}(y)\Big[\frac{1 - \tanh(y/(10^{-3}\mu m))}{2}\Big] \quad (6.18)$$

$$E_y(y)(V/m) = E_{y1}(y)\Big[\frac{1 + \tanh(y/(10^{-3}\mu m))}{2}\Big] + E_{y2}(y)\Big[\frac{1 - \tanh(y/(10^{-3}\mu m))}{2}\Big] \quad (6.19)$$

because the FEEM simulator requires a single expression for a field component. The use of the numerical value ($10^{-3}\mu$m) in the above expression results in zero or unity values of tanh for any non-zero y, so that for positive or negative values of y, $E_x(y)$ reduces to only $E_{x1}(y)$ or $E_{x2}(y)$, respectively. A similar expression was obtained for $E_y(y)$ as shown in equation 6.19. These expressions were then used as the input port conditions to launch SPPs towards the Si-metal structure in the FEEM in order to obtain t and r.

At a distance L_2 from the groove, t is given by :

$$t = \sqrt{\frac{P_{L2}e^{2Im(\gamma_{SPP})k_0L_2}}{P_{IN}e^{(-2)Im(\gamma_{SPP})k_0L_1}}} \tag{6.20}$$

where P_{IN} is the incident power, k_0 is the wavevector of the light in free space, and P_{L2} is the transmitted SPP power obtained at a distance L_2 on the right hand side of the groove (see Figure 6.6). The denominator of the above equation shows the proportion of P_{IN} at the groove. Similarly, the reflection amplitude (r) is given by:

$$r = \sqrt{\frac{P_{IN} - P_{L1}}{e^{(-4)Im(\gamma_{SPP})k_0L_1}}} \tag{6.21}$$

where P_{L1} is the reflected SPP power obtained at a distance of L_1 on the left hand side of the groove.

Figure 6.8(b) shows the resulting transmission and reflection amplitudes as a function of D_{gr}. The simulations were also used to determine the change in phase experienced by a SPP transmitted or reflected by a single groove for varying D_{gr} as shown in Figure 6.8(c). For each groove depth, the change in phase was calculated by determining the difference in the position of a field maximum in the FEEM of the Si-metal structure with and without grooves, from a fixed point near the input. The phase shift induced by transmission across the groove remains approximately constant for $D_{gr} > 70$nm.

The efficiency with which a single groove excites surface plasmons from illumination by light incident at an angle of 32° to the horizontal plane of the Si-metal structure (as shown in Figure 6.7) was also obtained using the FEEM. The excitation efficiencies of the

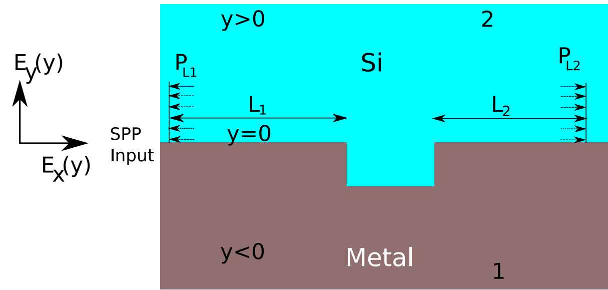

Figure 6.6: A planar Si-metal structure comprising a single groove illuminated by an in-plane SPP field launched from the left hand side.

surface plasmon polaritons propagating forwards and backwards relative to the direction of the incident light were obtained by sampling the field at a large distance from the groove. Any contributions due to the incident field were eliminated by subtracting the field amplitude obtained in the absence of the groove from the original sampled field amplitude. Figure 6.8(d) shows the forward and backward propagating surface plasmon amplitudes for varying D_{gr}.

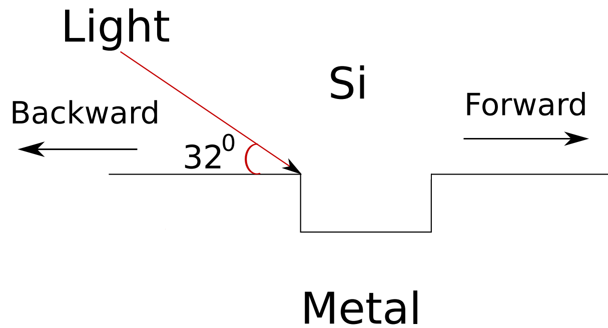

Figure 6.7: A planar Si-metal structure containing a single groove.

The overall results obtained from the TMM are shown in Figure 6.8(a) for different values of D_{gr}. The agreement between the results obtained from the TMM and FEEM is largely qualitative, rather than quantitative. This is because the approximate TMM does not include effects such as the efficiency with which the surface plasmons generated by the adjacent grooves couple into the narrow slit, scattering of light by grooves on one side of the structure across to grooves on the other side, or coupling of scattered light

back into surface plasmons. The TMM mainly aids in understanding of the origin of the peaks of the power coupling behaviour with respect to different D_{gr}.

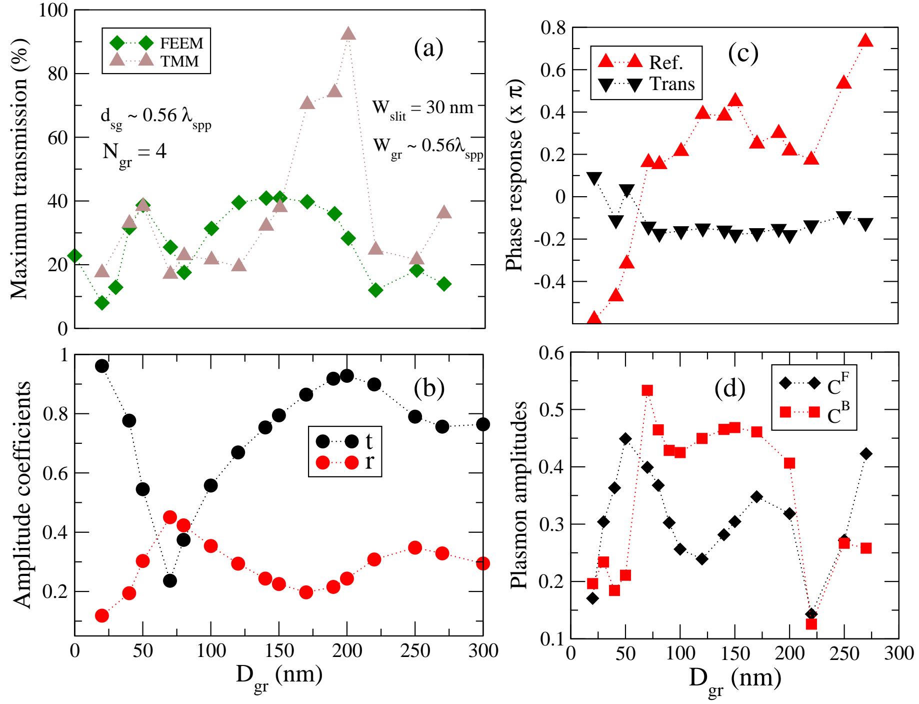

Figure 6.8: (a) Maximum power coupling efficiency obtained in the narrow silicon slit at the apex of the structure for different D_{gr} using the FEEM (green diamonds) and the TMM (brown triangles). (b) Transmission and reflection coefficients obtained for different D_{gr} from a planar metal-Si structure containing a single groove and using SPPs as the input source. (c) SPP transmission and reflection phase shifts for different D_{gr}. (d) Excitation efficiencies of the SPPs at a single Si-metal groove structure propagating forwards (C^F) and backwards (C^B) when illuminated from an incident light falling at an angle to the groove.

The maximum in the power coupling efficiency obtained at D_{gr}= 50nm agrees with that obtained from the FEEM result. The TMM indicates that this is due to the maximum in the forward propagating plasmon excitation efficiency by each groove and the minimum in the backward propagating plasmon excitation efficiency (Figure 6.8d). The FEEM result predicted a minimum in the coupling efficiency at D_{gr}=70nm. The results

from the TMM show that this was due to: (i) a minimum in the transmission coefficient (and a maximum in the reflection coefficient) (Figure 6.8b), and (ii) a maximum in the excitation efficiency of the backward-propagating SPPs (Figure 6.8d).

The dependence of the transmission coupling performance on D_{gr} was investigated further by simulation of the electric field profiles which occur when an SPP mode passes across a single Si-metal groove structure. The interaction of the field with the leading edge of the groove increases with D_{gr}, which leads to increased scattering and reflection (Figure 6.9), therefore results in a minimum coupling efficiency at D_{gr}=70nm (Figure 6.8a). The scattering effect attenuates as the groove depth is further increased and the SPP mode becomes progressively less perturbed by the groove (Figure 6.9b): this leads to an increasing coupling efficiency with a maximum at D_{gr}=200nm.

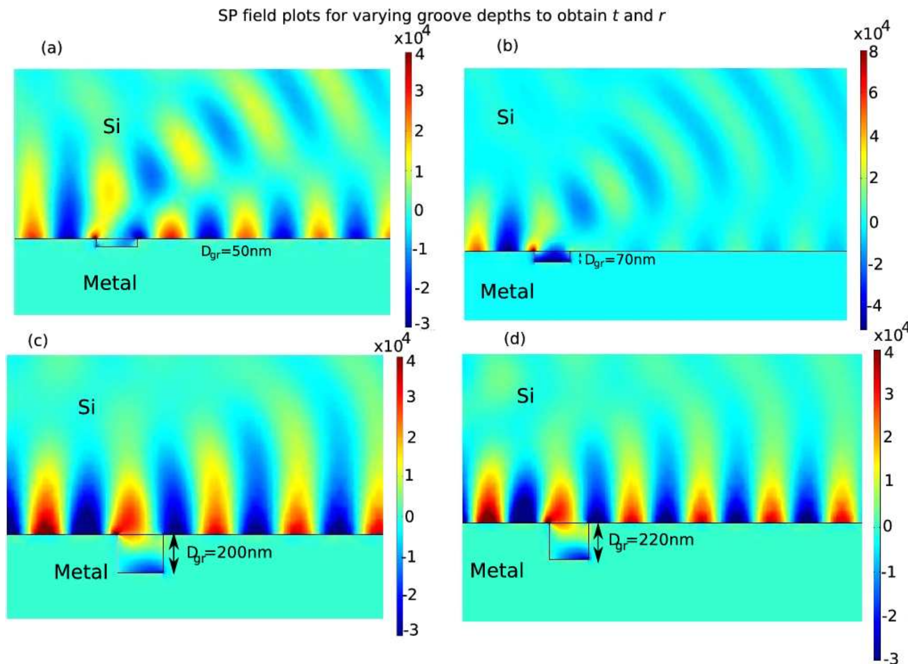

Figure 6.9: Variation in the surface plasmon electric field profile (E_y) in a planar Si-metal structure for groove depths ranging from 70nm to 220nm with W_{gr}= $0.56\lambda_{SPP}$, obtained using the FEEM.

Groove depths in this range are approximately half the surface plasmon wavelength,

which is why they appear to support a first-order vertical resonant mode. However, the resonance exhibited by the groove has a very low selectivity, due to the relatively large width of the groove. The phase difference between the SPPs transmitted directly across and those coming out of the groove is determined by the geometry of the grooves. If the groove profile is designed such that these SPPs are equal in magnitude but out of phase, then almost negligible transmission and maximum reflection can be achieved [154]. Figure 6.10 shows the schematic of an in-plane Si-metal structure containing a single groove with SPP field launched from the left hand side of the structure.

The reflection/transmission variation with the groove depth can be understood from a simple consideration, as follows. Assuming a half the SPP wavelength ($\lambda_{SPP}/2$) propagation down the groove (with the accumulated phase ϕ_{in}), and the same amount after reflection (with the additional accumulated phase $\phi_{in} = \phi_{out}$), the phase change incurred by this EM wave in a round trip within the groove is one plasmon wavelength, which corresponds to a phase shift of 2π. Additionally, the reflection of the plasmons at the bottom of the groove introduces a π phase shift, and therefore the total phase shift amounts to: $\phi_{tot}= \phi_{in}+ \phi_{out}+\pi= 3\pi$. This results in destructive interference with the wave that came across the groove and therefore a minimum transmission (or good reflection). Similarly, a propagation length of $3\times\lambda_{SPP}/4$ down (and up) the groove would result in maximum transmission (low reflection). The study carried out in the chapter three on metallised stub modulator has shown that the groove metallurgical length (L) is not equal to, but is, in fact, smaller than the EM length by $\triangle$l= 0.13μm. With λ_{SPP}=0.424μm, this gives the metallurgical length L=0.08μm (groove depth) for which maximum reflection should occur, rather close to $D_{gr} \approx$ 70nm in Figure 6.8(b), while the minimum reflection would require L= 190nm, again in good agreement with the results in Figure 6.8(b).

A minimum in the coupling efficiency at D_{gr}=220nm in the FEEM was also obtained. The TMM result indicated that this was due to the minimum in the excitation efficiency of the forward propagating plasmons (Figure 6.8(d)). A very weak lateral resonance at D_{gr}=220nm was obtained compared to the strong lateral SPP resonances obtained

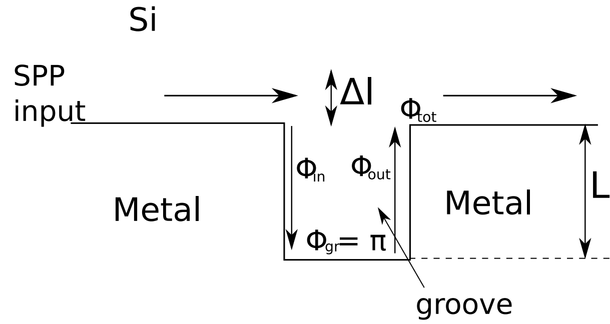

Figure 6.10: Schematic representation of the groove in an in-plane Si-metal structure.

within the groove for D_{gr}=200nm and 250nm, which resulted in a minimum excitation efficiency in both the forward and backward propagating SPP waves. In contrast, the transmission and reflection are far less sensitive to the precise value of D_{gr}.

6.4 Optimisation of the coupling efficiency for varying physical parameters

The effect of varying W_{gr} on the power coupling efficiency of the plasmonic coupler was investigated using the FEEM. Figure 6.11 shows the simulated power coupling efficiency dependence on W_{gr} with all the other parameters kept fixed. The figure shows multiple peaks in the coupling efficiency for different W_{gr}. Figure 6.12 shows the x-component of the electric field profile (E_x) of the plasmonic coupler at W_{gr}=0.56λ_{SPP}. Strong lateral SPP resonant modes pinned at the sidewalls of the Si-metal interface within the first and third grooves (from the slit) were obtained, while weaker resonances occur within the second and fourth groove. The simulated results predict a maximum coupling efficiency of ≈60% for a broad range of W_{gr}, varying from 0.5-0.6λ_{SPP}, in accordance with the range required to achieve EOT in a 2D BE structure [39]. However, the other transmission peaks at W_{gr}=0.35 and 0.8λ_{SPP} are not the result of the individual groove resonances but occur due to the optimum collective behaviour of the 2x4 rectangular groove array.

Figures 6.13a and 6.13b show magnified views of the electric field profiles (E_y) at

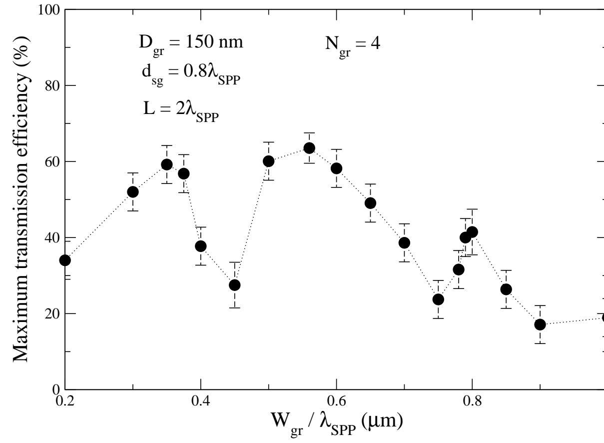

Figure 6.11: Power coupling efficiency into the slit as a function of W_{gr}.

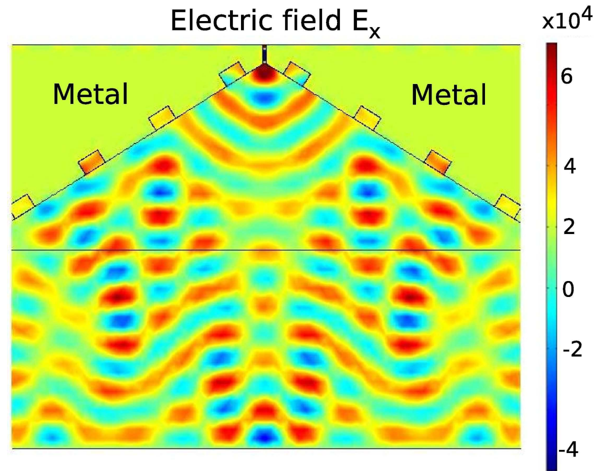

Figure 6.12: Simulated electric field profile (E_x) of the plasmonic coupler for D_{gr}= 150nm and $W_{gr} \approx 0.56\lambda_{SPP}$.

W_{gr}=0.35and 0.45λ_{SPP}, which correspond to the first maximum and minimum in the coupling performance in Figure 6.11. It was observed from these figures that the SPP field intensity within the groove nearest to the slit can influence the coupling efficiency of the whole system. Strong absorption of the SPP electric field within the groove occurs at W_{gr}=0.45λ_{SPP}, which degrades the SPP coupling into the slit, resulting in a reduced overall power coupling efficiency (Figure 6.11). However, at W_{gr}= 0.35λ_{SPP}, the SPP

propagation is least influenced by the presence of the groove, resulting in an increased power coupling efficiency. Similar behaviour of the SPP field within the groove was observed for W_{gr}= 0.75 and $0.8\lambda_{SPP}$, where a stronger lateral electric field intensity (E_x) was obtained in the former than the latter case (Figures 6.13c, 6.13d), resulting in a larger coupling efficiency for W_{gr}=$0.8\lambda_{SPP}$.

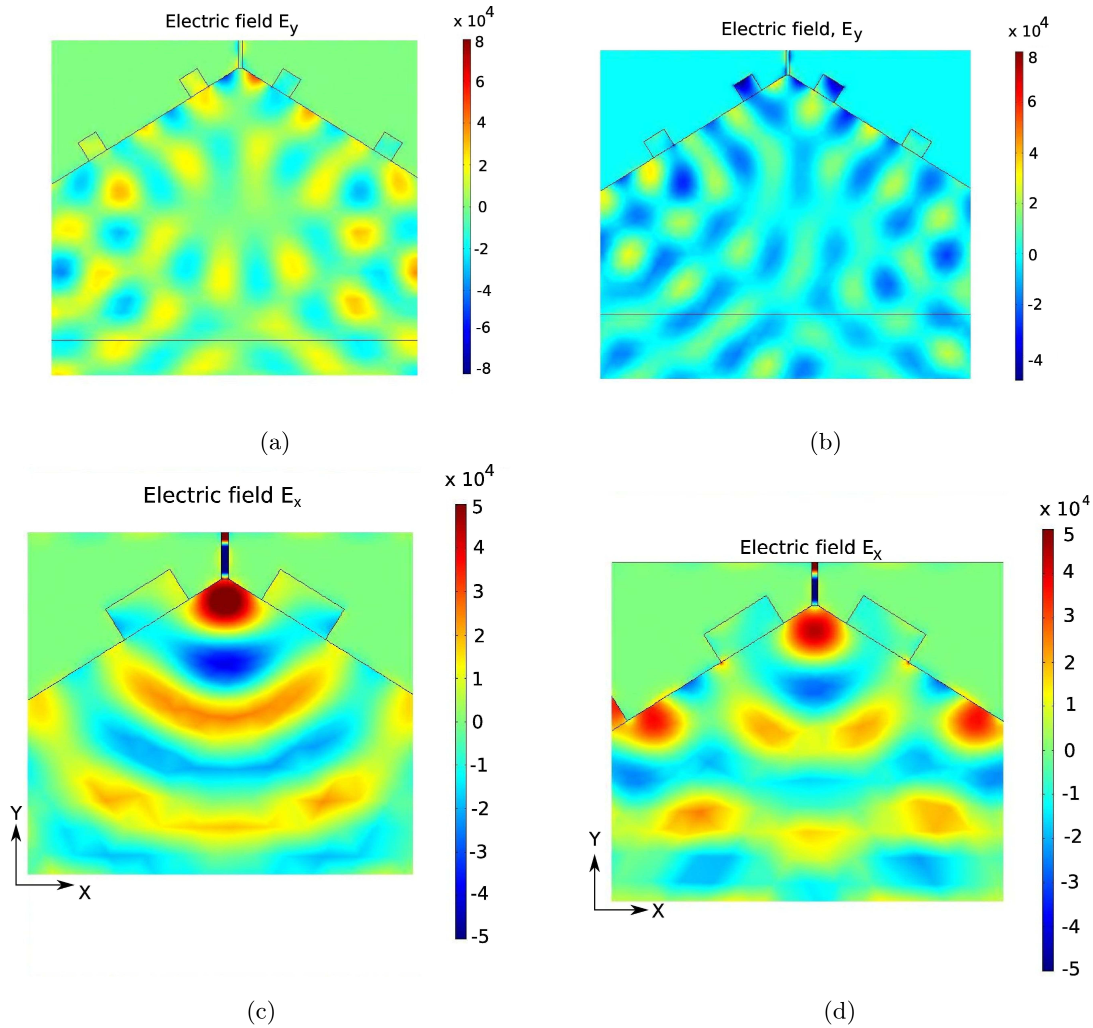

(a)

(b)

(c)

(d)

Figure 6.13: Magnified view of the electric field (E_y,E_x) profiles for: (a) $W_{gr} \approx 0.35\lambda_{spp}$, ($b$) $W_{gr} \approx 0.45\lambda_{spp}$, ($c$) $W_{gr} \approx 0.75\lambda_{spp}$ and (d) $W_{gr} \approx 0.8\lambda_{spp}$

The distance between the centres of the slit and the nearest groove was optimised so that plasmons arriving at the slit entrance from the two sides of the corrugated structure

interfere constructively with those excited by the incident light impinging directly on the effective aperture which encompasses the slit and angled metal side-walls at the apex of the coupler. The effective aperture characterises how much of the incident power is captured by it which could be useful for coupling light into the slit. Figure 6.14 shows the simulated power coupling efficiencies for varying slit-to-groove distance (d_{sg}), with all other parameters kept fixed.

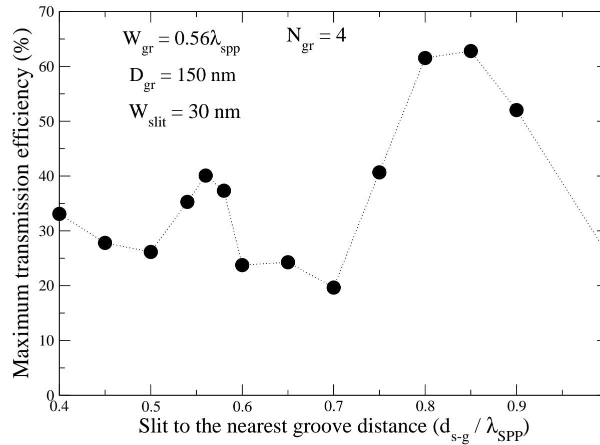

Figure 6.14: Effect of the varying slit to nearest groove distance (d_{sg}) on the maximum power coupling efficiency.

In a 2D BE structure, d_{sg} of $\approx 0.54\lambda_{SPP}$ was predicted to yield maximum EOT from normally incident light. This path length satisfies the difference in the phase shifts introduced when the incident light generates plasmons (i) at a groove and (ii) the slit, and the phase shift introduced when the plasmons arriving from the two sides of the plasmonic coupler are coupled into the perpendicular slit (see Figure 6.15a). However, in this case the central slit is tilted at an angle to the normal to the metal-Si interface (Figure 6.15b), and therefore the phase shift introduced when the propagating plasmons from the groove array couple into the tilted slit should be modified. Electromagnetic simulations were carried out for both cases in order to determine the difference in phase shifts for plasmons coupling into a perpendicular, relative to a 32° tilted slit, and this was calculated to be $\approx 0.7\pi$. Therefore, an optimum coupling efficiency at $d_{sg} \approx (0.7/2)\lambda_{SPP}$

was expected. This agrees well with the FEEM result, where a maximum power coupling efficiency of ≈63% was attained at d_{sg}≈$0.85\lambda_{SPP}$. This value also agrees approximately with the optimum d_{sg}=0.95π, obtained in the symmetrically arranged metal antenna structure (Figure 6.2) illuminated by an obliquely incident light [153].

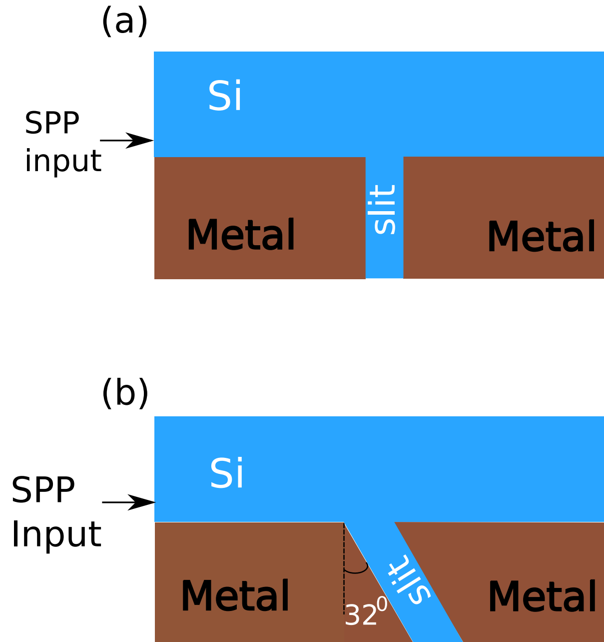

Figure 6.15: Schematic diagram of (a) a perpendicular slit in the case of a 2D BE structure and (b) a tilted slit in the plasmonic coupler.

Using the optimised plasmonic coupler, the width of the slit (W_{sl}) at the apex of the optimised plasmonic coupler was varied between 20-300nm, and the coupling efficiency of light into the slit was obtained using the FEEM. Figure 6.16 shows the simulated coupling efficiency as a function of W_{sl} with all other parameters fixed. Figures 6.17a and 6.17b shows the magnified view of the simulated E_x profiles at W_{sl}= 20nm and 300nm. For a deep subwavelength slit (W_{Sl} <30nm), the SPP mode at the metal-dielectric interface superposes with the incident dielectric mode near the vicinity of the slit entrance, which aids in an efficient conversion of the SPP mode supported by the slit (Figure 6.17a), resulting in a maximum coupling efficiency of 72% for W_{Sl}=20nm.

In addition, the SPP field intensity appeared to be least affected by the presence of the

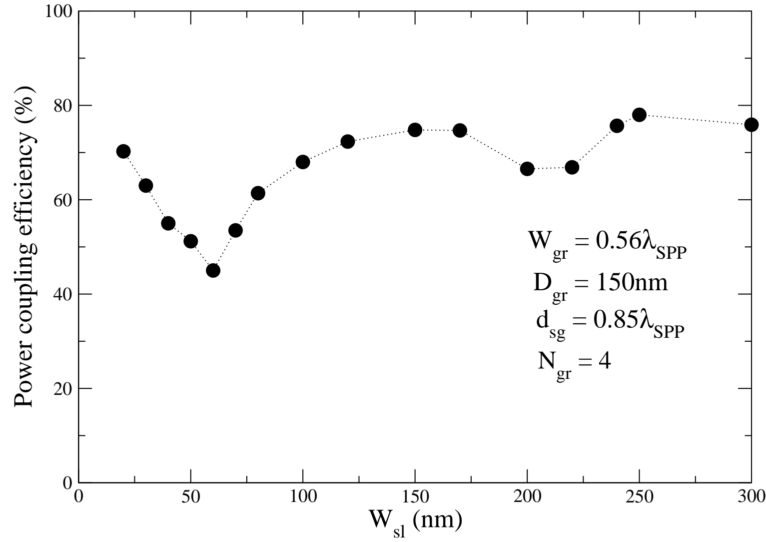

Figure 6.16: Simulated power coupling efficiency for different W_{sl}.

grooves on either side of the geometry, which in turn aids in an efficient SPP propagation, and therefore leads to an enhanced coupling into the slit. However, the above phenomena decreases on further increasing W_{Sl} up to 60nm, beyond which the coupling efficiency increases again (Figure 6.16). For $W_{sl} > 150$nm, strong lateral SPP resonant modes are pinned at the side walls within the groove nearest to the slit (see Figure 6.17b), while nearly negligible absorption of the SPP propagation occurs by the other grooves, which results in large coupling efficiencies in the range of 66-75% (Figure 6.16).

6.5 Applications to SOI waveguide coupling and plasmon mode splitting

In this section, the efficiency with which incident light from a broad input opening couples into SOI plasmonic and dielectric waveguides was investigated using the FEEM. The two main coupling configurations that are widely used for this purpose are an end-fire and an out-of-plane schemes [155, 156]. Recent experimental demonstration have shown the use of an 8μm wide, 50μm long, inverted taper coupler for end-fire coupling of the fibre to an SOI waveguide, which predicted a fibre to silicon waveguide including taper losses

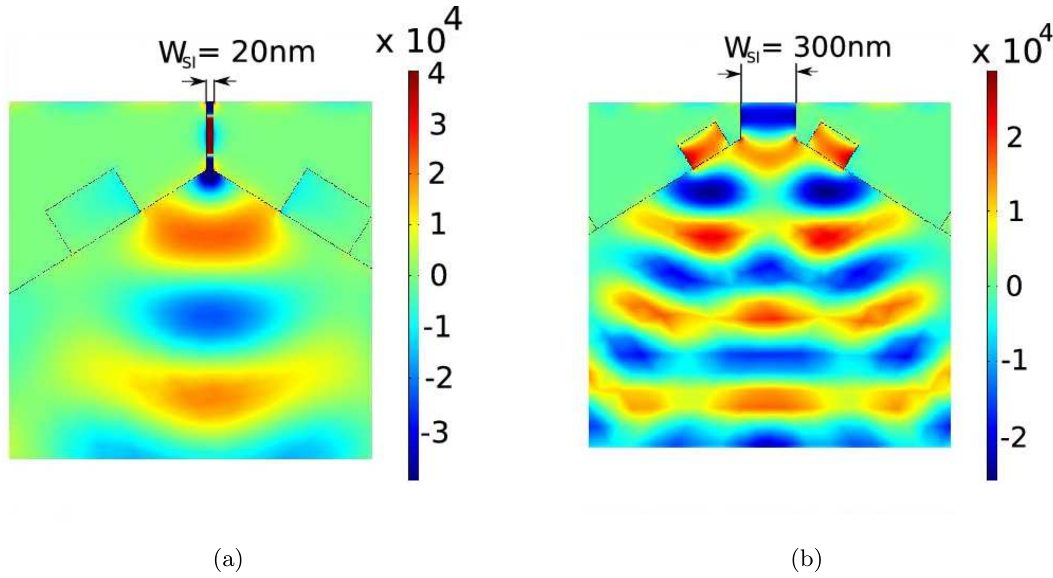

(a)

(b)

Figure 6.17: Magnified view of the simulated electric field (E_x) profiles of light coupling into: (a) a 20nm and (b) a 300nm wide slit.

of ≈12 dB [157]. For an out-of-plane fibre grating coupler, the measured coupling loss from a standard fibre to a single mode SOI waveguide was 5.2dB, using a 50μm taper length [158].

Keeping W_{sl}= 300nm, the prospects of using the optimised plasmonic coupler for coupling light from a wide input fibre grating opening directly into a 300nm SOI waveguide were investigated, using the FEEM. Figure 6.18 shows the simulated electric field profile (E_x) of the tapered plasmonic coupler. Pinned SPP modes were obtained at the vertical side-walls of the metal-Si-metal plasmonic waveguide at the apex of the coupler, where the maximum field intensity was obtained at the metal-Si interface (see Figure 6.19). These SPP modes are efficiently converted into an SOI dielectric waveguide mode with the maximum field intensity located at the centre of the silicon waveguide. The FEEM predicted maximum power coupling efficiency of ≈63% and 61.5% in plasmonic couplers comprising 4 and 7 number of grooves respectively, which correspond to input opening widths of 6.4μm and 10.4μm. The taper lengths of these structures are only 1.9μm and 3.15μm. A typical single mode optical fibre has a core diameter of ≈10 μm for 1.55 μm

wavelength operation [159]. This means that the plasmonic coupler can be employed for coupling light from a fibre grating coupler directly into a nano-plasmonic waveguide with 1.3dB insertion loss or into a single mode SOI waveguide with 2.1 dB insertion loss. In recent works on plasmonic coupling, a dielectric slab waveguide (width 300nm) placed adjacent to an MDM nano-slot waveguide (≈50nm wide) theoretically predicted a coupling efficiency of 70%, however their input opening width is much smaller than that of the plasmonic coupler discussed here [160]. In another situation, a tapered photonic SOI to plasmonic waveguide coupling structure numerically predicted a coupling efficiency of 50%, in which the structure comprises an SOI waveguide vertically side coupled to a gold strip [161].

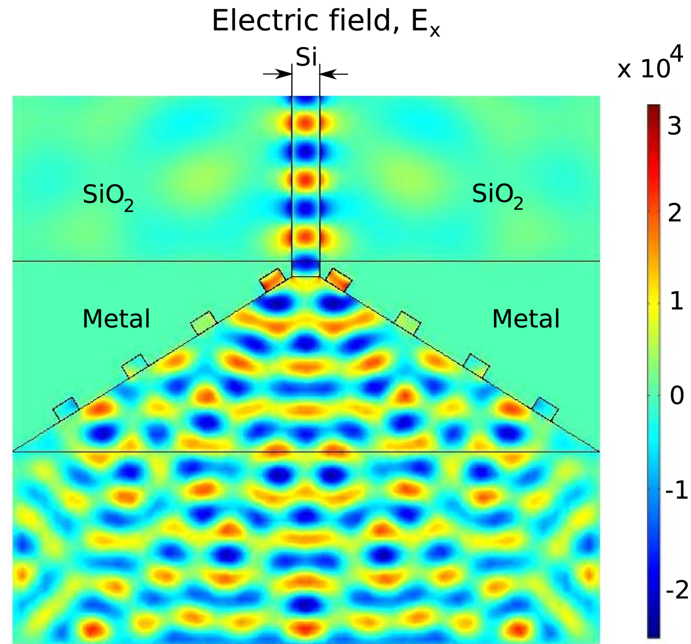

Figure 6.18: Simulated electric field distribution (E_x) of the plasmonic tapered structure used for coupling light from a ≈6.2μm wide input opening into an 300nm SOI dielectric waveguide.

Finally, the performance of the coupler as a plasmonic splitter was investigated using the FEEM: in this case the coupler simultaneously splits and couples light from a broad

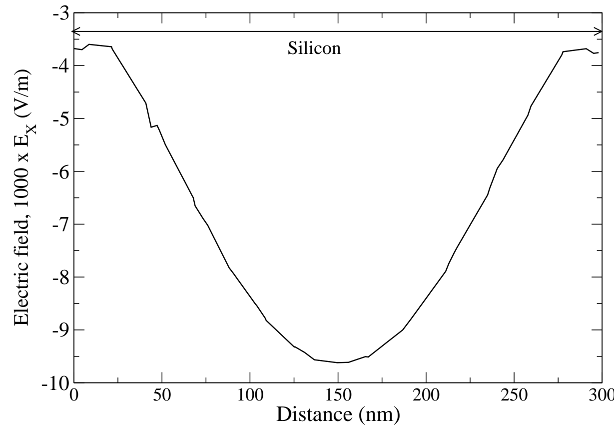

Figure 6.19: Simulated electric field profile (E_x) along the line normal to the metal-Si interface across the 300nm wide metal-Si-metal plasmonic waveguide at the apex of the coupler.

input opening equally into two nano-plasmonic SOI waveguides at its apex. The width of each slit was kept at 50nm, and they were separated by a metal gap region. Figure 6.20 shows the magnified view of the E_x profile of the simulated plasmonic splitter. The metal gap width (W_{gap}) was varied, and the efficiency with which the light couples into each 50 nm plasmonic slit was obtained with all other parameters kept fixed. Figure 6.21 shows the dependence of the power coupling efficiency on W_{gap}. Since the optical path length of the SPPs travelled along one side of the coupler is different upon arrival at the entrance of the two slits, the condition for achieving maximum constructive interference between the SPPs at the slit entrance degrades with increasing W_{gap}. The total SPP intensity is proportional to the square of the cosine of the phase difference, which is why it is not very sensitive to the very small values of W_{gap}, but sensitivity increases for larger value of W_{gap}. Furthermore, absorption of the pinned SPP modes by metal increases with increasing W_{gap}: however, this has a small effect on the overall coupling performance of the system.

The proposed plasmonic splitter could be employed for splitting light from an optical carrier directly into two input arms of the Mach-Zehnder plasmonic modulator: for example the one described in the previous chapter, in which case the MZ structure can

be modified such that only the output arms need to be asymmetric [162]. In another similar application, the above designed plasmonic splitter could also be used for coupling light from a broad fibre grating opening directly into the two nano plasmonic arms of the metal-oxide-semiconductor-metal MZ modulator proposed by Shiyang et. al [114].

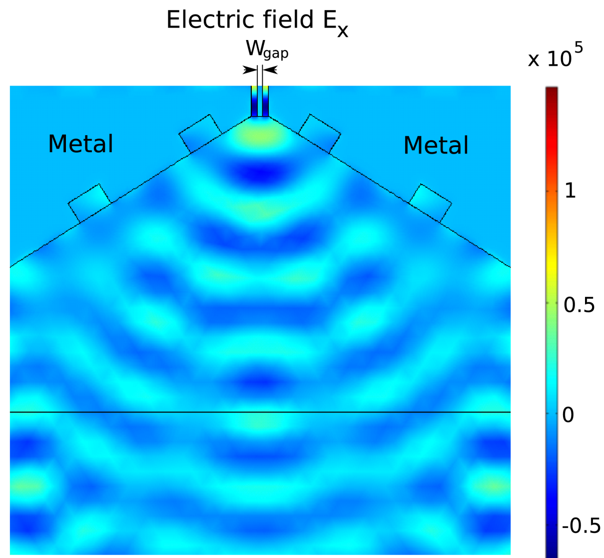

Figure 6.20: E_x profile of the simulated structure where the light from a broad input opening simultaneously couple and splits into each nano plasmonic waveguide situated at the apex of the structure.

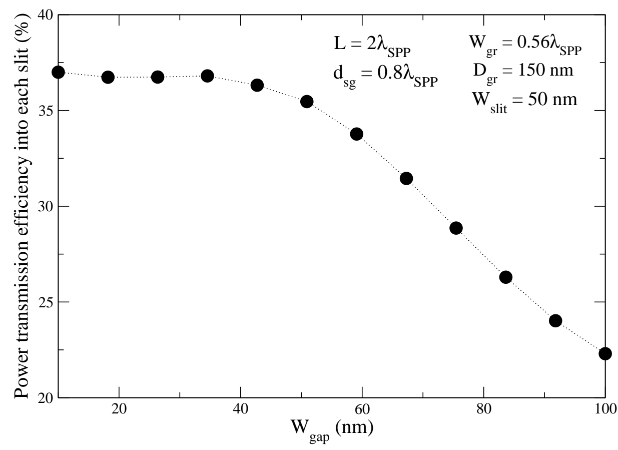

Figure 6.21: Simulated power coupling efficiency into each plasmonic slit as a function of W_{gap}.

Chapter 7

Conclusion and future outlook

7.1 Summary

Theoretical investigations of the excitation of SPPs in a simple metal-dielectric (air) interface, IMI and MIM structures were carried out. The SPP mode confinement is weaker in IMI based plasmonic structures, however the loss due to absorption by the metal is lower. In contrast, a stronger SPP mode confinement can be achieved in MIM based structures, but at the expense of large loss due to absorption. Hence, a trade-off between the SPP mode confinement and loss was generally observed in plasmonic structures.

The wavevector of the incident light should be always greater than that of the SPPs in order to excite them. This can be achieved by implementing the Kretschmann technique or by patterning the surface of the metal-dielectric structures (chapter one) which provides the extra momentum for fulfilling the phase matching condition between the incident light and SPP wavevectors. A periodic metal grating structure on an SOI waveguide was used to analyse the SPP mode dispersion compared to the light lines in air. The Bragg condition in such a structure can be satisfied by tuning the periodicity of the gratings, which leads to a resonance condition, and therefore minimum system transmission. This occurs near the band zone edge of the SPP dispersion curve, leading to the reduction of the group velocity of SPPs, which in turn results in slowing of the

light.

The 2nd chapter describes a theoretical investigation using a 2D FEEM, the subwavelength confinement property of SPPs in a metallised stub cavity structure coupled to an underlying single mode dielectric waveguide, for optical modulation purposes. Metal wings at the sides of the stub were used to achieve an efficient coupling of the input mode into SPP modes, which was indicated by the pinning of the mode at the metal-dielectric interface. The stub was filled with an optically active material (Ge/SiGe MQWs or Ge QDs) whose imaginary part of the refractive index (and therefore the absorption coefficient) is changed via an externally applied bias. This in turn spoils the resonance (and therefore Q factor) of the stub, which modifies the optical transmission through the system. Such a structure is also analogous to a transmission line circuit theory, in which different orders of vertical EM resonance within the stub can be obtained by tuning the stub height. Thus, a comparison was carried out between the transmission line and electromagnetic models, which demonstrated good agreement between the two models with respect to the dependence of absorption on the stub height. This in turn was achieved by subtracting a correction length ($\triangle H$) from the geometrical height of the stub. Moreover, higher orders of lateral EM resonance were obtained for wider stubs (W >0.45μm). It was found that wider stubs introduce an EM mode conversion effect, which transforms the symmetric field profile of the input mode into almost asymmetric field profile of the EM mode in the output waveguide. This happens when κ of the stub filling increases from a lower (κ=0.01) to a larger value (κ=0.05), leading to a negligible EM mode overlap with the single mode output waveguide, and therefore results in a reduced transmission. Possible electrical biasing schemes and optimisation of the stub structure with respect to its physical parameters (W and H) were carried out using the electrostatic and electromagnetic simulations to achieve maximum ER and minimum IL for a practically attainable range of κ values.

The simulations of the stub structure were then extended into three dimensions, within which two structures were considered: the original TM-mode stub modulator, and an alternative stub structure intended for TE mode modulation. However, the

FEEM results indicated that the TE mode cannot be efficiently coupled to the stub for any practical range of stub absorption coefficients, and hence very little modulation can be achieved: the simulated extinction ratios are < 2dB. 3D simulations of the TM mode stub modulator showed a strong EM mode conversion effect for stubs supporting 3rd orders of lateral and vertical EM resonance, which resulted in an optimised ER of 7.5dB with an IL of 8dB. Additionally, it was found that the mode conversion effect and increase in κ behave in an opposite manner: i.e the former effect becomes weaker as the κ of the stub material increases and vice versa. The 3D FEEM results indicated that the EM mode conversion is a more dominant effect than the increase in κ of the stub material, which leads to a more controllable transmission at the output waveguide. Furthermore, simulations were carried out with respect to different stub depths along the third dimension, which indicated that the 2D approximation is not accurate for stubs and waveguides with depths less than 2μm.

A plasmon mode existing within a low index gap layer sandwiched between a conductor and a high index dielectric layer was investigated in chapter five. The confinement of this mode was quite sensitive to the variation in the thickness and refractive index of the gap layer. Thus, optical modulation in such a CGD system can be achieved by varying the refractive index of the gap layer via an externally applied bias, which modifies the transmission through the waveguide between the biased and unbiased states. However, a large change in the refractive index of up to $7\text{x}10^{-2}$ was required to achieve significant ER, which is quite difficult to obtain in Si. Alternatively, the structure was modified by including an oxide layer between the conductor and gap layers similar to a MOS-Ge system, in which a large index change can be achieved via charge carrier accumulation effect near metal-oxide-gap junction. Anyhow, the presence of an oxide layer degraded the overall system performance, resulting in a negligible ER. The CGD structure was also investigated for exciting plasmon and dielectric modes simultaneously, which for a given device length interfere constructively or destructively in an unbiased or a biased state. But, these modes should be excited with different amplitudes with respect to each other, which is also quite challenging to realise in practice.

Following from the above work, the free carrier charge accumulation and electromagnetic effects near the MIS junction in a symmetric MISIM MZ structure were investigated to achieve electro-optic based interference modulation using carrier transport and 2D FEEM. Each arm of the Mach-Zehnder structure comprised a MISIM structure, and the accumulation mode over the inversion mode device operation was considered suitable since the former device predicted a larger electron density peak near the MIS junction for a given bias. Additionally, HfO_2 rather than SiO_2 was considered since a larger portion of the applied bias (due to a smaller effective oxide thickness) is available across the silicon layer, causing a larger electron density peak in the MISIM structure. A larger electron density in the MISIM MZ device was required to achieve a larger perturbation of the confinement of the EM mode when a bias was applied, which leads to a larger change in the effective plasmon mode index ($\triangle n_{eff}$). A larger $\triangle n_{eff}$ eventually leads to a shorter device arm length required to achieve destructive interference between the plasmon modes from the two arms of the MZ device. The MISIM MZ accumulation mode device was optimised to achieve a strong electro-optic effect with respect to its different physical parameters, which resulted in an optimised performance with IL as low as 1dB for the device arm length of only 0.25μm for an asymmetric Mach-Zehnder structure biased in push-pull mode.

Additionally, the MISIM structure was also investigated to employ it as a simple single waveguide EA device. In this case, optical modulation was obtained by calculating the difference between the propagation loss in the biased and unbiased states for a particular device length. The dependence of the propagation loss on different physical parameters (W, H and t_{ox}) was carried out using 2D FEEM. The results predicted better system performance for thinner silicon and oxides having larger dielectric constant, however the overall device performance (ER=5.2dB and IL=7.2dB for 1μm device length) was found to be comparatively weaker than that obtained in the MISIM MZ EO device.

Thus, various electro-optic and electroabsorption modulators were investigated including the coupled stub, MISIM MZ and single waveguide MISIM EA devices. Depending upon the fabrication precision, the electro-optic stub modulator can be designed to

achieve a very large ER with an acceptable IL, however the fabrication of such a modulator is quite difficult to realise in practice. On the other hand, the MISIM EO and EA modulators show quite promising results. Fabrication of the MISIM EA single waveguide device is simple and easy compared to the other designs, but the predicted IL is comparatively large. The MISIM EO MZ device has the best predicted results with an IL as low as 1dB for a device length of only 0.25μm (and therefore the smallest footprint compared to the other modulator devices considered here), and a power consumption of only 40 fJ/bit for an applied bias of 4V. The recently published MZ EO and single waveguide EA plasmonic modulators proposed by Shiyang et. al [128] have shown insertion losses of 8dB and 4.5dB in 3μm and 4μm long devices respectively, with power consumptions of 240 and 339 fJ/bit respectively. The above results indicate that plasmonic devices can be used for optical modulation purposes with nanoelectronics circuitry, especially since they provide very small device footprints compared to conventional photonic modulators, which are generally several millimetres long.

Finally, a silicon-based plasmonic nanofocusing structure was investigated theoretically for coupling light from a wide fibre input opening directly into a nano sized plasmonic waveguide. The structure comprises symmetrically arranged metallised grooves which converges into a nano slit at the apex. The period and angle of the grooves were optimised so that SPPs coming from each groove remain in phase. In such a situation, the incident light coherently excites and focuses SPPs while constructively interfering with SPPs from the other grooves as they propagate towards the apex of the structure. An analytical transfer matrix model was also developed to investigate the coupling efficiencies with respect to different groove depths. A qualitative agreement between the TMM and FEM results was obtained with respect to the position of different peaks of the coupling of light into the nano slit. The structure was then optimised for different structural parameters (d_{sg}, W_{gr}, N_{gr}, W_{sl}) to achieve maximum coupling into the slit. Thus a maximum efficiency of 72% of light from a 6.2μm wide input opening into a 20nm metal-silicon-metal plasmonic waveguide at the apex was obtained. Additionally, the optimised structure was applied to investigate coupling into a 300nm single mode di-

electric waveguide, which resulted in an efficiency of 60%. Moreover, a coupling efficiency of 2×37% (or 1.3dB IL) was obtained, in which the structure was used to simultaneously couple and split light from a wide fibre opening (6.4μm) into two nano-plasmonic waveguides (width 50nm) at the apex of the structure.

A significant advantage of the structure is that it is very short– less than a third of the input aperture width. The proposed plasmonic coupler therefore promises to be a key component in future on-chip plasmonic optical circuits for coupling light directly from a large area fibre grating into a nanoscale plasmonic waveguide. Furthermore, the capability of the structure to provide simultaneous coupling and splitting into two equivalent plasmonic waveguide means that it could be used to couple an optical carrier directly into an Mach-Zehnder plasmonic modulator, hence providing a high efficiency passive front end for an on-chip plasmonic transceiver.

7.2 Future of silicon-based plasmonic integrated circuits

The highly confined nature of SPPs in plasmonic structures can be applied to achieve various optical active and passive elements with device footprint much smaller than the wavelength of the incident light. With recent advances in fabrication technology and simulation tools, plasmonic structures have been able to demonstrate efficient control on the flow of light, and by engineering these structures: they can exhibit unparallelled ability to concentrate light, and also to 'trap' light, for example in solar cells for energy harvesting. Silicon compatible plasmonic based circuits will have the advantages of the size of nano-electronics and speed of photonic devices, which will eventually lead to the realisation of silicon-plasmonic on-chip transceiver system for telecommunication applications with very low energy requirements. Various plasmonic enhanced optical components in such a system would include a 2×2/4×4 (de)multiplexer, a low power active on/off modulator/switching device (possibly realisable using MZI type plasmonic structure, for example the one explained in chapter 4), a highly efficient in/out coupling from a wide input optical fibre grating couplers, low loss waveguides, and detectors.

Various plasmonic optical devices described above have been recently realised by researchers around the world. These include theoretical investigations of wavelength-division-(de)multiplexing enabled transmission of 480 Gb/s (12x40 GB/s) aggregated through a 60 μm long hybrid dielectric-loaded-SPP waveguide [163–165]. A dual periodic MIM based heterowaveguide structure was theoretically and numerically investigated to achieve SPP wavelength division multiplexing application [166]. An experimental demonstration of a plasmonic laser using a hybrid plasmonic waveguide comprising a high gain cadmium sulphide semiconductor nanowire, separated from a silver surface by an insulating gap, was reported in which the generated optical modes were a hundred times smaller than the diffraction limit [167]. In other developments, hybrid plasmonic waveguides and directional couplers were demonstrated with a propagation loss of 0.08dB/μm at the telecommunication wavelength of 1.55 μm [168]. However, one of the key aspects in developing plasmonic devices is that they are SOI compatible, which is important in silicon-plasmonic research in order to realise plasmonics based circuits for interconnects and datacom applications, and raise a significant hope for developing a '*router-on-chip*' prototype which will have extremely large capacity and very low power consumption.

References

[1] R. Ritchie, "Plasma losses by fast electrons in thin films." *Phys. Rev.*, vol. 106, pp. 874–881, 1957.

[2] S. L. Cunningham, A. A. Maradudin, and R. F. Wallis, "Effect of a charge layer on the surface-plasmon-polariton dispersion curve," *Phys. Rev. B*, vol. 10, pp. 3342–3355, 1974.

[3] D. Bohm and D. Pines, "A collective description of electron interactions. i. magnetic interactions," *Phys. Rev.*, vol. 82, pp. 625–634, 1951.

[4] D. Pines and D. Bohm, "A collective description of electron interactions: Ii. collective vs individual particle aspects of the interactions," *Phys. Rev.*, vol. 85, pp. 338–353, 1952.

[5] D. Bohm and D. Pines, "A collective description of electron interactions: Iii. coulomb interactions in a degenerate electron gas," *Phys. Rev.*, vol. 92, pp. 609–625, 1953.

[6] D. Pines, "A collective description of electron interactions: Iv. electron interaction in metals," *Phys. Rev.*, vol. 92, pp. 626–636, 1953.

[7] J. M. Pitarke, V. Silkin, E. Chulkov, and P. Echenique, "Theory of surface plasmons and surface-plasmon polaritons," *Rep.Prog.Phys.*, vol. 70, 2007.

[8] C. J. Powell and J. B. Swan, "Origin of the characteristic electron energy losses in magnesium," *Phys. Rev.*, vol. 116, pp. 81–83, 1959.

[9] E. A. Stern and R. A. Ferrell, "Surface plasma oscillations of a degenerate electron gas," *Phys. Rev.*, vol. 120, pp. 130–136, 1960.

[10] E. Kretschmann and H. Reather, "Radiative decay of nonradiative surface plasmon excited by light," *Naturf*, vol. 23A, pp. 2135–2136, 1968.

[11] A. Otto, "Excitation of nonradiative surface plasma waves in silver by the method of frustrated total reflection," *Z. Phys.*, vol. 216, p. 398, 1968.

[12] J. Homola, S. S. Yee, and G. Gauglitz, "Surface plasmon resonance sensors: review," *Sensors and Actuators B: Chemical*, vol. 54, pp. 3–15, 1999.

[13] W. Knoll, "Interfaces and thin films as seen by bound electromagnetic waves," *Annual Rev. of Phys. Chem.*, vol. 49, pp. 569–638, 1998.

[14] M. Malmqvist, "Biospecific interaction analysis using biosensor technology," *Nature*, vol. 361, pp. 186–187, 1993.

[15] F. Chien and S. Chen, "A sensitivity comparison of optical biosensors based on four different surface plasmon resonance modes," *Biosensors and Bioelectronics*, vol. 20, pp. 633–642, 2004.

[16] A. Pipino, J. Woodward, C. Meuse, and V. Silin, "Surface-plasmon-resonance-enhanced cavity ring-down detection," *J. Chem. Phys.*, vol. 120, p. 1629179, 2004.

[17] B. Rothenhausler and W. Knoll, "Surface–plasmon microscopy," *Nature*, vol. 332, pp. 615–617, 1988.

[18] G. Flatgen, K. Krischer, B. Pettinger, K. Doblhofer, H. Junkes, and G. Ertl, "Two-dimensional imaging of potential waves in electrochemical systems by surface plasmon microscopy," *Science*, vol. 269, pp. 668–671, 1995.

[19] R. Green, R. Frazier, K. Shakesheff, M. Davies, C. Roberts, and S. Tendler, "Surface plasmon resonance analysis of dynamic biological interactions with biomaterials," *Biomaterials*, vol. 21, pp. 1823–1835, 2000.

[20] B. Liedberg, C. Nylander, and I. Lunstrom, “Surface plasmon resonance for gas detection and biosensing,” *Sensors and Actuators*, vol. 4, pp. 299–304, 1983.

[21] S. Schuster, R. Swanson, L. Alex, R. Borret, and M. Simon, “Assembly and function of a quaternary signal transduction complex monitored by surface plasmon resonance,” *Nature*, vol. 365, pp. 343–347, 1993.

[22] P. Schuck, “Use of surface plasmon resonance to probe the equilibrium and dynamic aspects of interactions between biological macromolecules,” *Annu. Rev. Biophys. Biomol. Struct*, vol. 26, pp. 541–566, 1997.

[23] D. M. Hernandez, J. Villatoro, D. Talavera, and D. Luna-Moreno, “Optical-fibre surface-plasmon resonance sensor with multiple resonance peaks,” *Appl. Opt.*, vol. 43, pp. 1216–1220, 2004.

[24] A. R. Mendelsohn and R. Brent, “Protein interaction methods-toward an endgame,” *Science*, vol. 284, pp. 1948–1950, 1999.

[25] A. Alexandre, P. Gershon, and H. A. Schuessler, “Surface-plasmon resonance spectrometry and characterisation of absorbing liquids,” *Appl. Opt.*, vol. 39, pp. 3314–3320, 2000.

[26] J. Pendry, “Playing tricks with light,” *Science*, vol. 285, pp. 1687–1688, 1999.

[27] E. Prodan, C. Radloff, N. Halas, and P. Nordlander, “A hybridization model for the plasmon response of complex nanostructures,” *Science*, vol. 302, pp. 419–422, 2003.

[28] M. Quinten, A. Leitner, J. R. Krenn, and F. R. Aussenegg, “Electromagnetic energy transport via linear chains of silver nanoparticles,” *Opt. Lett.*, vol. 23, pp. 1331–1333, 1998.

[29] R. Charbonneau, P. Berini, E. Berolo, and E. Lisicka-Shrzek, “Experimental observation of plasmon polariton waves supported by a thin metal film of finite width,” *Opt. Lett.*, vol. 25, pp. 844–846, 2000.

[30] B. Lamprecht, J. Krenn, G. Scheider, H. Ditlbacher, M. Salerno, N. Felidj, A. Leitner, F. Aussenegg, and J. Weeber, “Surface plasmon propagation in microscale metal stripes,” *Appl. Phys. Lett.*, vol. 79, p. 1380236, 2001.

[31] T. Nikolajsen, K. Leosson, I. Saladutinov, and S. Bozhevolnyi, “Polymer-based surface-plasmon-polariton stripe waveguides at telecommunication wavelengths,” *Appl. Phys. Lett.*, vol. 82, no. 5, pp. 668–670, 2003.

[32] J. R. Krenn, B. Lamprecht, H. Ditlbacher, G. Schider, M. Salerno, A. Leitner, and F. Aussenegg, “Nondiffraction-limited light transport by gold nanowires.” *Europhys. Lett.*, vol. 60, pp. 663–669, 2002.

[33] J. Krenn and J. Weeber, “Surface plasmon polaritons in metal stripes and wires,” *Philos. Trans. R. Soc. Lond. Ser. A*, vol. 362, pp. 739–756, 2004.

[34] W. A. Murray, S. Astilean, and W. L. Barnes, “Transition from localised surface plasmon resonance to extended surface plasmon-polariton as metallic nanoparticles merge to form a periodic hole array,” *Phys. Rev. B*, vol. 69, p. 165407, 2004.

[35] S. A. Maier, P. Barclay, T. Johnson, M. Friedman, and O. Painter, “Low-loss fibre accessible plasmon waveguide for planar energy guiding and sensing,” *Appl. Phys. Lett.*, vol. 84, pp. 3990–3992, 2004.

[36] I. V. Novikov and A. A. Maradudin, “Channel polaritons,” *Phys. Rev. B*, vol. 66, p. 035403, 2002.

[37] D. F. P. Pile and D. K. Gramotnev, “Plasmonic subwavelength waveguides: next to zero losses at sharp bends,” *Opt. Lett.*, vol. 30, pp. 1186–1188, 2005.

[38] D. Pile, T. Ogawa, D. Gramotnev, K. Vernon, K. Yamaguchi, T. Okamoto, M. Haraguchi, and M. Fuki, “Two-dimensionally localised modes of a nanoscale gap plasmon waveguide,” *Appl. Phys. Lett.*, vol. 87, p. 261114, 2005.

[39] H. J. Lezec, A. Degiron, E. Devaux, R. A. Linke, L. Martin-Moreno, F. J. Garcia-Vidal, and T. W. Ebbesen, “Beaming light from a subwavelength aperture,” *Science*, vol. 297, pp. 820–822, 2002.

[40] T. Ebbesen, H. Lezec, H. Ghaemi, T. Thio, and P. Wolff, “Extraordinary optical transmission through sub-wavelength hole arrays,” *Nature*, vol. 391, pp. 667–669, Nov. 1997.

[41] E. Ozbay, “Plasmonics: merging photonics and electronics at nanoscale dimensions,” *Science*, vol. 311, pp. 189–193, 2006.

[42] H. Ditlbacher, J. Krenn, G. Schider, A. Leitner, and F. Aussenegg, “Two-dimensional optics with surface plasmon polaritons,” *Appl. Phys. Lett.*, vol. 81, no. 10, pp. 1762–1764, 2002.

[43] W. Nomuar, M. Ohtsu, and T. Yatsui, “Nanodot coupler with a surface plasmon polariton condenser for optical far/near-field conversion,” *Appl. Phys. Lett.*, vol. 86, p. 181108, 2005.

[44] R. Walters, v. R. Loon, I. Brunets, J. Schmitz, and A. Polman, “A silicon-based electrical source of surface plasmon polaritons,” *Nature materials*, vol. 9, pp. 21–25, 2009.

[45] J. Dionne, L. Sweatlock, M. Sheldon, A. Alivisatos, and H. Atwater, “Silicon-based plasmonics for on-chip photonics,” *Selected Topics in Quantum Electronics, IEEE Journal of*, vol. 16, pp. 295–306, 2010.

[46] J. Dionne, K. Diest, L. Sweatlock, and H. Atwater, “Plasmostor: A metal-oxide-si field effect plasmonic modulator,” *Nano Lett.*, vol. 9, pp. 897–902, 2009.

[47] R. Oulton, V. Sorger, D. Genov, D. Pile, and X. Zhang, “A hybrid plasmonic waveguide for subwavelength confinement and long-range propagation,” *Nat. Phot.*, vol. 2, pp. 496–500, 2008.

[48] D. Daoxin and H. Sailing, "Integrated silicon photonic nanocircuits and technologies for optical interconnect and optical sensing," *Conf. on optoelec. int. circuits, Proc. of SPIE*, vol. 8265, p. 82650L, 2012.

[49] S. Papaioannou, K. Vyrsokinos, O. Tsilipakos, A. Pitilakis, K. Hassan, J. C. Weeber, L. Markey, A. Dereux, S. I. Bozhevolnyi, A. Miliou, E. E. Kriezis, and N. Pleros, "A 320 gb/s-throughput capable 2 x 2 silicon-plasmonic router architecture for optical interconnects," *J. lightwave tech.*, vol. 29, pp. 3185–3195, 2011.

[50] Y. J. Zhou and T. J. Cui, "Multidirectional surface-wave splitters," *Appl. Phys. Lett.*, vol. 98, 2011.

[51] S. Sederberg, D. Driedger, M. Nielsen, and A. Y. Elezzabi, "Ultrafast all-optical switching in a silicon-based plasmonic nanoring resonator," *OPTICS EXPRESS*, vol. 19, pp. 23 494–23 503, 2011.

[52] R. Thomas, Z. Ikonic, and R. W. Kelsall, "SiGe metallised stub and plasmonic gap mode electro-absorption modulators," *Proc. of SPIE*, vol. 7943, 2011, Conference on silicon photonics VI, San Francisco, CA, JAN 23-26, 2011.

[53] J. Wang, X. Guan, Y. He, Y. Shi, Z. Wang, S. He, P. Holmström, L. Wosinski, L. Thylen, and D. Dai, "Sub-μm2 power splitters by using silicon hybrid plasmonic waveguides," *Opt. Express*, vol. 19, pp. 838–847, 2011.

[54] Y.-J. Tsai, A. Degiron, N. M. Jokerst, and D. R. Smith, "Plasmonic multi-mode interference couplers," *Opt. Express*, vol. 17, pp. 17 471–17 482, 2009.

[55] Z. Han and S. He, "Multimode interference effect in plasmonic subwavelength waveguides and an ultra-compact power splitter," *Optics Communications*, vol. 278, no. 1, pp. 199–203, 2007.

[56] H. Chu, Y. Akimov, P. Bai, P. Li, and W. Hoefer, "Ultra compact wavelength-selective silicon-based plasmonic components," *Quant. Elec. Laser Sc. Conf.*, 2010.

[57] O. Hess, J. B. Pendry, S. A. Maier, R. F. Oulton, J. M. Hamm, and K. L. Tsakmakidis, "Active nanoplasmonic metamaterials," *Nat. Mat.*, vol. 11, pp. 573–584, 2012.

[58] V. Giannini, A. Fernandez-Dominguez, S. Heck, and S. Maier, "Plasmonic nanoantennas: fundamentals and their use in controlling the radiative properties of nanoemitters," *Chem. Rev.*, vol. 111, pp. 3888–3912, 2011.

[59] O. Hess and K. Tsakmakidis, "Slow and stopped light in metamaterials," *NUSOD 2008: Proc. of the 8th inter. conf. on num. sim. of optoelec. dev.*, pp. 97–98, 2008.

[60] O. Hess, K. L. Tsakmakidis, E. I. Kirby, T. Pickering, and J. M. Hamm, "Gain in negative-refractive-index slow-light waveguides," *Proc. of SPIE, conf on adv. in slow and fast light IV*, vol. 7949, 2011.

[61] S. A. Maier, *Plasmonics: Fundamentals and Applications.* Springer Science, 2007.

[62] D. Sarid and W. Challener, *Modern Introduction to Surface Plasmons- Theory, Mathematica Modelling and Applications.* Cambridge, 2010.

[63] E. van Faassen, "Dielectric response of a nondegenerate electron gas in semiconductor nanocrystallites," *Phys. Rev. B*, vol. 58, p. 15729, 1998.

[64] J. Pendry, "New magnetic material emphasise the negative," pp. 1–5, 2001.

[65] S. Ramakrishna, "Physics of negative refractive index materials," *Rep. Prog. Phys.*, vol. 68, pp. 449–521, 2005.

[66] A. V. Zayats, I. I. Smolyaninov, and A. A. Maradudin, "Nano optics of surface plasmon polaritons," *Physics Reports*, vol. 408, pp. 131–314, 2005.

[67] R. Zia, M. D. Selker, P. B. Cartysse, and M. L. Brongersma, "Geometries and materials for subwavelength surface plasmon modes," *J. Opt. Soc*, vol. 21, 2004.

[68] G. Lǵraveevh́ateque. and O. J. Martin, "Optimisation of finite diffraction gratings for the excitation of surface plasmons," *J.Appl.Phys.*, vol. 100, 2006.

[69] S. I. Bozhevolnyi, A. Boltasseva, T. Sondergaard, T. Nikolajsen, and K. Leosson, "Photonic bandgap structures for long-range surface plasmon polaritons," *Optics Communications*, vol. 250, pp. 328–333, 2005.

[70] A. V. Zayats, I. I. Smolyaninov, and A. A. Maradudin, "Nano-optics of surface plasmon polaritons," *Phys. Reports*, vol. 408, pp. 131–134, 2005.

[71] S. C. Kitson, W. L. Barnes, and J. R. Sambles, "Full photonic band gap for surface modes in the visible," *Phy. Rev. Letter*, vol. 77, pp. 897–902, 1996.

[72] G. Mattiussi and P. Berini, "Demonstration of bragg gratings based on long-ranging surface plasmon polariton waveguides," *Opt Exp.*, vol. 13, June. 2005.

[73] "Comsol multiphysics 4.1," `http://www.comsol.com`.

[74] W.D.Hayes, "Group velocity and nonlinear dispersive wave propagation," in *Proc. R. Soc. Lond.*, vol. 332. Royal Society, 1973, pp. 199–221.

[75] S. H. Lin, K. y Hsu, and P. Yeh, "Experimental observations of the slow down of optical beams by a volume index grating in a photo-refractive linbo$_3$ crystal," *Opt. Lett.*, vol. 25, 2000.

[76] Q. Gan, Z. Fu, Y. J. Ding, and F. J. Bartoli, "Ultrawide-bandwidth slow light systems based on thz plasmonic graded metallic structures," *Phys. Rev. Lett.*, vol. 25, 2008.

[77] C. Kittel, *Introduction to solid state physics*, 8th ed. Wiley international, 1973.

[78] D. Pacifici, H. Lezec, and H. Atwater, "All-optical modulation by plasmonic excitation of cdse quantum dots," *Nat. Photo.*, vol. 1, pp. 402–406, 2007.

[79] V. V. W. Marcelo, Z. Han, "Conductor-gap-silicon plasmonic waveguides and passive components at subwavelength scale," *Opt. Exp.*, vol. 18, p. 11728, 2010.

[80] Z. W. J. Pan, H. Kaiting, "Realisation of subwavelength guiding utilising coupled wedge plasmon polaritons in splitted groove waveguides," *Opt. Exp.*, vol. 18, pp. 16 722–16 732, 2010.

[81] D. Crouse and P. Keshavareddy, "A method for enhancing designing electromagnetic resonance enhanced silicon-on-insulator metal-semiconductor-metal photodetectors," *J. of Opt.*, vol. 8, pp. 175–181, 2006.

[82] P. Johnson and R. Christy, "Optical constants of noble metals," *Phys. Rev. B*, vol. 6, pp. 4370–4379, 1972.

[83] C. Min and G. Veronis, "Absorption switches in metal-dielectric-metal plasmonic waveguides," *Opt. Exp.*, vol. 17, no. 13, pp. 10 757–10 766, 2009.

[84] M. Yosuku, O. Toshihiro, H. Masanobu, F. Masuo, and N. Masatoshi, "Characteristics of gap plasmon waveguide with stub structures," *Opt. Exp.*, vol. 16, pp. 16 314–16 325, 2008.

[85] A. Pannipitiya, I. Rukhlenko, M. Premaratne, H. Hattori, and G. Agarwal, "Improved transmission model for metal-dielectric-metal waveguides with stub structure," *Opt. Exp.*, vol. 18, pp. 6191–6204, 2010.

[86] M. Haraguchi, Y. Matsuzaki, T. Tsuzura, T. Okamoto, M. Fukui, K. Okamoto, S. Seki, and S. Tagawa, "Plasmonic waveguides with wavelength selective function." *SPIE proc.*, vol. 7033, 2008.

[87] J. Liu, G. Fang, H. Zhao, Y. Zhang, and S. Liu, "Surface plasmon reflector based onserial stub structure," *Opt. Express*, vol. 17, pp. 20 134–20 139, 2009.

[88] G. Veronis and S. Fan, "Theoretical investigation of compact couplers between dielectric slab waveguides and two dimensional metal- dielectric-metal plasmonics waveguides," *Opt. Exp.*, vol. 15, pp. 1211–1221, 2007.

[89] C. Delacour, S. Blaize, P. Grosse, J. M. Fedeli, A. Bruyant, R. S. Montiel, G. Lerondel, and A. Chelnokov, "Efficient directional coupling between silicon and copper

plasmonic nanoslot waveguides: toward metal-oxide- silicon nanophotonics," *Nano Lett.*, vol. 10, pp. 2922–2926, 2010.

[90] S. Robert, "Optical properties of copper," *Phys. Rev.*, vol. 118, pp. 1509–1518, 1960.

[91] D. Pozar, Ed., *Microwave engineering*, 3rd ed. John Wiley and Sons. Inc., 1973.

[92] A. Pannipitiya, I. Rukhlenko, and M. Premaratne, "Analytical modeling of resonant cavities for plasmonic-slot-waveguide junctions," *IEEE. Phot. J.*, vol. 3, pp. 220–233, 2011.

[93] N. Ida, Ed., *Engineering Electromagnetics*, 2nd ed. Springer, 2003.

[94] Y. Kuo, Y. Lee, G. Yangsi, S. Ren, J. Roth, T. Kamins, M. D.A.B, and J. Harris, "Quantum-confined stark effect in ge/sige quantum wells on si for optical modulators," *IEEE. J. of Sel. Top. in Quant. Elec.*, vol. 12, pp. 1503–1513, 2006.

[95] P. Chaisakul, D. Marris-Morini, M.-S. Rouifed, G. Isella, D. Chrastina, J. Frigerio, X. L. Roux, S. Edmond, J.-R. Coudevylle, and L. Vivien, "23 ghz ge/sige multiple quantum well electro-absorption modulator," *Opt. Express*, vol. 20, pp. 3219–3224, 2012.

[96] Y. Kuo, Y. Lee, G. Yangsi, S. Ren, J. Roth, T. Kamins, D. Miller, and H. J.S, "Strong quantum confined stark effect in germanium quantum well structures on silicon," *Nat. Lett.*, vol. 437, no. 04204, p. 1334, Oct. 2005.

[97] Y.-H. Kuo, Y. Lee, S. Ren, Y. Ge, D. Miller, and J. Harris, "Quantum-confined stark effect electroabsorption in ge/sige quantum wells on silicon substrates," in *Lasers and Electro-Optics Society, 2005. LEOS 2005. The 18th Annual Meeting of the IEEE*, oct. 2005, pp. 284–285.

[98] H. Haus and Y. Lai, "Theory of cascaded quarter wave shifted distributed feedback resonators," *Quantum Electronics, IEEE Journal of*, vol. 28, pp. 205–213, Jan. 1992.

[99] J. E. Roth, F. O, R. Schaevitz1, Y.-H. Kuo, T. I. K. J. S. Harris, and D. A. B. M. and, "Optical modulator on silicon employing germanium quantum wells," *Opt. Express*, vol. 15, no. 9, p. 5851, 2007.

[100] R. Prasanth, J. Haverkort, and J. Wolter, "Electro-refraction in quantum dots: Dependence on lateral size and shape," *IEEE Transactions on Nanotechnology*, vol. 3, pp. 270–274, 2004.

[101] I. Avrutsky, R. Soref, and W. Buchwald, "Sub-wavelength plasmonic modes in a conductor-gap-dielectric system with a nanoscale gap," *Opt. Exp.*, vol. 18, pp. 348–363, 2009.

[102] M. Wu, Z. Han, and V. Van, "Conductor-gap-silicon plasmonic waveguides and passive components at subwavelength scale," *Opt. Express*, vol. 18, no. 11, pp. 11 728–11 736, May 2010. [Online]. Available: http://www.opticsexpress.org/abstract.cfm?URI=oe-18-11-11728

[103] R. Chau, S. Datta, M. Doczy, B. Doyle, J. Kavalieros, and M. Metz, "High-kappa;/metal-gate stack and its mosfet characteristics," *Electron Device Letters, IEEE*, vol. 25, no. 6, pp. 408 – 410, june 2004.

[104] R. Thomas, Z. Ikonic, and R. Kelsall, "Plasmonic enhanced electro-optic stub modulator on a soi platform," *Photonics and Nanostr.*, vol. 9, p. 101, 2011.

[105] D. Miller, "Germanium quantum wells for high performance modulators in silicon photonics," *Photonics Spectra*, p. 80, Sept. 2007.

[106] G. Reed, G. Mashanovich, F. Gardes, and D. Thomson, "Silicon optical modulators," *Nat. Phot.*, vol. 4, pp. 518–526, 2010.

[107] M. Lipson, "Compact electro-optic modulators on a silicon chip," *Selected Topics in Quantum Electronics, IEEE Journal of*, vol. 12, no. 6, pp. 1520 –1526, nov.-dec. 2006.

[108] M. Nedeljkovic, R. Soref, and G. Mashanovich, "Free carrier electrorefraction and electroabsorption modulation predictions for silicon over the 1-14μm infrared wavelength range," *Photonics Journal, IEEE*, vol. 3, no. 6, pp. 1171 –1180, dec. 2011.

[109] R. S. I. Avrutsky and W. Buchwald, "Sub-wavelength plasmonic modes in a conductor-gap-dielectric system with a nano-scale gap," *Opt. Exp.*, vol. 18, pp. 348–363, 2007.

[110] G. T. Reed, *Silicon Photonics: the state of the art.* John Wiley & Sons, Ltd, 2008.

[111] M. lipson, "Compact electro-optic modulators on a silicon chip," *IEEE J. of Sel. Top. in Quan. Elec.*, vol. 12, pp. 1520–1526, 2006.

[112] R. Soref and B. R. Bennett, "Electro-optical effects in silicon," *IEEE J. of Quan. Elec.*, vol. 23, pp. 123–129, 1987.

[113] E. Feigenbaum, K. Diest, and H. A. Atwater, "Unity-order index change in transparent conducting oxides at visible frequencies," *Nano Letters*, vol. 10, pp. 2111–2116, 2010.

[114] S. Zhu, G. Q. Lo, and D. L. Kwong, "Theoretical investigation of silicon mos-type plasmonic slot waveguide based mzi modulators," *Opt. Express*, vol. 18, no. 26, pp. 27 802–27 819, Dec 2010. [Online]. Available: http://www.opticsexpress.org/abstract.cfm?URI=oe-18-26-27802

[115] W. Cai, J. White, and M. Brongersma, "Compact, high-speed and power-efcient electro-optic plasmonic modulators," *Nano Lett.*, vol. 9, no. 12, pp. 4403–4411, 2009.

[116] A. Melikyan, N. Lindenmann, S. Walheim, P. Lufke, S. Ulrich, J. Ye, P. Vicze, H. Hahn, T. Schimmel, C. Koos, W. Freude, and J. Leuthold, "Surface plasmon polariton absorption modulator," *Opt. Exp.*, vol. 19, no. 9, pp. 8855–8869, 2011.

[117] D. R, U. Keil, and T. Franck, “High speed silicon mach-zehnder modulator,” *Opt. Exp.*, vol. 13, no. 8, pp. 3129–3135, 2005.

[118] A. Chaudhary and J. Roy, “Mosfet models, quantum mechanical effects and modelling approaches: a review,” *J. of Semicond. Tech. and Sci.*, vol. 10, p. 20, 2010.

[119] J. Srikantaiah and A. Gupta, “Quantum mechanical effects in bulk mosfets from a compact modelling perspective: a review,” *IETE Tech. Rev.*, vol. 29, pp. 3–28, 2012.

[120] H. Jiang and P. Zhang, “Model analysis and parameter extraction for mos capacitor including quantum mechanical effects,” *J. of Computational Math.*, vol. 10, no. 81, p. 401, Mar 2006.

[121] Y. Li, T. wei Tang, and X. Wang, “Modeling of quantum effects for ultrathin oxide mos structures with an effective potential,” *Nanotechnology, IEEE Transactions on*, vol. 1, no. 4, pp. 238 – 242, Dec 2002.

[122] I. Silvaco Data Systems, “Silvaco, atlas user’s manual,” 2008.

[123] W. Hu, X. Chen, X. Zhou, Z. Quan, and L. Wei, “Quantum-mechanical effects and gate leakage current of nanoscale n-type finfets: A 2d simulation study,” *Mic. Elec. J.*, vol. 37, pp. 613–619, 2006.

[124] R. Salvador, R. Salvador, A. Martinez, C. Garcia-Meca, R. Ortuno, and J. Marti, “Analysis of hybrid dielectric plasmonic waveguides,” *IEEE J. of Sel. Top. in Quan. Elec*, vol. 14, no. 6, pp. 1496–1501, nov.-dec. 2008.

[125] I. Avrutsky, R. Soref, and W. Buchwald, “Sub-wavelength plasmonic modes in a conductor-gap-dielectric system with a nanoscale gap,” *Opt. Express*, vol. 18, no. 1, pp. 348–363, Jan 2010.

[126] A. Singh, “Free charge carrier induced refractive index modulation of crystalline silicon,” *GFP, 2010 IEEE Inter.*, pp. 102–104, 2010.

[127] P. Dong, L. Chen, and Y. Chen, “High-speed low-voltage single-drive push-pull silicon mach-zehnder modulators,” *Opt. Exp.*, vol. 20, pp. 6163–6169, 2012.

[128] Z. Shiyang, G. Lo, and D. Kwong, “Electro-absorption modulation in horizontal metal-insulator-silicon-insulator- metal nanoplasmonic slot waveguides,” *Appl. Phys. Lett.*, vol. 99, p. 151114, 2011.

[129] T. Thio, K. Pellerin, and R. Linke, “Enhanced ligh transmission through single subwavelength aperture,” *Opt. Lett.*, vol. 26, no. 24, p. 1972, 2001.

[130] E. Moreno, F. Garca-Vidal, and L. Moreno, “Enhanced transmission and beaming of light via photonic crystal surface modes,” *Phys. Rev. B*, vol. 69, no. 12, pp. 121 402–1, 2004.

[131] S. Zhu and W. Zhou, “Plasmonic properties of two-dimensional metallic nanoholes fabricated by focused ion beam lithography,” *Journal of Nanoparticle Research*, vol. 14, pp. 1–6, 2012. [Online]. Available: http://dx.doi.org/10.1007/s11051-011-0652-0

[132] J. M. Steele, Z. Liu, Y. Wang, and X. Zhang, “Resonant and non-resonant generation and focusing of surface plasmons with circular gratings,” *Opt. Express*, vol. 14, no. 12, pp. 5664–5670, Jun 2006. [Online]. Available: http://www.opticsexpress.org/abstract.cfm?URI=oe-14-12-5664

[133] S. A. Maier and H. A. Atwater, “Plasmonics: Localization and guiding of electromagnetic energy in metal/dielectric structures,” *Journal of Applied Physics*, vol. 98, no. 1, p. 011101, 2005. [Online]. Available: http://link.aip.org/link/?JAP/98/011101/1

[134] F. J. Garcia-Vidal and L. Martin-Moreno, “Transmission and focusing of light in one-dimensional periodically nanostructured metals,” *Phys. Rev. B*, vol. 66, p. 155412, Oct 2002. [Online]. Available: http://link.aps.org/doi/10.1103/PhysRevB.66.155412

[135] T. Thio, H. Lezec, T. Ebbesem, K. Pellerin, G. Lewen, A. Nahata, and R. Linke, "Giant optical transmission of subwavelength apertures: physics and applications," *Nanotech.*, vol. 13, pp. 429–432, 2002.

[136] T. Ebssen, H. Lezec, H. Ghaemi, T. Thio, and P. Wolff, "Extraordinary optical transmission through sub-wavelength hole arrays," *Lett. to Nat.*, vol. 391, no. 12, 1998.

[137] T. Ebssen and C. Genet, "Light in tiny holes," *Nature*, vol. 445, pp. 39–46, 2007.

[138] J. Dionne, L. Sweatlock, M. Sheldon, A. Alivisatos, and H. Atwater, "Silicon based plasmonics for on-chip photonics," *IEEE J. of Sel. Top. in Quant. Elec.*, vol. 16, no. 1, p. 295, 2010.

[139] O. Janssen, H. Urbach, and G. Hooft, "On the phase of plasmons excited by slits in a metal film," *Opt. Exp.*, vol. 14, no. 24, p. 1183, 2006.

[140] L. H. Thio T, T. Ebbesen, K. Pellerin, G. Lewen, A. Nahata, and R. Limke, "Giant optical transmission of subwavelength apertures: physics and applications," *Nano*, vol. 13, p. 429, 2002.

[141] H. Lezec, A. Degiron, R. Linke, M. Moreno, F. Vidal, and T. Ebbesen, "Beaming light from a subwavelength aperture," *Science*, vol. 297, p. 820, 2002.

[142] J. Porto, F. Garcia-Vidal, and J. Pendry, "Transmission resonances on metallic gratings with very narrow slits," *Phys. Rev. Lett.*, vol. 83, no. 14, pp. 2845–2848, 1999.

[143] H. Lezec and T. Thio, "Diffracted evanescent model for enhanced an suppressed optical transmission through subwavelength hole arrays," *Opt. Exp.*, vol. 12, p. 3629, 2004.

[144] S. Palacios, O. Mahboub, G. Vidal, L. Moreno, S. Rodrigi, C. Genet, and T. Ebbesen, "Mechanisms for extraordinary transmission through bull's eye structures," *Opt. Exp.*, vol. 19, p. 10429, May 2011.

[145] F. I. Baida, D. V. Labeke, and B. Guizal, "Enhanced confined light transmission by single subwavelength apertures in metallic films," *Appl. Opt.*, vol. 42, no. 34, pp. 6811–6815, Dec 2003. [Online]. Available: http://ao.osa.org/abstract.cfm?URI=ao-42-34-6811

[146] L.-B. Yu, D.-Z. Lin, Y.-C. Chen, Y.-C. Chang, K.-T. Huang, J.-W. Liaw, J.-T. Yeh, J.-M. Liu, C.-S. Yeh, and C.-K. Lee, "Physical origin of directional beaming emitted from a subwavelength slit," *Phys. Rev. B*, vol. 71, p. 041405, Jan 2005. [Online]. Available: http://link.aps.org/doi/10.1103/PhysRevB.71.041405

[147] H. Ghaemi, T. Thio, G. D.E, T. Ebbesen, and H. Lezec, "Surface plasmons enhanced optical transmission through subwavelength holes," *Phys. Rev. B*, vol. 58, no. 11, p. 6779, 1998.

[148] F. Vidal, H. Lezec, T. Ebbesen, and M. Moreno, "Light passing through subwavelength apertures," *Rev. of Modern Phys.*, vol. 82, p. 729, 2010.

[149] T. Sondergaard, S. Bozhevolnyi, S. Novikov, J. Beermann, E. Devaux, and Ebbesen, "Extraordinary optical transmission enhanced by nanofocusing," *Nano Lett.*, vol. 10, pp. 3123–3128, 2010.

[150] O. T. A. Janssen, H. P. Urbach, and G. W. 't Hooft, "Giant optical transmission of a subwavelength slit optimized using the magnetic field phase," *Phys. Rev. Lett.*, vol. 99, p. 043902, Jul 2007.

[151] L. Yin, V.-V. V.K, J. Pearson, J. Hiller, J. Hua, U. Welp, D. Brown, and C. Kimball, "Subwavelength focusing and guiding of surface plasmons," *Nano Lett.*, vol. 5, no. 7, pp. 1399–1402, 2005.

[152] G. Li and A. Xu, "Phase shifts of plasmons excited by slits in a metal film illuminated by oblique incident tm plane wave," *Proc. of SPIE*, vol. 7135, pp. 71 350T–9, 2008.

[153] L. G. Yuan, C. Lin, X. Feng, and X. An-Shi, "Plasmonic corrugated horn structure for optical transmission enhancement," *Chin. Phys. Lett.*, vol. 26, p. 124205, December 2009.

[154] X. Huang and M. Brongersma, "Rapid computation of light scattering from aperiodic plasmonic structures," *Phys. Rev. B*, vol. 84, p. 245120, 2011.

[155] V. R. Almeida, R. R. Panepucci, and M. Lipson, "Nanotaper for compact mode conversion," *Opt. Lett.*, vol. 28, no. 15, pp. 1302–1304, Aug 2003.

[156] T. Ang, G. Reed, A. Vonsovici, A. Evans, P. Routley, and M. Josey, "Effects of grating heights on highly efficient unibond soi waveguide grating couplers," *Photonics Technology Letters, IEEE*, vol. 12, no. 1, pp. 59 –61, Jan. 2000.

[157] J. Galan, P. Sanchis, B. Sanchez, and J. Marti, "Polarisation insensitive fibre to soi waveguide experimental coupling technique integrated with a v-groove structure," *Group IV Photonics, 4th IEEE Inter. Conference*, pp. 1–3, Sept. 2007.

[158] H. Sun, A. Chen, A. Szep, and L. R. Dalton, "Efficient fibre coupler for vertical silicon slot waveguides," *Opt. Express*, vol. 17, no. 25, pp. 22 571–22 577, Dec 2009.

[159] K. Shiraishi, M. Kagaya, K. Muro, H. Yoda, Y. Kogami, and C. Tsai, "Single mode fibre with a plano-convex silicon microlens for integrated butt-coupling scheme," *Opt. Exp*, vol. 47, no. 34, pp. 6345–6349, 2008.

[160] G. Veronis and S. Fan, "Theoretical investigation of compact couplers between dielectric slab waveguides and two-dimensional metal-dielectric-metal plasmonic waveguides," *Opt. Exp.*, vol. 15, pp. 1211–1221, 2007.

[161] X. He, L. Yang, and T. Yang, "Optical nanofocusing by tapering coupled photonic-plasmonic waveguides," *Opt. Express*, vol. 19, no. 14, pp. 12 865–12 872, Jul 2011.

[162] R. Thomas, Z. Ikonic, and R. Kelsall, "Electro-optic metal-insulator-semiconductor-insulator-metal mach-zehnder plasmonic modulator," *Phot. and Nanostr.*, vol. 10, pp. 183–189, 2011.

[163] O. Tsilipakos, A. Pitilakis, and E. Kriezis, "Hybrid silicon-plasmonics: Efficient waveguide interfacing for low-loss integrated switching components," *Conf. on nanophot. proc. of SPIE*, vol. 8424, p. 84241E, 2012.

[164] G. Oriol, T. Paul, B. Wang, and et al., "Design, fabrication and characterisation of fully-etched tm grating coupler for photonic integrated system-in-package," *Conf. on silicon phot. and phot. int. circuits, proc. of SPIE*, vol. 8431, p. 84310G, 2012.

[165] J. Weeber, K. Hassan, M. Neilson, and et al., "Dielectric loaded surface plasmon waveguides for datacom applications," *Conf. on nano phot. IV, proc. of SPIE*, vol. 8424, p. 842407, 2012.

[166] X. Q. Yu and S. Zhu, "Wavelength division multiplexer of surface plasmon polaritons using dual-periodical arranged metal gap waveguide," *3rd IEEE inter. nanoelec. conf.*, vol. 1-2, pp. 748–749, 2010.

[167] R. Oulton, V. Sorger, T. Zentgraf, and et al., "Plasmon lasers at deep subwavelength scale," *Nature let.*, vol. 461, pp. 629–632, 2009.

[168] L. Fei, W. Zhechao, D. Daoxin, L. Thylen, and L. Wosinski, "Experimental demonstration of ultra-compact directional couplers based on silicon hybrid plasmonic waveguides," *Appl. Phys. Lett.*, vol. 100, p. 241105, 2012.